Control of photochromic molecules adsorbed to optical microfibres

Dissertation

zur
Erlangung des Doktorgrades (Dr. rer. nat.)
der
Mathematisch-Naturwissenschaftlichen Fakultät
der
Rheinischen Friedrich-Wilhelms-Universität Bonn

vorgelegt von

Ulrich Wiedemann

aus
Karlsruhe

Bonn 2011

Angefertigt mit Genehmigung
der Mathematisch-Naturwissenschaftlichen Fakultät
der Rheinischen Friedrich-Wilhelms-Universität Bonn

1. Gutachter: Prof. Dr. Dieter Meschede
2. Gutachter: Prof. Dr. Stefan Linden

Tag der Promotion: 20.12.2011

Erscheinungsjahr: 2012

Diese Dissertation ist auf dem Hochschulschriftenserver der ULB Bonn
`http://hss.ulb.uni-bonn.de/diss_online` elektronisch publiziert

Abstract

The high light intensity in an optical microfibre and the resulting nonlinear effects were applied to develop a new method to precisely determine the microfibre diameter. The evanescent field of these optical microfibres was then used to control the internal state of surface-adsorbed photochromic molecules.

I start with a brief sketch of the mathematical description of light propagation in step-index optical fibres. From the results the main properties of optical microfibres are derived. Then, I describe the fabrication of optical microfibres with special requirements for the experiments presented later in the thesis.

A new technique to measure the submicrometre diameter of optical microfibres with an accuracy of better than 2 % is presented. This method is based on second- and third-harmonic generation. It is found that the fibre diameter can be unambiguously deduced from the peak wavelength of the harmonic light. High-resolution scanning electron microscope imaging is used to verify the results.

In the following, the experimental basics for the switching of photochromic molecules adsorbed to optical microfibres are described. I present the technique to deposit and detect the molecules and show their basic behaviour due to light exposure. The internal state of the molecules is measured via their state-dependent light absorption. Repeated switching between the states is achieved by exposure to the evanescent field of a few nanowatts of light guided in the microfibre.

The photochromic processes are then quantitatively analysed. Time-resolved photoswitching dynamics are measured and mathematically modelled with a rate equation model. By adjusting the microfibre evanescent field strength the dynamic equilibrium state of the molecules is controlled. I also study how many times the photochromic system can be switched before undergoing significant photochemical degradation.

Parts of this thesis have been published in the following journal articles:

- U. Wiedemann, K. Karapetyan, C. Dan, D. Pritzkau, W. Alt, S. Irsen, and D. Meschede, "Measurement of submicrometre diameters of tapered optical fibres using harmonic generation," *Opt. Express*, vol. 18, no. 8, pp. 7693–7704, 2010.

- R. Garcia-Fernandez, W. Alt, F. Bruse, C. Dan, K. Karapetyan, O. Rehband, A. Stiebeiner, U. Wiedemann, D. Meschede, and A. Rauschenbeutel, "Optical nanofibers and spectroscopy," *Appl. Phys. B*, vol. 105, no. 1, pp. 3–15, 2011.

Contents

Introduction **1**

1 Step-index optical fibres **5**

1.1 Light propagation in step-index optical fibres 5

1.1.1 From Maxwell's equations to the vector wave equations . . . 6

1.1.2 Derivation of the electric and magnetic fields 8

1.1.3 The eigenvalue equation for the propagation constant 9

1.2 Optical microfibres 11

1.2.1 Principle of operation 11

1.2.2 Fabrication 14

1.2.3 Fibre materials and transmission properties 15

2 Diameter measurement of optical microfibres using harmonic generation 21

2.1 Nonlinear optics 21

2.1.1 Polarization density 21

2.1.2 Fibre nonlinearity 24

2.2 Observed nonlinear effects in optical microfibres 24

2.2.1 Spectral broadening 25

2.2.2 Harmonic generation 29

2.3 Concept of microfibre diameter measurement 32

2.4 Measurement of the harmonic spectral response 33

2.5 Analysis of the harmonic spectral response 34
2.5.1 Interpretation of measured harmonic spectrum shape 34
2.5.2 Determination of the microfibre waist diameter 36
2.6 Verification using scanning electron microscope imaging 38
2.7 Optical damage 41
2.8 Conclusion 42

3 Switching photochromic molecules adsorbed to optical microfibres 45
3.1 Photochromism 45
3.1.1 General characteristics of photochromic systems 45
3.1.2 Classes of photochromic reactions 49
3.1.3 Photochromic molecules used here 50
3.2 Experimental prerequisites 52
3.2.1 Attaching organic dye molecules to microfibres 52
3.2.2 Detection of organic dye molecules adsorbed to microfibres . 53
3.3 Basic photoswitching 53
3.3.1 Optical setup 54
3.3.2 Absorbance spectrum during photoswitching 55
3.3.3 Photoswitching dynamics 57

4 Quantitative analysis of the photochromic processes 65
4.1 Reaction kinetics of the switching processes 65
4.1.1 Photobleaching: Exposure to white light 66
4.1.2 Photocolouration: Exposure to UV and white light 70
4.1.3 Molecules ratio in the photostationary state 71
4.2 Cyclability 76
4.2.1 Dependence on UV power 77
4.2.2 Dependence on number of adsorbed molecules 79

4.2.3 Photodestruction quantum yield 81
4.3 Summary and conclusion 83

5 Outlook **85**

5.1 Diameter measurement and harmonic generation 85
5.2 Photochromic molecules 86

Bibliography **89**

Acknowledgements **97**

Introduction

The idea of light guiding by total internal reflection goes back to J. Kepler in the 17th century and was first demonstrated by D. Colladon and J. Babinet in the 1840s [1]. They demonstrated the bending of light in a water stream and Colladon described the results: "*...once entering the stream [the light rays] encounter its surface under angle small enough to experience a total internal reflection; the same effect repeats at each new point of incidence, such that the light circulates in the transparent jet like in a canal, and follows all the turns*". From this discovery it took more than 100 years until optical waveguides had their breakthrough. The invention of the laser in 1960 stimulated the interest in low loss optical waveguides for optical communication. From the first applications in telecommunication industry the use of optical fibres developed in many directions. Besides information transmission, optical fibres found their way for example into medical applications [2], into optical fibre sensor technology [3], and doped with rare-earth elements they are used as high-power fibre lasers [4].

In the experiments presented in this thesis optical fibres which are tapered down to diameters on the order of one micrometre – optical microfibres (OMF) – are used. OMF can be produced from standard, commercially available optical fibres by the flame-brushing technique [5–8]. Contrary to a conventional optical fibre, where the light is weakly guided by the core-cladding interface, strong light guidance by the cladding-air interface occurs in OMF [9]. This results in tight confinement of the propagating mode with a mode area of $\sim \lambda^2$, where λ is the wavelength of the light. Thus, the light intensity is very high – not only inside the fibre but also in its evanescent field. At the same time the light remains confined over a length of up to several centimetres. For comparison, in a homogeneous material the depth of focus of a light beam focused to λ^2 is limited to a very short range on the order of λ. Thus we obtain about four orders of magnitude enhancement of the light-matter interaction by guiding a light beam with an OMF. The properties of OMF make them an excellent tool for nonlinear optics (high intensity) and light-matter interaction experiments with the fibre surrounding (strong evanescent field).

The combination of the high intensity due to spatial confinement with the tempo-

ral confinement of a pulsed laser results in even higher peak intensities. First experiments on nonlinear spectral broadening by enhanced self-phase modulation in OMF using femtosecond laser pulses had been performed [10], and were later continued with supercontinuum generation in OMF [11,12]. Moreover, third-harmonic generation in OMF has been theoretically predicted and experimentally observed [13–15]. Despite the centrosymmetric properties of silica second-harmonic light was also obtained [15].

After the mathematical description of light propagation in step-index optical fibres and the introduction of OMF in Chap. 1, I present measurements on nonlinear effects in OMF in Chap. 2. A pulsed laser with picosecond pulse duration was used to obtain self-phase modulation (SPM) as well as second- and third-harmonic generation (SHG, THG). It was found that the phase-matching condition for harmonic generation allows us to unambiguously deduce the fibre diameter from the wavelength of the measured harmonic light.

The second characteristic feature of OMF – the strong evanescent field – allows efficient light-matter interaction experiments for example with surface-adsorbates or vapours. In previous experiments in our group ultra-sensitive absorption spectroscopy of surface-adsorbed organic dye molecules has been demonstrated [16]. After the passive observation of organic dyes, the next level of complexity is the optical manipulation of molecules. Candidates for active optical switching are organic photochromic molecules which are part of ongoing research in physical chemistry. The characteristic property of these molecules can be deduced from the word "photochromic": "photo" means light-induced and "chromic" means a change in the absorption spectrum. Accordingly, photochromism is simply defined as a reversible light-induced change of the absorption spectrum. Experiments with photochromic molecules are usually performed using photochromic molecules in solution [17, 18], photochromic films prepared by spin-coating [19, 20] or vacuum evaporation [21], and photochromic molecules embedded in a polymer matrix [22, 23]. The main drawback of organic photochromic molecules is chemical degradation due to ultraviolet (UV) light leading to a reduction of the performance. With the review article by Irie [24] reporting on fatigue resistant diarylethenes, however, the research was intensified. In the same manuscript the basic potential for applications as optical switches and data storage was discussed.

The combination of OMF with surface-adsorbed photochromic molecules is a system providing good optical access to the internal states of the molecules. For evaluating the prospects of the system the applicability of preparation, detection

and manipulation of photochromic molecules adsorbed to OMF has to be studied. In the second part of this thesis (Chap. 3 and 4) I therefore present measurements of the light-induced switching dynamics of surface-adsorbed photochromic molecules. The switching dynamics were mathematically modelled in a rough approximation using a rate equation model. With this simple model I was able to extract the important and intuitive main properties of the systems.

Chapter 1

Step-index optical fibres

The experimental basis of this work are step-index optical fibres, i.e. dielectric waveguides with a circular step-index profile. In the first section of this chapter I will discuss the light propagation in step-index optical fibres. For this purpose I sketch the solution of Maxwell's equations for the fibre geometry. From the results the main properties of OMF are derived. In the second part of this chapter I will introduce the basic concept of OMF.

1.1 Light propagation in step-index optical fibres

The most common optical fibres consist of a fused silica (SiO_2) core doped with germanium (Ge) and a pure fused silica cladding. The germanium increases the refractive index of the fibre core n_{core} by 0.3 % to 0.4 % in comparison to the refractive index of the fibre cladding n_{clad}. This provides light guidance along the z axis by total internal reflection at the interface between core and cladding. Figure 1.1 illustrates the corresponding optical fibre geometry (a) and the radial refractive index distribution (b). A single-mode fibre for the visible and near infrared wavelength range has typically a fibre core diameter of 3 µm to 5 µm and a fibre cladding diameter of 125 µm. Due to the small refractive index difference between core and cladding the light does not propagate in the core only, the field also extends transversally into the cladding. The light intensity in the cladding decreases approximately exponentially in the radial direction with a decay length of a few micrometres. Therefore, the intensity at the cladding-air interface can be neglected and the light is guided by the core-cladding interface only.

Optical microfibres are tapered optical fibres with a cladding diameter of about one micrometre and a core diameter of few tens of nanometres. In these fibres the light is guided by the cladding-air interface rather than by the core-cladding interface for two reasons. First, the very thin fibre core is more than one order of

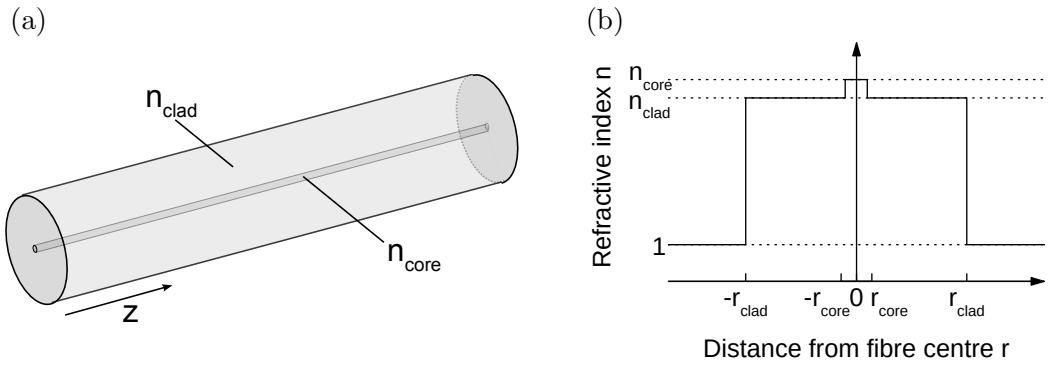

$$n(r) = \begin{cases} n_{\text{core}}, & 0 < r < r_{\text{core}} \\ n_{\text{clad}}, & r_{\text{core}} \leq r < r_{\text{clad}} \\ 1, & r_{\text{clad}} \leq r < \infty \end{cases} \tag{1.1}$$

Figure 1.1: (a) The schematic drawing of a step-index optical fibre with the light propagating along the z axis. (b) The radial refractive index distribution of a step-index optical fibre.

magnitude smaller than the wavelength of the used light ($\lambda > 300$ nm). Second, the refractive index difference at the cladding-air interface is more than 100 times larger than the refractive index difference at the core-cladding interface. Therefore, the core has a marginal influence on the guiding properties and can be neglected.

To describe light propagation in unprocessed optical fibres and in optical microfibres the two-layer system is a valid approximation [25, 26]. The corresponding waveguide geometry is illustrated in Fig. 1.2a and the radial refractive index distribution in Fig. 1.2b. The light propagation in cylindrical two-layer waveguides has been theoretically well studied and their profile is one of the few waveguide geometries with exact solutions. The derivation of the full vector solutions is sketched in the following, the details of these calculations can be found in chapter 12 and 30 of [25].

1.1.1 From Maxwell's equations to the vector wave equations

To understand light propagation in a waveguide the electric and magnetic fields can be derived from Maxwell's equations. The solutions are the guided modes of the waveguide. For the step-index optical fibre the time dependence of the fields can be separated by assuming an $\exp(-\mathrm{i}\omega t)$-dependence of the electric and magnetic field, where t is the time and ω the angular frequency of light. Due to the

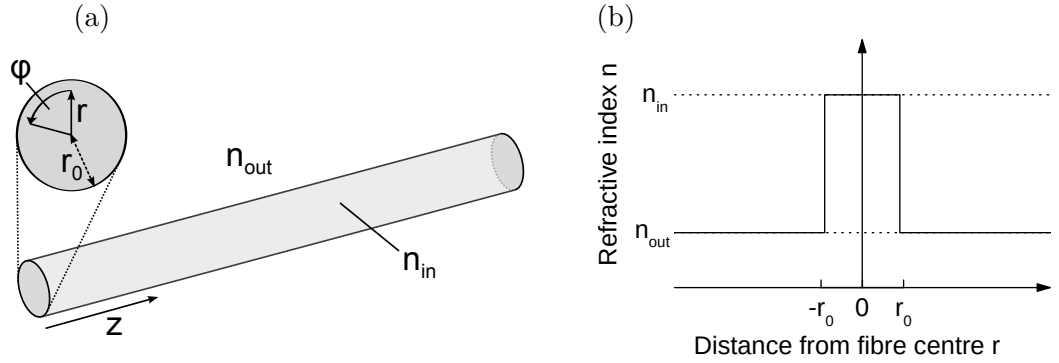

$$n(r) = \begin{cases} n_{\text{in}}, & 0 < r < r_0 \\ n_{\text{out}}, & r_0 \leq r < \infty \end{cases} \tag{1.2}$$

Figure 1.2: The cylindrical two-layer waveguide structure used for the calculations. (a) The schematic drawing of the waveguide in cylindrical coordinates with the light propagating along the z axis. (b) The radial refractive index plot of a step-index optical fibre. In case of the unprocessed optical fibre applies $n_{\text{in}} = n_{\text{core}}$, $n_{\text{out}} = n_{\text{clad}}$, and $r_0 = r_{\text{core}}$. In case of the OMF applies $n_{\text{in}} = n_{\text{clad}}$, $n_{\text{out}} = n_{\text{air}}$, and $r_0 = r_{\text{clad}}$.

cylindrical geometry of the optical fibre we use cylindrical coordinates for the spatial dependence of the fields. The light propagates along the optical axis z and the fibre cross section lies in the $r\varphi$-plane perpendicular to z, as illustrated in Fig. 1.2. Since the optical fibre cross section does not change along z, in particular $n = n(r)$, the z-dependence of the fields can be also separated. Under these assumptions, the ansatz for the electric and magnetic field can be chosen as

$$\mathbf{E}(r, \varphi, z, t) = \mathbf{e}(r, \varphi) \cdot \exp(\mathrm{i}\beta z) \cdot \exp(-\mathrm{i}\omega t) \tag{1.3}$$

$$\mathbf{H}(r, \varphi, z, t) = \mathbf{h}(r, \varphi) \cdot \exp(\mathrm{i}\beta z) \cdot \exp(-\mathrm{i}\omega t) \tag{1.4}$$

where $\beta = k_0 \cdot n_{\text{eff}}$ is the propagation constant, $k_0 = 2\pi/\lambda$ the free-space wave number with λ the free-space wavelength, and n_{eff} the effective refractive index. The propagation along z is therefore described by β and the z-independent modal fields by $\mathbf{e}(r, \varphi)$ and $\mathbf{h}(r, \varphi)$. Since the optical fibre is a nonmagnetic medium, the magnetic permeability μ is assumed to be equal to the free-space magnetic permeability μ_0. Moreover, the permittivity ϵ is related to the refractive index n by $\epsilon = n^2$. The time-independent Maxwell equations can be then expressed as

$$\nabla \times \mathbf{E} = \mathrm{i}\sqrt{\mu_0/\epsilon_0}\; k_0 \mathbf{H}; \qquad \nabla \times \mathbf{H} = \mathbf{J} - \mathrm{i}\sqrt{\mu_0/\epsilon_0}\; k_0 n^2 \mathbf{E} \tag{1.5}$$

$$\nabla \cdot (n^2 \mathbf{E}) = \rho/\epsilon_0; \qquad \nabla \cdot \mathbf{H} = 0 \tag{1.6}$$

where ϵ_0 is the vacuum permittivity, ρ the total charge density and $\mathbf{J}$ the total current density. For further simplification the field vectors $\mathbf{e}(r,\varphi)$ and $\mathbf{h}(r,\varphi)$ are separated into components transverse ($\mathbf{e}_\mathrm{t}$, $\mathbf{h}_\mathrm{t}$) and longitudinal ($e_\mathrm{z}\widehat{\mathbf{z}}$, $h_\mathrm{z}\widehat{\mathbf{z}}$) to the optical fibre axis, where $\widehat{\mathbf{z}}$ is the unit vector along z. The modal fields can be then written as

$$\mathbf{e}(r,\varphi) = \mathbf{e}_\mathrm{t} + e_\mathrm{z}\widehat{\mathbf{z}} \tag{1.7}$$

$$\mathbf{h}(r,\varphi) = \mathbf{h}_\mathrm{t} + h_\mathrm{z}\widehat{\mathbf{z}} \tag{1.8}$$

By eliminating either $\mathbf{E}$ or $\mathbf{H}$ in Eq. (1.5), Maxwell's equations for a source-free waveguide ($\mathbf{J} = 0$, $\rho = 0$) can be expressed in MKS units by the homogeneous vector wave equations

$$\left(\nabla^2 + n^2 k_0^2 - \beta^2\right)\mathbf{e} = -\left(\nabla_\mathrm{t} + \mathrm{i}\beta\widehat{\mathbf{z}}\right)\mathbf{e}_\mathrm{t} \cdot \nabla_\mathrm{t} \ln n^2 \tag{1.9}$$

$$\left(\nabla^2 + n^2 k_0^2 - \beta^2\right)\mathbf{h} = \left\{\left(\nabla_\mathrm{t} + \mathrm{i}\beta\widehat{\mathbf{z}}\right) \times \mathbf{h}\right\} \times \nabla_\mathrm{t} \ln n^2 \tag{1.10}$$

where $n = n(r)$ is the refractive index distribution specified in Eq. (1.2) and ∇_t, ∇^2 are the differential operators, for example defined in [25], table 30-1.

1.1.2 Derivation of the electric and magnetic fields

The approach to construct the fields is to solve Eq. (1.9) and (1.10) separately for the inner and outer dielectric medium and to use boundary conditions to calculate the amplitudes. Since the refractive index within the inner or the outer dielectric medium is constant we infer that $\nabla_t \ln n^2 = 0$ and Eq. (1.9) and (1.10) simplify to

$$\left(\nabla^2 + n^2 k_0^2 - \beta^2\right)\mathbf{e} = 0 \tag{1.11}$$

$$\left(\nabla^2 + n^2 k_0^2 - \beta^2\right)\mathbf{h} = 0 \tag{1.12}$$

For the circular step-index waveguide we obtain for e_z in cylindrical coordinates (correspondingly for the magnetic field by exchanging e_z by h_z)

$$\left\{\frac{\partial^2}{\partial R^2}+\frac{1}{R}\frac{\partial}{\partial R}+\frac{1}{R^2}\frac{\partial^2}{\partial \varphi^2}+U^2\right\}e_\mathrm{z} = 0 \qquad \text{for } 0 \le R < 1 \tag{1.13}$$

$$\left\{\frac{\partial^2}{\partial R^2}+\frac{1}{R}\frac{\partial}{\partial R}+\frac{1}{R^2}\frac{\partial^2}{\partial \varphi^2}-W^2\right\}e_\mathrm{z} = 0 \qquad \text{for } 1 < R < \infty \tag{1.14}$$

where

$$R=\frac{r}{r_0}, \qquad U=r_0\sqrt{k_0^2 n_\mathrm{in}^2-\beta^2}, \qquad W=r_0\sqrt{\beta^2-k_0^2 n_\mathrm{out}^2} \tag{1.15}$$

Equation (1.13) and (1.14) and the corresponding equations for h_z are solved using the boundary conditions at the interface. The boundary conditions for nonmagnetic media imply that all magnetic field components (h_z, h_φ, h_r) and the electric field components tangential to the interface (e_z, e_φ) are continuous.

The transverse field components e_φ, e_r, h_φ, and h_r are calculated from e_z, h_z and the relationship between the field components obtained from Maxwell's equations, see section 30-2 of [25]. The results for all six field components can be found in table 12-3 of [25]. The solutions of the vector wave equations can be categorized into three classes: The hybrid (HE, EH) modes with all six field components being non-zero and the azimuthally symmetric transverse modes, which are divided into the transverse electric (TE) modes with $e_z = 0$ and the transverse magnetic (TM) modes with $h_z = 0$. For the full description of light propagation the propagation constant β is needed, which will be derived in the next section.

1.1.3 The eigenvalue equation for the propagation constant

With the boundary condition of continuous tangential field components at the interface the solutions of the fields lead to an eigenvalue equation for the propagation constant β. According to [25], the eigenvalue equation can be expressed for the hybrid modes as

$$\left\{\frac{J_\nu'(U)}{UJ_\nu(U)}+\frac{K_\nu'(W)}{WK_\nu(W)}\right\}\left\{\frac{J_\nu'(U)}{UJ_\nu(U)}+\frac{n_\mathrm{out}^2}{n_\mathrm{in}^2}\cdot\frac{K_\nu'(W)}{WK_\nu(W)}\right\} = \left(\frac{\nu\beta}{kn_\mathrm{in}}\right)^2\left(\frac{V}{UW}\right)^4 \tag{1.16}$$

and for transverse modes as

$$\frac{J_1(U)}{UJ_0(U)} + \frac{K_1(W)}{WK_0(W)} = 0 \qquad \text{for TE modes} \tag{1.17}$$

$$\frac{J_1(U)}{UJ_0(U)} + \frac{n_{\text{out}}^2}{n_{\text{in}}^2} \cdot \frac{K_1(W)}{WK_0(W)} = 0 \qquad \text{for TM modes} \tag{1.18}$$

where J_ν is the Bessel function of the first kind, K_ν the modified Bessel function of the second kind, and V the waveguide parameter which is given by

$$V = k_0 r_0 \sqrt{n_{\text{in}}^2 - n_{\text{out}}^2} \tag{1.19}$$

Since the eigenvalue equations are transcendental they have to be solved numerically. Eq. (1.16) is quadratic in $J_\nu'(U)/UJ_\nu(U)$ and thus we obtain two different eigenvalue equations corresponding to the two roots. This leads to two sets of solutions for the hybrid modes, the $\text{HE}_{\nu\text{m}}$ and $\text{EH}_{\nu\text{m}}$ modes. The solutions are denoted with two indices, ν and m, where ν originates from the detailed calculations of the fields and describes the azimuthal dependence, and m denotes the m-th root of the eigenvalue equations. For the transverse modes the solutions are denoted as $\text{TE}_{0\text{m}}$ and $\text{TM}_{0\text{m}}$. The first index ν being zero indicates that the transverse modes are, as mentioned before, azimuthally symmetric.

To obtain the numerical solutions for the normalized propagation constant β/k_0 of the guided modes we developed a MATLAB toolbox [27]. The solutions for β/k_0 of the guided modes are shown in Fig. 1.3. For all guided modes the propagation constant is between $n_{\text{out}}k_0$ and $n_{\text{in}}k_0$. The number of propagating modes depends on the V-parameter. For example, for $V < 2.405$ only the fundamental mode HE_{11} can propagate and the waveguide is called single-mode.

In Fig. 1.3a the result for an optical fibre with a large refractive index step is illustrated describing light propagation in an OMF. In Fig. 1.3b the corresponding graph for a small refractive index step is shown describing light propagation in an unprocessed optical fibre. In the latter case some of the modes are degenerate. Due to the small refractive index step the modes are "weakly bound" and the hybrid modes can be represented by the linearly polarized LP modes. The fundamental HE_{11} mode is denoted as LP_{01}, and the three next higher modes TE_{01}, TM_{01}, and HE_{21} are denoted as LP_{11}. The LP modes have negligible field components in the direction of propagation and are close to free-space transverse electromagnetic modes ($e_\text{z} = h_\text{z} = 0$) [28].

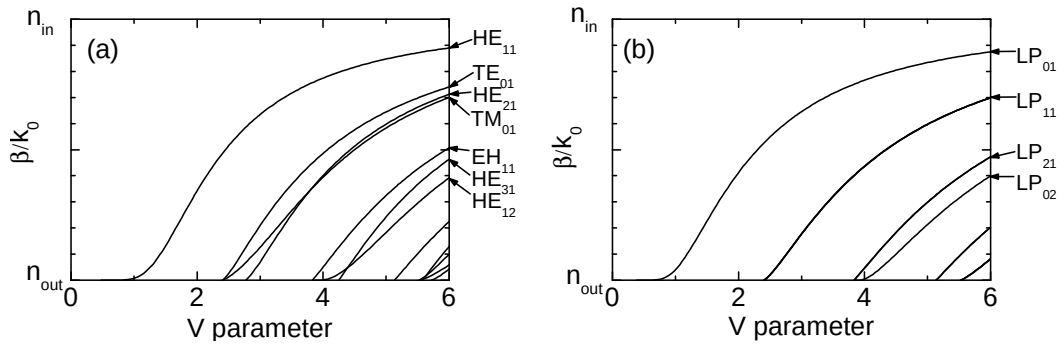

Figure 1.3: Numerical solution of the transcendental eigenvalue equation. The normalized propagation constant β/k_0 is plotted versus the fibre parameter V. (a) Hybrid modes of an optical fibre with large refractive index step. Inner material: pure fused silica, outer material: air, $\lambda = 900$ nm. (b) Linear polarized modes of an optical fibre with small refractive index step. Inner material: Ge-doped silica, outer material: pure fused silica, $\lambda = 900$ nm.

The calculations of the LP modes in an optical fibre with small refractive index step can be enormously simplified because of possible approximations leading to a scalar wave equation. However, since the full vectorial solution is required for the description of light propagation in an OMF, these calculation are not carried out here.

1.2 Optical microfibres

1.2.1 Principle of operation

The sketch of an OMF is shown in Fig 1.4a. It consists of an unprocessed optical fibre section, the down-taper, the micrometre waist, the up-taper which is symmetric to the down-taper, and a second unprocessed optical fibre section.

The unprocessed optical fibre section is typically a single-mode fibre for the used wavelength meaning that only the fundamental mode can propagate. The light is guided by the core-cladding interface with a small refractive index step. Therefore, the fundamental mode is the linearly polarized LP_{01} mode which is propagating mainly inside the core, as illustrated in Fig. 1.4b.

In the down-taper, the fibre diameter starts to decrease and the light is gradually more tightly confined until the mode field diameter reaches a minimum. When the diameter decreases further, the core-cladding interface does not confine the light any

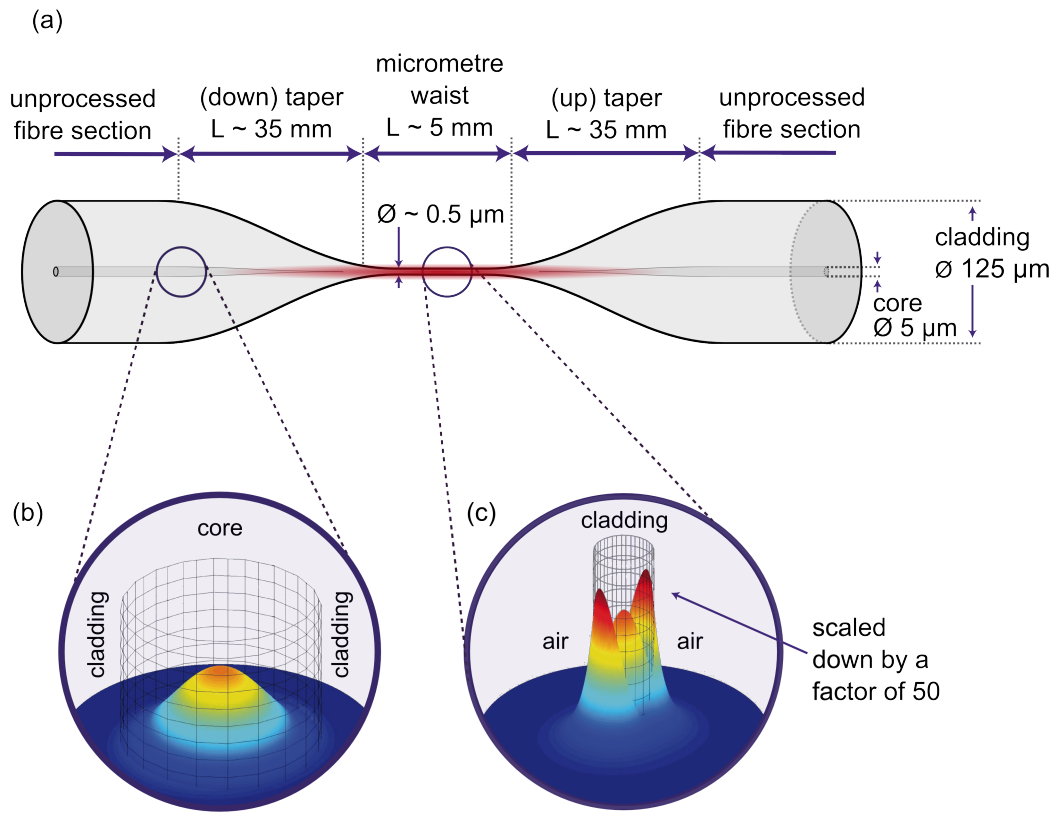

Figure 1.4: (a) Sketch of an OMF. The two bottom images show the intensity distribution of the quasi-linearly polarized HE_{11} mode in the unprocessed single-mode fibre (b) and in the OMF (c). The intensity distributions were calculated using our MATLAB toolbox [27].

more and the light expands into the cladding. In this section the light is guided by both the core-cladding and the cladding-air interface. An even further decrease of the fibre diameter reduces the influence of the core-cladding interface and the light is then guided only by the cladding-air interface with the large refractive index step. To minimize transmission losses this mode conversion has to be adiabatic meaning that the fundamental mode does not couple to higher transverse or radiative modes. The requirement for adiabatic taper transition has been analysed [29, 30] and can be achieved by ensuring shallow slopes with angles of a few milliradians.

When the light reaches the OMF waist with a submicrometre diameter the intensity increases by up to two orders of magnitude, see Fig. 1.4c. This tight confinement is maintained for several millimetres over the whole length of the microfibre waist. Moreover, up to 50 % of the light propagates outside the fibre, as the evanes-

cent field, providing excellent conditions for light-matter interaction experiments with gases or surface-adsorbates. At the up-taper, which is symmetrical to the down-taper, the mode conversion is then reversed.

The intensity distribution at the microfibre waist depends strongly on the waist diameter and the wavelength of the light. For modes independent of the azimuthal angle φ, like all transverse modes and the circularly polarized hybrid modes, the intensity distribution can be plotted versus the microfibre waist diameter. This is shown in Fig. 1.5a for the circularly polarized fundamental mode HE_{11} with $\lambda = 900$ nm and varying fibre waist diameter. The fibre diameter can be tailored in such a way that, depending on the requirements of the experiment, the intensity at the fibre centre or at the fibre surface is maximized. E.g., for $\lambda = 900$ nm the

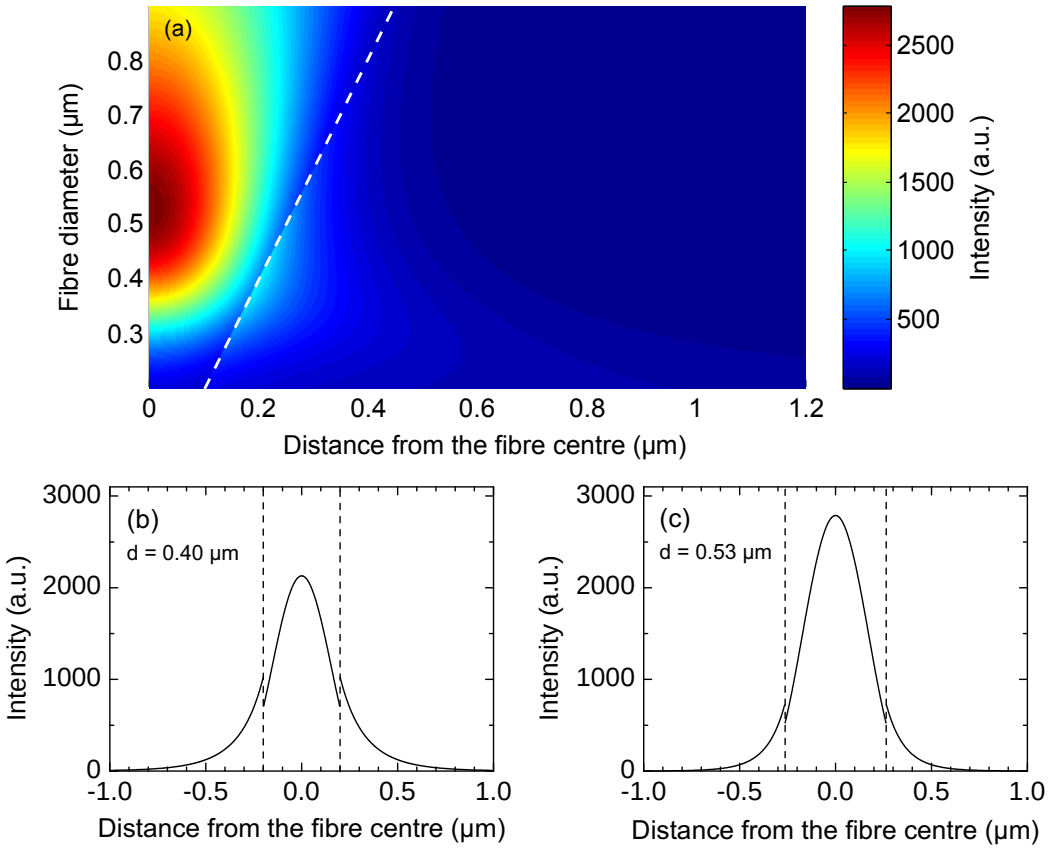

Figure 1.5: Intensity distribution of the circularly polarized HE_{11} mode at the wavelength of 900 nm shown as a colour-coded 3D plot (a) and as 2D plots for the two specific fibre diameters of $d = 0.40$ µm (b) and $d = 0.53$ µm (c). The dashed lines illustrate the fibre surface. Calculated using our MATLAB toolbox [27].

intensity of the circularly polarized HE_{11} mode at the fibre surface is maximized at the fibre diameter of 0.40 µm (see Fig. 1.5b), and at the fibre centre at the fibre diameter of 0.53 µm (see Fig. 1.5c). To avoid confusion due to similar values of fibre diameters and wavelengths, I denote the fibre diameter in micrometres and the wavelength in nanometres throughout the thesis.

1.2.2 Fabrication

OMF are produced by tapering commercial single-mode optical fibres using the flame-brushing technique [5–8]. A sketch of the pulling procedure is shown in Fig. 1.6. The optical fibre is fixed with strong magnets on two computer-controlled precision translation stages. A fibre section of 1 mm length is heated with a pure hydrogen-oxygen flame to 1500 °C. At this temperature the silica becomes viscous and can be tapered by pulling at both ends. To evaluate the success of a pulling process, the transmission through the fibre is monitored during tapering using a light source and a detector. We use either a diode laser with a wavelength of

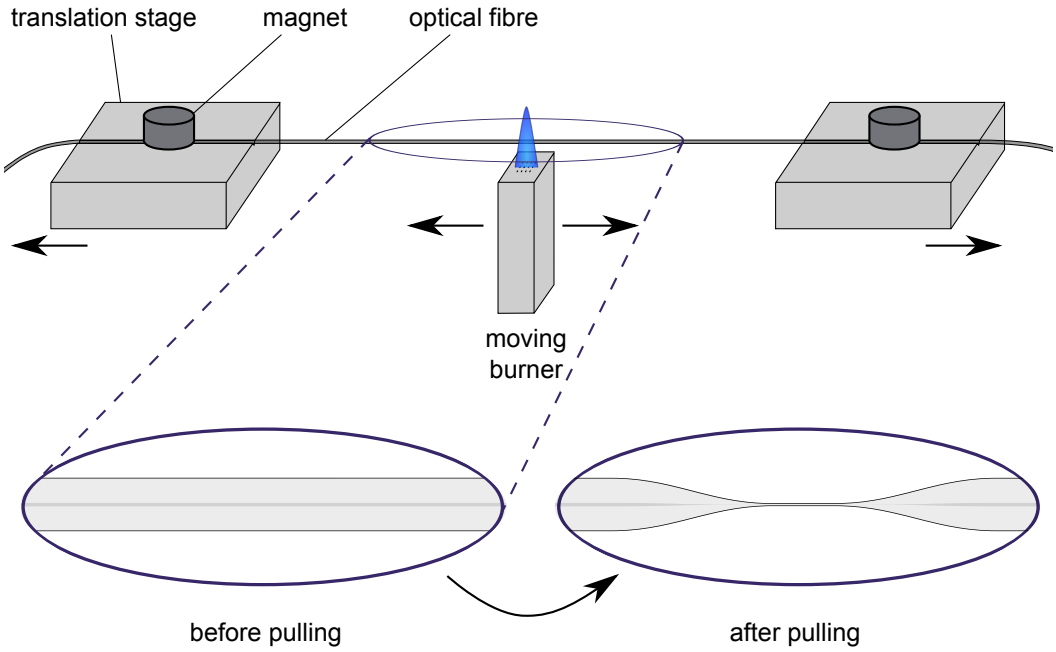

Figure 1.6: The commercial single-mode optical fibre is fixed on two translation stages with strong magnets. By heating the fibre with a moving hydrogen-oxygen flame and simultaneous pulling at both ends the optical fibre is tapered to the desired shape. The two insets show the optical fibre before and after tapering.

852 nm and a photodiode or a broadband deuterium-halogen lamp and a spectrometer. The movement of the translation stages and the heater are calculated using a mathematical model [31]. This allows producing tapers with a predefined shape. To ensure adiabatic transitions all OMF for my measurements have a taper shape with three conical sections. The slopes of the three sections are 3 mrad, 2 mrad, and 3 mrad. The shallower slope in the intermediate taper section is used to prevent losses during the conversion of the core-guided modes to the cladding-guided modes. The waist diameters of the OMF used in my experiments are in the range of 0.3...0.5 µm. The length of the whole tapered section is 7.5 cm and is subdivided into the two taper sections each 3.5 cm in length and the waist 5 mm in length.

After pulling, the OMF are inserted to a metallic fibre holder and fixed with UV curing glue. The metallic fibre holder protects the tapered OMF section mechanically and from dust.

1.2.3 Fibre materials and transmission properties

For the experiments of third-harmonic generation in Chap. 2 as well as for switching photochromic molecules in Chap. 3 and 4 it is necessary to use UV-light-transmitting OMF. For this purpose the transmission properties of different fibre types were measured.

There are two basic types of silica-based step-index optical fibres available, the core-doped fibres and the cladding-doped fibres. The core-doped fibres consist of a pure fused silica cladding and a silica core doped with a material increasing the refractive index. The most common doping material is Ge which has a low absorption in the visible and infrared (IR) wavelength range, but an enhanced absorption in the UV. The alternative are cladding-doped fibres with a pure fused silica core and a silica cladding doped with an index-lowering material, most commonly fluorine (F). The advantage of this fibre type is the low UV-light absorption of the pure silica core.

F-doped-cladding optical fibres

During tapering of the single-mode fibre Nufern S630-HP with F-doped cladding we observed that the transmission of 852 nm light through the fibre dropped to zero reproducible. With an IR viewer we checked that the light was lost in the down-taper and no light reached the microfibre waist. A possible explanation might be the high diffusion rate of fluorine. During heating, the fluorine can diffuse from

the cladding into the core and therefore the refractive index step between core and cladding, which is essential for light guiding, smears out or might even vanish [32].

Ge-doped-core optical fibres

Unlike the F-doped-cladding fibres, the Ge-doped-core fibres can be tapered without losing the light guiding properties. To estimate the range of usable wavelength with the Ge-doped-core fibres the spectral transmission characteristics of the untapered fibres have to be known. The fibre manufacturers specify the transmission of their fibres only around the design wavelength. For the single-mode fibre Fibercore SM800, which we successfully used in previous experiments, the design wavelength is 830 nm.

The experimental setup for measuring the spectral transmission of the SM800 fibre is illustrated in Fig. 1.7. At both ends of an SM800 fibre a piece of pure silica core fibre with F-doped cladding S630-HP was connected by arc fusion splicing [33]. These two S630-HP ends were permanently connected to a deuterium-halogen lamp (Avantes DH-S) with a continuous spectrum from 215–2500 nm and a spectrometer (Ocean Optics HR2000). The transmission through this three-section fibre structure was measured for different lengths L of the SM800 fibre. After each measurement the SM800 fibre was cut, shortened at one side, and then respliced to the S630-HP fibre. At the last measurement, for $L = 0$, the two remaining S630-HP fibres sections were directly spliced together. The spectrum for $L = 0$ was used as the reference for all other measurements, i.e. this spectrum corresponds to 100 % transmission. The resulting relative transmission spectra for different lengths L are plotted in Fig. 1.8a. All curves are below 100 % even in the visible wavelength

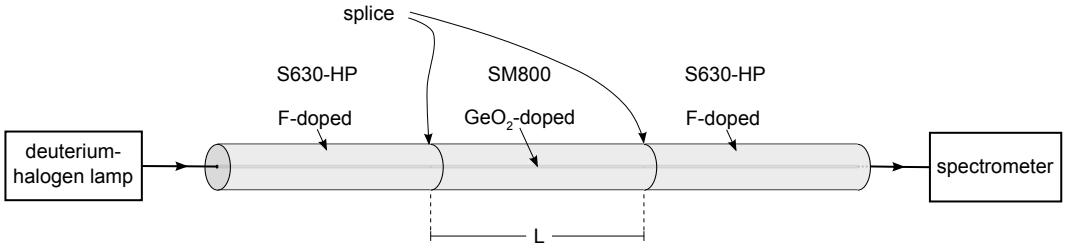

Figure 1.7: Experimental setup for the UV absorption measurement of the SM800 fibre (Ge-doped core). The two outer S630-HP fibre sections (F-doped cladding) are permanently connected to the deuterium-halogen lamp DH-S and the spectrometer. The centre section of the SM800 fibre is spliced to the two S630-HP fibres.

range where no significant absorption of the SM800 fibre is expected. This can be attributed to losses at the additional second splice when measuring the spectra for $L \neq 0$, whereas the reference spetrum was obtained with a fibre containing only one splice. Moreover, the strong and unsystematic scattering in the visible wavelength range indicates that the splice quality varies. Therefore, the measurement error is estimated to ± 10 %. At shorter wavelengths, below 370 nm, additional absorption occurs. For a fibre length of $L = 25$ cm the transmission for $\lambda < 340$ nm decreased to ~ 4 %. Exemplatory the transmission at 330 nm was analysed for all measured fibre lengths L, see Fig. 1.8b. Despite the strong scattering of the curves as well as the additional offset due to the losses at the second splice, the decrease is well described by an exponential function. The resulting exponential fit function is: $T = 87\ \% \cdot \exp\left(-L/(6.9\ \text{cm})\right)$.

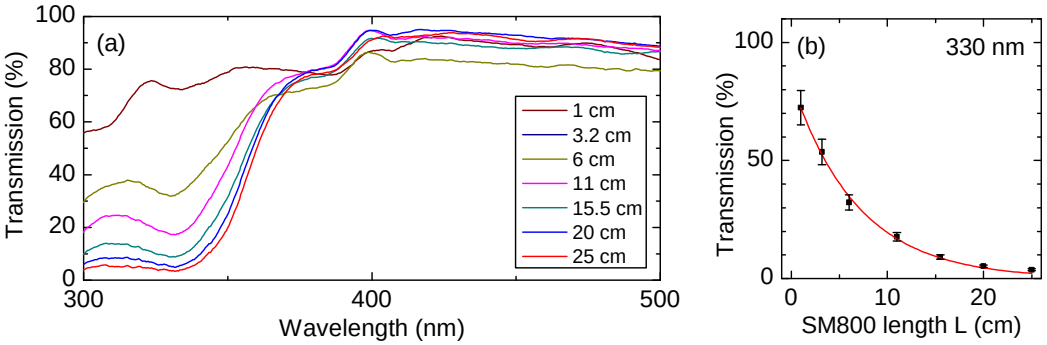

Figure 1.8: (a) Transmission spectra of the spliced fibre with different SM800 fibre lengths L. 100 % corresponds to the transmission of the single-piece S630-HP fibre. (b) Corresponding transmission at $\lambda = 330$ nm. The relative error for all measurements is estimated to be ± 10 % of the transmission.

Fabrication of spliced UV-transmitting OMF

Ge-doped-core SM800 fibres can be tapered, but the UV absorption with an exponential decay constant of $\sim$7 cm is strong. Thus, the length of the untapered SM800 fibre has to be minimized. However, to connect the OMF to the light sources, detectors or collimation lenses, the fibre ends have to be at least tens of centimetres. The approach to produce an UV-transmitting OMF is to taper an SM800 fibre with the F-doped-cladding fibre S630-HP used as fibre ends. The three fibre sections are permanently connected by fusion splicing, similar to the design in Fig. 1.7. The length of the heated SM800 fibre section depends on the pulling trajectory, i.e. the

burner and translation stage movement, and is calculated by the pulling machine control program. The fibre is carefully aligned on the two translation stages so that only the SM800 fibre section is heated and tapered.

The spectral transmission during and after pulling of this fibre configuration is shown in Fig. 1.9. The final transmission illustrated with the continuous curve can be classified in three regions, see Tab. 1.1. Considering the modes propagating in the S630-HP fibre, the manufacturer specifies single-mode operation at wavelengths above (590 ± 30) nm [34], i.e. in this regime only the fundamental mode LP_{01} is guided. Since the fundamental mode is generally guided in the whole OMF including the tapered part, the losses for $\lambda > 590$ nm are small. For $\lambda < 590$ nm, the LP_{11} mode propagates additionally to the fundamental LP_{01} mode in the untapered S630-HP fibre. In the taper sections of the OMF, the adiabaticity criterion is more strict for higher modes and therefore they are more easily lost. This explains the transmission drop for $\lambda < 590$ nm after the pulling is finished. Similar to this, there is a second transmission drop for wavelengths below 400 nm, which can be attributed to taper losses of further higher modes (LP_{21}, LP_{02}) propagating in the untapered S630-HP fibre.

It is noticeable that at an intermediate pulling step, shown as the dashed curve, the transmission is reduced to 60 % for wavelengths between 480 nm and 590 nm

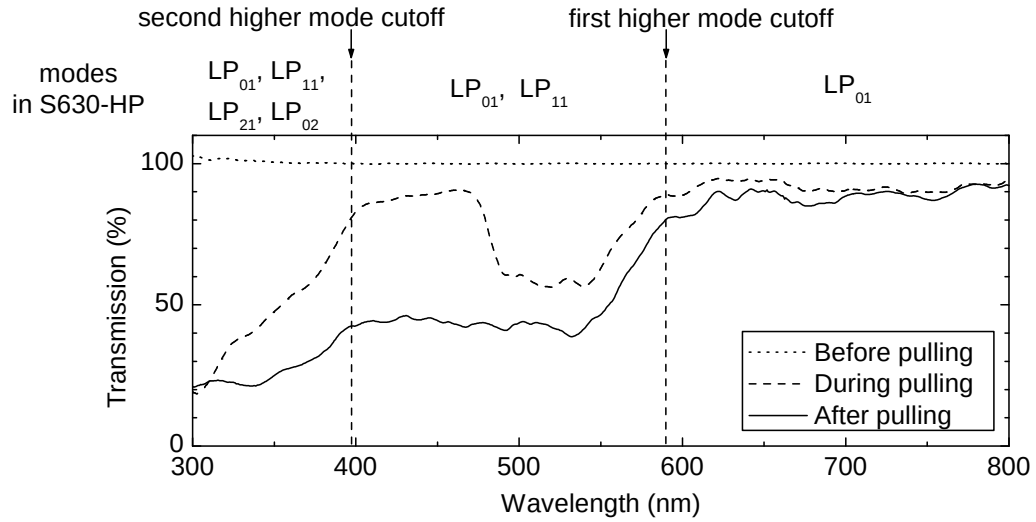

Figure 1.9: Transmission before, during and after pulling of a spliced S630-HP – SM800 – S630-HP fibre with a final waist diameter of 0.44 µm and a waist length of 5 mm. The two vertical dashed lines indicate the higher mode cutoff wavelengths in the S630-HP fibre.

Wavelength (nm)	Modes in S630-HP	Transmission (%)
300–400	LP_{01}, LP_{11}, LP_{21}, LP_{02}	> 20
400–590	LP_{01}, LP_{11}	> 40
590–800	LP_{01}	> 85

Table 1.1: Spectral transmission of the spliced OMF with a final waist diameter of 0.44 µm and a waist length of 5 mm. For each transmission regime the corresponding modes propagating in the untapered S630-HP fibre are noted.

whereas it remains above 85 % for wavelengths between 400 nm and 480 nm. This means that the LP_{11} mode is already lost for $\lambda > 480$ nm but still guided for $\lambda < 480$ nm. This can be understood from the conversion characteristics of the core modes to the cladding modes in the taper section. This conversion occurs for long wavelengths at larger fibre diameters, and therefore earlier in the pulling procedure. Since the higher modes are lost during this conversion process, they are first lost at the long-wavelength edge.

The measured transmission properties of Fig. 1.9 demonstrate that this OMF design is applicable for measurements requiring transmission of UV light down to $\lambda = 300$ nm.

Chapter 2

Diameter measurement of optical microfibres using harmonic generation

To quantitatively understand and control light propagation in OMF it is crucial to know the submicrometre waist diameter precisely. The precision of our OMF fabrication process undergoes experimental limitations and was determined to ± 5 % [35]. In this chapter, I demonstrate a new technique for optical measurement of the submicrometre waist diameter. The method is based on the nonlinear effects of second- and third-harmonic generation and offers an accuracy of better than 2 %. For the implementation of the method we make use of nonlinear spectral broadening. I therefore first introduce nonlinear effects observed in OMF followed by the description of the OMF diameter measurement.

2.1 Nonlinear optics

Nonlinear optical phenomena originate from the nonlinear response of a material to an applied optical field. A general description of nonlinear optics can be found for example in [36, 37], and in particular for optical fibres in [38].

2.1.1 Polarization density

In dielectric media an electric field causes a separation of bound charges. This leads to a local electric dipole moment and is macroscopically described by the density of induced dipole moments, the polarization density $\mathbf{P}$. The response of the dielectric medium in turn influences the electric field $\mathbf{E}$ and thus the wave propagation in dielectric media. The wave propagation is described by the electromagnetic wave equation which can be derived from Maxwell's equations. For a source-free wave-

guide ($\mathbf{J} = 0$, $\rho = 0$) the electromagnetic wave equation is given by

$$\nabla^2\mathbf{E} - \frac{\partial^2}{\partial t^2}\left(\mu_0\epsilon_0\mathbf{E} + \mu_0\mathbf{P}\right) = 0 \tag{2.1}$$

In anisotropic media $\mathbf{P}$ is not necessarily parallel to $\mathbf{E}$. The vector components of $\mathbf{P}$ are defined as

$$P_i = \epsilon_0 \sum_j \chi_{ij}^{(1)}\ E_j + \epsilon_0 \sum_{jk} \chi_{ijk}^{(2)}\ E_j E_k + \epsilon_0 \sum_{jkl} \chi_{ijkl}^{(3)}\ E_j E_k E_l + \ldots \tag{2.2}$$

where $\mathbf{P}_i$ is the i-th component of the polarization density, $\mathbf{E}_j$ is the j-th component of the electric field and $\chi^{(n)}$ is the susceptibility tensor of rank $n+1$. For low light intensities the nonlinear contributions, i.e. all contribution of order two and above, are negligible and the absolute value of the polarization density is proportional to the absolute value of the electric field. For high intensities, the nonlinear components gain importance. The response of the material becomes nonlinear and additional optical effects can occur.

Many nonlinear effects are based on frequency-mixing processes. The lowest-order nonlinear frequency mixing processes contain three waves and can be derived from the second-order polarization density

$$P_i^{(2)}(\omega) = \epsilon_0 \sum_{jk} \chi_{ijk}^{(2)}(\omega;\omega_1,\omega_2) E_j(\omega_1) E_k(\omega_2) \tag{2.3}$$

The two incoming waves with the frequencies ω_1 and ω_2 can couple in different ways to a new wave with the frequency ω. The resulting second-order polarization densities $\mathbf{P}^{(2)}(\omega = \omega_1 + \omega_2)$, $\mathbf{P}^{(2)}(\omega = \omega_1 - \omega_2)$, $\mathbf{P}^{(2)}(\omega = 2\omega_1)$ correspond to the nonlinear effects of sum-frequency generation, difference-frequency generation and second-harmonic generation, respectively.

Since many relevant nonlinear effects in OMF can be deduced from the mixing of four waves, I explain the example of four-wave mixing (FWM) in more detail. In an FWM process three waves with the frequencies ω_1, ω_2, and ω_3 produce a forth wave with the frequency ω, and the responsible third-order polarization density can be expressed as

$$P_i^{(3)}(\omega) = \epsilon_0 \sum_{jkl} \chi_{ijkl}^{(3)}(\omega;\omega_1,\omega_2,\omega_3)\ E_j(\omega_1) E_k(\omega_2) E_l(\omega_3) \tag{2.4}$$

For the further description this equation is simplified by assuming scalar quantities and considering only FWM processes with incoming waves of the same frequency ω_0. The scalar polarization density $P(\omega_0)$ including the first and third-order is then given by

$$\begin{aligned} P(\omega_0) &= P^{(1)}(\omega_0;\omega_0,\omega_0,\omega_0) + P^{(3)}(\omega_0;\omega_0,\omega_0,\omega_0) \\ &= \epsilon_0\ \chi^{(1)}\ E(\omega_0) + \epsilon_0\ \chi^{(3)}\ E^3(\omega_0) \end{aligned} \tag{2.5}$$

With an applied electric field of the form $E(\omega_0,t) = E_0\cos(\omega_0 t)$ and by using the trigonometric transformation $\cos^3(x) = 3/4\cdot\cos(x) + 1/4\cdot\cos(3x)$, the time-dependent scalar polarization density can be expressed as

$$\begin{aligned} P(\omega_0,t) &= \epsilon_0\ \chi^{(1)}E_0\cos(\omega_0 t) + \frac{3}{4}\epsilon_0\ \chi^{(3)}E_0^3\cos(\omega_0 t) + \frac{1}{4}\epsilon_0\chi^{(3)}E_0^3\cos(3\omega_0 t) \\ &= \epsilon_0\left(\chi^{(1)} + \frac{3}{4}\chi^{(3)}\ E_0^2\right)E_0\cos(\omega_0 t) + \frac{1}{4}\epsilon_0\ \chi^{(3)}E_0^3\cos(3\omega_0 t) \end{aligned} \tag{2.6}$$

The two terms of this expression are responsible for different effects and are shortly presented in the following.

Optical Kerr effect

The first term of Eq. (2.6) describes the response of the material at the frequency of the applied field ω_0. In the parentheses appears a nonlinear contribution caused by the third-order susceptibility $\chi^{(3)}$. The polarization density apparently depends on the intensity $I \propto E_0^2$. This dependence can be described by an intensity-dependent refractive index

$$n(I) = n_0 + n_2 I \tag{2.7}$$

where n_0 is the linear refractive index and n_2 the second-order refractive index related to $\chi^{(3)}$. This phenomenon is known as the optical Kerr effect.

Third-harmonic generation

The second term of Eq. (2.6) is proportional to $\cos(3\omega_0 t)$ and describes the response of a nonlinear material with the tripled frequency. The corresponding process is the generation of one photon with the frequency $3\omega_0$ from three photons with the initial frequency ω_0 and is also known as third-harmonic generation (THG).

2.1.2 Fibre nonlinearity

Bulk fused silica provides a small third-order susceptibility $\chi^{(3)}$ which is responsible for example for THG. For the second-order susceptibility $\chi^{(2)}$ we have to consider the inversion symmetry of fused silica. We assume the second-order nonlinear polarization density $P^{(2)}(\omega_0, t)$ depending on the applied electric field $E(\omega_0, t) = E_0 \cos(\omega_0 t)$ as

$$P^{(2)}(\omega_0, t) = \epsilon_0 \chi^{(2)} (E_0 \cos(\omega_0 t))^2 \tag{2.8}$$

If we change the sign of the electric field $E(\omega_0, t) \rightarrow -E(\omega_0, t)$, the sign of the polarization density $P(\omega_0, t)$ must also change due to the inversion symmetry. We get

$$-P^{(2)}(\omega_0, t) = \epsilon_0 \chi^{(2)} (-E_0 \cos(\omega_0 t))^2 \tag{2.9}$$

$$-P^{(2)}(\omega_0, t) = \epsilon_0 \chi^{(2)} (E_0 \cos(\omega_0 t))^2 \tag{2.10}$$

Comparing Eq. (2.8) and Eq. (2.10) we obtain $\chi^{(2)} = 0$ meaning that second-order nonlinear effects – and similarly all even-order nonlinear effects – should not be possible in bulk fused silica. However, sum-frequency generation and SHG in optical fibres has been observed since the early 1980s [39, 40] with conversion efficiencies of 10^{-3}. Various approaches were used to explain the origin of SHG in optical fibres [39,41], including intrinsic birefringence in the fibre, surface contributions and electric multipole contributions from the bulk, but the true origin remained unclear. Later, much higher conversion efficiencies of 3–5 % were achieved [42]. Theoretical models explained the high efficiency by a photo-induced charge build-up, which leads to an spatially periodic electric DC field within the optical fibre breaking the fibre symmetry [43,44]. In recent experiments SHG was also demonstrated in OMF which was attributed to surface contributions [15], and a theoretical study of the prospects of surface and bulk multipole SHG in OMF followed [45].

2.2 Observed nonlinear effects in optical microfibres

Besides the nonlinearity of the material, the strength of nonlinear effects depends on the pump light intensity and the interaction length. In our experiments, intense pump light is provided by the high peak power of a Ti:sapphire laser with picosecond pulse duration. The strong confinement in the microfibre waist leads to a further intensity increase which is maintained over several millimetres interaction length. All this together provides excellent conditions for nonlinear interaction. The nonlinear effects that we have observed in OMF are described in the following.

2.2.1 Spectral broadening

In optical fibres several nonlinear effects cause spectral broadening of laser pulses [38,42,46,47], such as self-phase modulation (SPM), cross-phase modulation (XPM), stimulated Raman scattering, and supercontinuum generation. In OMF it has been observed that enhanced SPM using laser pulses with a pulse duration of 350 fs is a significant effect [10].

Calculation of SPM-broadened spectra

SPM occurs when a laser pulse travels through a nonlinear medium because of the time-dependent light intensity [38]. Due to the intensity-dependent refractive index caused by the optical Kerr effect (see Eq. (2.7)) an additional nonlinear phase shift Φ_{NL} is induced. This can be illustrated, for example, using a laser pulse with a normalized electric field amplitude $E_0(0,t)$ with Gaussian shape

$$E_0(0,t) = \exp\left(-\frac{t^2}{2\tau^2}\right) \tag{2.11}$$

where t is the time and τ is the full width at half maximum pulse duration. The z-dependence including the nonlinear phase shift can be then expressed as

$$E_0(z,t) = E_0(0,t)\exp\left(\mathrm{i}\Phi_{\mathrm{NL}}(z,t)\right) \tag{2.12}$$

where z is the propagation coordinate and Φ_{NL} is the nonlinear phase shift. From Eq. (2.12) one can see that the temporal shape of the pulse does not change because $|E_0(z,t)|^2 = \text{const}$. The nonlinear phase shift is given by

$$\Phi_{\mathrm{NL}}(z,t) = \frac{2\pi}{\lambda_0}\cdot n_2 \cdot I(t)\cdot z \tag{2.13}$$

By calculating the Fourier transform of the temporal pulse shape $E_0(z,t)$ we get the spectral intensity $S(\omega)$

$$S(\omega) = \left|\widetilde{E}_0(z,\omega)\right|^2 = \left|\int_{-\infty}^{\infty} E_0(0,t)\exp\left[\mathrm{i}\Phi_{\mathrm{NL}}(z,t) + \mathrm{i}(\omega-\omega_0)t\right]dt\right|^2 \tag{2.14}$$

where ω is the angular frequency and ω_0 the centre angular frequency of the initial spectrum. Figure 2.1 shows the normalized spectral intensity $S_{\mathrm{norm}}(\omega)$ of a laser pulse after travelling through an OMF calculated according to Eq. (2.14).

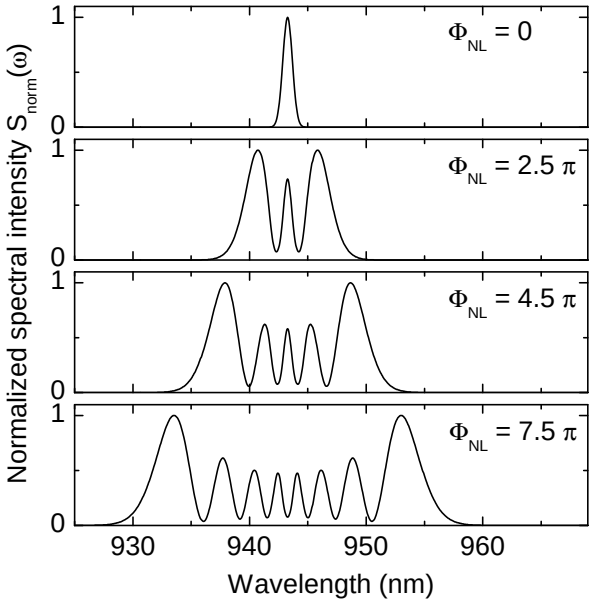

Figure 2.1: Calculated SPM-broadened spectrum for an OMF with a waist diameter of $d = 0.440$ µm, a waist length of $l = 5$ mm, and the nonlinear-index coefficient $n_2 = 3.2^{-16}$ cm^2/W (p. 40 in [38]). The laser pulse duration is 1.35 ps an the central wavelength is $\lambda = 943$ nm. The used average powers are, from top to bottom: 0 mW, 121 mW, 218 mW, and 363 mW. Similar simulations have been reported for example in [48].

Experimental setup

In our experiment we observed spectral broadening in OMF with the setup shown in Fig. 2.2. We use a Spectra-Physics Tsunami Ti:sapphire laser tunable from 840 nm to 1020 nm, which can operate in both continuous-wave (CW) and pulsed (1 ps pulse duration, 80 MHz repetition rate) mode. When the laser is operated in the pulsed mode the initial spectral width is fourier limited to ∼1 nm. The input fibre end is fixed to a positioning stage and the beam is coupled into the fibre using a microscope objective. The beam emitted from the fibre is collected by a lens. A small fraction of the beam is reflected at a glass plate and detected with a spectrometer (Avantes AvaSpec 3648-UA-25-AF). The light transmitted through the glass plate is monitored with a thermal power meter. To check the nonlinearities of the used optics we sent pulsed light through an untapered optical fibre instead an OMF and measured the resulting spectrum. Within the spectrometer resolution of 1.4 nm we could not see any spectral broadening from which we concluded that the nonlinearities of the optics can be neglected for our measurements.

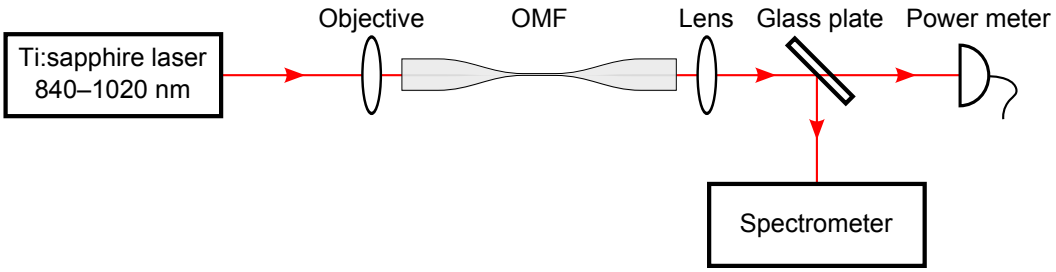

Figure 2.2: Experimental setup for measuring spectral broadening in OMF. The laser pulses are coupled into the OMF with a microscope objective and are collected after the OMF with a lens. A small fraction of the beam is reflected at a glass plate and detected with a spectrometer. The light transmitted through the glass plate is monitored with a thermal power meter.

Measurement

Laser pulses with an initial wavelength of 943 nm, a pulse duration of 1.35 ± 0.15 ps and an average power of 260 mW were sent through an OMF (diameter $d = 0.44$ µm, waist length $l = 5$ mm). After travelling through the OMF, the spectrum of the laser pulses is broadened symmetrically around the initial wavelength to a width of 25 nm and consists of eight peaks, see Fig. 2.3. The calculated SPM-broadened spectrum for the same fibre geometry and similar laser parameters is also plotted in Fig. 2.3 for comparison. The general shape of the calculated and measured spectrum with eight peaks and a spectral width of 25 nm coincide very well. In the calculations a 35 % higher power was needed to reproduce the spectral broadening from the measurement. Several reasons can be responsible for this deviation. First, the pulse peak power P_0 is not known very precisely. To calculate the peak intensity we have to know the fibre diameter, the pulse duration and the average power. However, the errors of the assumed fibre diameter, $d = (0.44 \pm 0.02)$ µm, and the pulse width, $\tau = (1.35 \pm 0.15)$ ps, are large. Moreover, the average power was measured after the fibre and due to losses in the up-taper, the actual average power in the microfibre waist might be higher. Another reason for the deviation could be SPM additionally occuring in the taper, which was not considered in the calculation. It is also noticable that the exact shape of the inner peaks does not meet the expectations. In the calculations the spectral intensity between the peaks reaches almost zero whereas in the measured spectrum the contrast is not very high. This could be attributed to the resolution of the spectrometer (1.4 nm) or additional linear and nonlinear effects. For example, in the optical fibre section

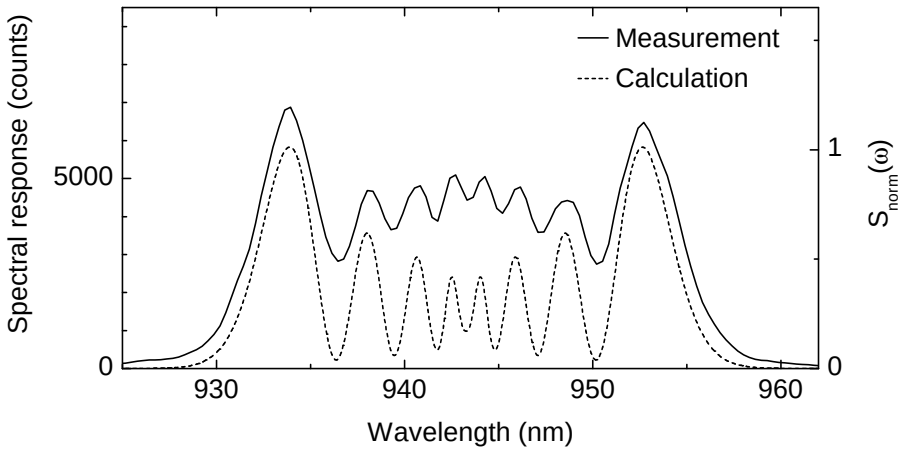

Figure 2.3: Solid line: Laser pulse spectrum measured after an OMF with a waist diameter of $d = 0.440$ µm and a waist length of $l = 5$ mm. The initial laser wavelength is 943 nm, the pulse duration 1.2–1.5 ps, the average power after the OMF 260 mW, and the spectral resolution 1.4 nm. Dotted line: Calculated SPM-broadened spectrum using the same OMF geometry and the following laser pulse parameters: initial wavelength 943 nm, pulse duration 1.35 ps, average power 350 mW. The nonlinear phase shift of the calculated spectrum is $\Phi_{\mathrm{NL}} = 7.24\ \pi$.

before the tapered part group velocity dispersion (GVD) can occur. This leads to a frequency chirp within the light pulse meaning that the instantaneous frequencies are not distributed homogenously over the pulse. In combination with SPM a symmetric, but smeared out spectral distribution is the consequence.

Experimentally, it is impossible to achieve the high symmetry of the broadened spectrum in Fig. 2.3 reproducible. Usually, the spectra have a more arbitrary shape and depend strongly on the actual light pulse. Two examples for typical broadened spectra are shown in Fig. 2.4. Asymmetric spectral broadening can originate for example from self-steepening [49,50] or stimulated Raman scattering [51]. However, from the results illustrated in Fig. 2.3 we can still conclude that SPM is very significant for the spectral broadening in OMF.

For the diameter measurement presented in the following sections the spectral broadening turns out to be a desirable side effect. However, since it is not the main interest of this work, I omit a more detailed discussion of additional nonlinear spectral broadening effects. An overview can be found in [38].

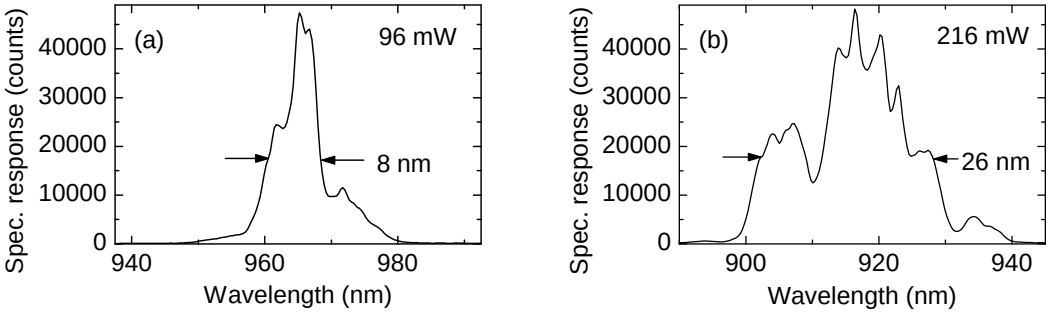

Figure 2.4: Spectra of pulsed light after travelling through an OMF ($d = 0.440$ µm, $l = 5$ mm). The pulse duration was 1.2–1.5 ps and the average power after the OMF 96 mW (a) and 216 mW (b).

2.2.2 Harmonic generation

The second nonlinear effect we observed in OMF is harmonic generation. As mentioned in Sec. 2.1, harmonic generation is a frequency-mixing process in which two, three, or n photons of the same frequency ω generate one new photon with the frequency 2ω, 3ω, or $n\omega$, respectively.

Modal phase matching for harmonic generation

For efficient harmonic generation, at each position along the microfibre waist the local generated harmonic wave has to be in phase with the harmonic waves generated in the section before. This is fulfilled if the phase velocities $v_{\mathrm{ph}} = c/n_{\mathrm{eff}}$ of the fundamental and harmonic waves are equal, where $n_{\mathrm{eff}} = \beta/k_0$ is the effective refractive index, and is known as the phase-matching condition. It can be written as

$$n_{\mathrm{eff,fundamental}} = n_{\mathrm{eff,harmonic}} \tag{2.15}$$

Due to material dispersion phase matching cannot be achieved for the same mode of the fundamental and the harmonic wavelength in an OMF. By making use of modal dispersion we can overcome this problem and phase match the $\mathrm{HE}_{11}(\omega)$ mode of the fundamental wavelength to higher modes of the harmonic wavelengths. Figure 2.5 illustrates the effective refractive index depending on the fibre diameter for the lowest-order modes of the IR pump light with $\lambda_\omega = 1000$ nm and the corresponding second-harmonic light with $\lambda_{2\omega} = 500$ nm and third-harmonic light with $\lambda_{3\omega} = 333$ nm. These plots are obtained similarly to Fig. 1.3a using $n_{\mathrm{eff}} = \beta/k_0$. At the intersections marked with black circles the phase-matching condition is fulfilled.

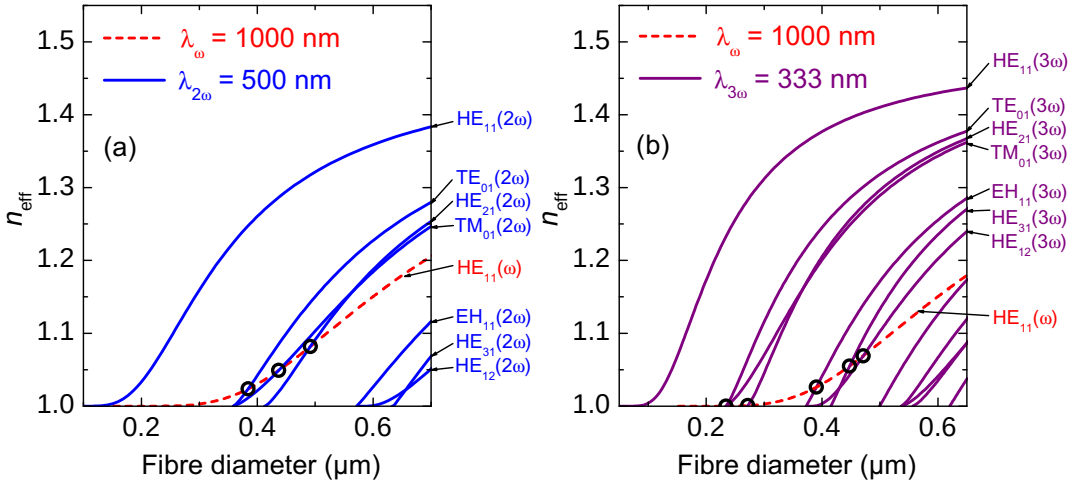

Figure 2.5: The effective refractive index depending on the fibre diameter for $\lambda_\omega = 1000$ nm and the wavelength of the second harmonic $\lambda_{2\omega} = 500$ nm (a) and third harmonic $\lambda_{2\omega} = 333$ nm (b). The lowest-order modes for all three wavelengths are shown. At the intersections marked with black circles the phase-matching condition is fulfilled.

Mode overlap

To get efficient energy transfer from the fundamental mode of the pump light $\mathrm{HE}_{11}(\omega)$ to the higher mode of the harmonic light a large nonlinear mode overlap is required. For the second harmonic exact values of the nonlinear mode overlap cannot be obtained since the origin of $\chi^{(2)}$ is not fully understood. Lægsgaard investigated in [45] the contributions from the electric quadrupole moments of the bulk and the contributions from the fibre surface to the nonlinear mode overlap. Lægsgaard further mentioned that the nonlinear overlap of the $\mathrm{HE}_{11}(\omega)$ and $\mathrm{TE}_{01}(2\omega)$ is zero, and therefore no SHG to this mode is expected. For THG the nonlinear mode overlap ρ_3 can be calculated according to [14]

$$\rho_3 = \iint_{A_{\mathrm{NL}}} (\mathbf{F}_1^* \cdot \mathbf{F}_3)\,(\mathbf{F}_1^* \cdot \mathbf{F}_1^*)\,dS \tag{2.16}$$

where A_{NL} is the cross section of the fibre and $\mathbf{F}_1$ and $\mathbf{F}_3$ are the normalized transverse electric modal fields of the fundamental wave and the third harmonic wave, respectively. The nonlinear mode overlap integral can be calculated numerically and depends on the fibre diameter and the wavelength of the pump light. For the three THG phase-matching points in Fig. 2.5b the nonlinear mode overlap was determined, see Tab. 2.1. The phase-matching points at fibre diameters below

$d = 0.3$ µm have been neglected since n_{eff} is very close to 1 for these modes. In this case the evanescent field is very large, i.e. the light propagates mainly outside the fibre, and small fibre diameter non-uniformities result in significant losses [52]. Therefore, these modes are not expected to be guided reasonably.

THG mode	Fibre diameter (µm)	Nonlinear mode overlap ρ_3
$EH_{11}(3\omega)$	0.390	0.01
$HE_{31}(3\omega)$	0.448	0.17
$HE_{12}(3\omega)$	0.471	0.79

Table 2.1: Calculated nonlinear mode overlap for THG at the three phase-matching points for $\lambda = 1000$ nm.

Measurement of harmonics

The experimental setup for the harmonic measurement is shown in Fig. 2.6. To measure SHG and THG at different wavelengths we use the tunable Ti:sapphire laser (840–1020 nm) in pulsed mode (1 ps pulse duration, 80 MHz repetition rate). The input fibre end is fixed to a positioning stage and the beam is coupled in using a microscope objective. The typical average power in the sample is 120 mW (1.5 nJ pulse energy). The beam emitted from the fibre is collected by a lens. A dichroic mirror reflects IR and transmits the second harmonic. The IR power is monitored by a thermal power meter. The light passing the dichroic mirror (∼100 nW) is filtered from residual IR light and the second-harmonic light is measured by the spectrometer (Avantes AvaSpec 3648-UA-25-AF). Despite higher efficiency of THG in comparison with SHG in silica, we do not observe a significant amount of THG light at the end of the fibre due to the high UV-absorption in the Ge-doped core of our samples. Therefore we usually measure the third-harmonic light by positioning an ultraviolet-pass filter and the spectrometer directly above the fibre waist and

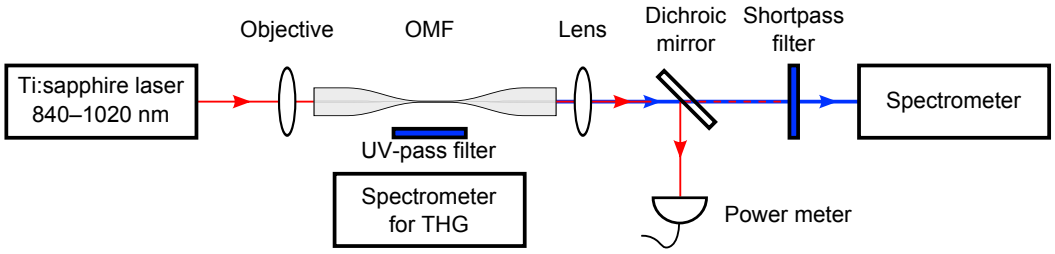

Figure 2.6: Experimental setup for SHG and THG measurement.

detecting scattered UV light. Alternatively, by splicing a pure silica 50 µm core fibre to our fibre sample at the up-taper, we were also able to collect the third-harmonic UV light at the end of the fibre.

The measured harmonic spectra at a fixed IR wavelength are illustrated in Fig. 2.7. As described in Sec. 2.2.1 the IR light is spectrally broadened. The wavelength of the harmonic spectra are as expected at one half (SHG) and one third (THG) of the IR spectrum wavelength. The conversion efficiency of SHG and THG with 120 mW of pulsed light is typically on the order of 10^{-6} and 10^{-5}, respectively.

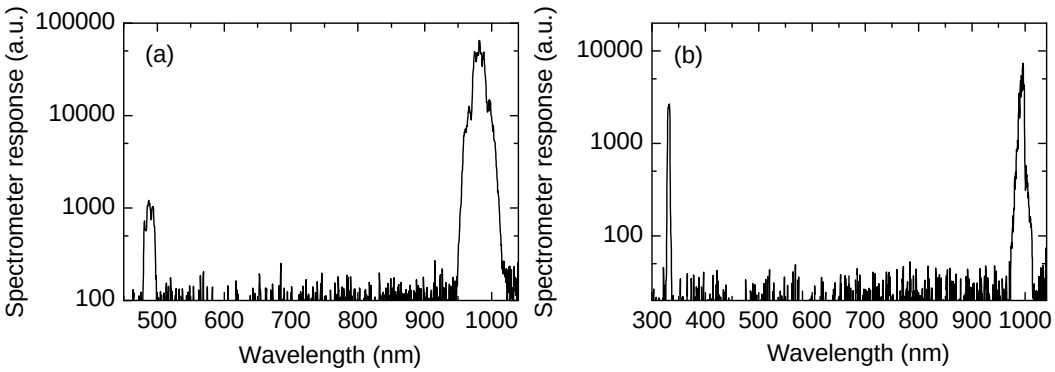

Figure 2.7: Harmonic generation at a fixed laser wavelength. The spectrally broadened IR light is converted to the second (a) and third (b) harmonic. In this measurement we used IR filters with low optical density to detect also the IR light. Due to different coupling efficiencies of the IR and the harmonic light to the spectrometer, the peak heights are not up to scale.

2.3 Concept of microfibre diameter measurement

Figure 2.8a shows the effective refractive index for the fundamental and the second-harmonic light. The three intersections at different fibre diameters are the phase matching points. If the wavelength is changed, the n_{eff} curves shift, and thus phase matching occurs at a different fibre diameter, see Fig. 2.8b. This means that for each mode there is a one to one relation between the fibre diameter and the phase-matching wavelength (Fig. 2.8c). The phase-matching curves for THG can be obtained in a similar way and are shown in Sec. 2.5.2, Fig 2.12.

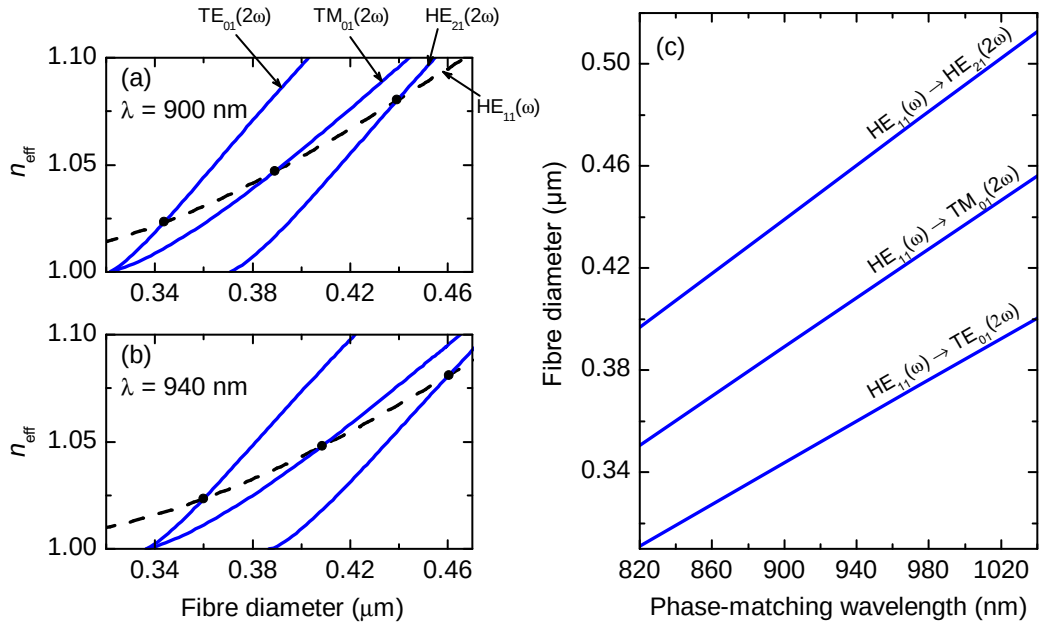

Figure 2.8: (a, b) Effective refractive index of the fundamental wave (dashed line) and the second harmonic wave (solid lines). For each wavelength the phase-matching condition is fulfilled at the three intersections. (c) Dependence of the fibre diameter on the phase-matching wavelength for the three modes.

2.4 Measurement of the harmonic spectral response

The OMF samples were pulled from the Fibercore SM800 fibre which has a Ge-doped core ($d_{\text{core}} = 4$ µm) and a pure silica cladding ($d_{\text{cladding}} = 125$ µm). Each taper consists of three sequential conical sections with slopes of 3 mrad, 2 mrad, and 3 mrad, respectively, and typically has a total length of 3.5 cm. The fibre waist has a length of 4 mm. The results in this chapter are obtained from samples with diameters ranging from 0.32 µm to 0.51 µm. The samples are labelled with capital letters A–G.

The pulsed laser and the strong light confinement provide a high peak intensity in the waist. This high peak intensity leads to SPM-dominated nonlinear broadening of the IR light. The laser pulse with 1 ps pulse duration and an initial spectral width of ∼1 nm is broadened by 10–20 nm. The IR transmission of the tapered part of the fibre exceeds 95 %.

For each broadened spectrum, the resulting harmonic light is measured using the spectrometer, see Fig. 2.7a for SHG and Fig. 2.7b for THG. To determine the

harmonic spectral response of the fibre, we scan the whole tuning range of our laser in between 10 and 20 steps and build the envelope of all individual spectra. The resulting spectral response for SHG is illustrated in Fig. 2.9a and for THG in Fig. 2.9b.

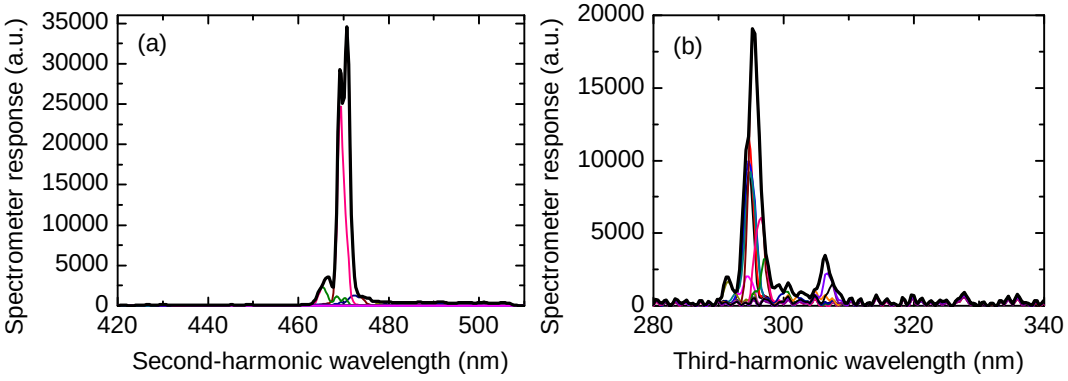

Figure 2.9: Full second-harmonic (a) and third-harmonic (b) spectral response of sample A: envelope (thick line) of individual SHG spectra taken at different laser wavelengths (thin lines).

2.5 Analysis of the harmonic spectral response

2.5.1 Interpretation of measured harmonic spectrum shape

As explained in Sec. 2.3, the wavelength of the generated harmonic light is directly connected to the fibre diameter via the phase-matching condition. Thus, the second- and third-harmonic spectral response shown in Fig. 2.9 can be analysed with respect to the fibre diameter. To connect the diameter occurrence with the expected harmonic spectral response, i.e. the conversion efficiency vs. the wavelength, one has to know the coherence length l_{coh} (the length over which the phase matching is maintained). For a perfectly uniform waist shape ($l_{\mathrm{coh}} \gg l_{\mathrm{waist}}$), the conversion efficiency depends quadratically on the waist length, $\eta \sim l_{\mathrm{waist}}^2$, due to coherent addition of the field amplitudes, see page 108 in [37]. In the realistic case of a non-uniform waist ($l_{\mathrm{coh}} \ll l_{\mathrm{waist}}$) the dependence will be approximately linear, $\eta \sim l_{\mathrm{waist}}$, due to intensity build-up [53].

In Fig. 2.10 the second-harmonic spectral response of sample A is again illustrated. The second-harmonic tail at long wavelengths can be attributed to phase matching occurring within the taper. Due to the short coherence length in the taper the SHG response is weak. The main peak, originating from the fibre waist,

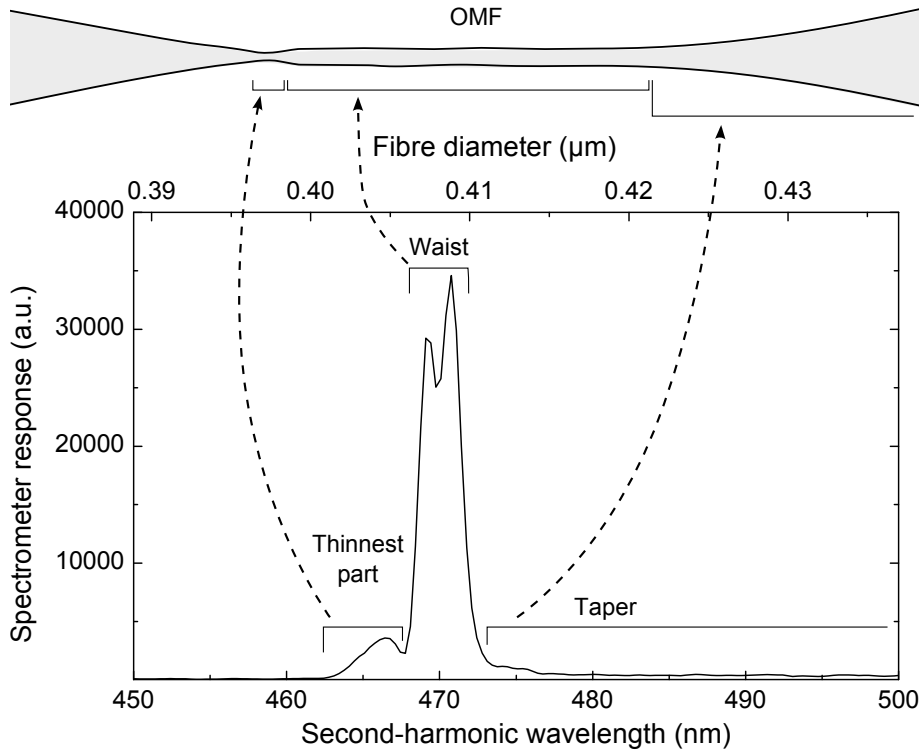

Figure 2.10: Second-harmonic spectral response of sample A. On the bottom axis the second-harmonic wavelength is plotted whereas the top axis illustrates the corresponding fibre diameter calculated from the phase-matching condition $\mathrm{HE}_{11}(\omega) \rightarrow \mathrm{TM}_{01}(2\omega)$.

is at $\lambda_{\mathrm{SHG}} = 470$ nm ($\lambda_{\mathrm{fundamental}} = 940$ nm) and corresponds to phase matching of $\mathrm{HE}_{11}(\omega)$ to $\mathrm{TM}_{01}(2\omega)$ at a fibre diameter of $d = 0.408$ µm. The leftmost minor peak corresponds to a short segment being thinner than the rest of the waist. Since there are no regions of smaller diameter in the fibre, there is no possibility of phase matching at shorter wavelengths. This explains the distinct cut-off on the left side of the spectrum.

The high peak intensity of the picosecond laser pulse could influence the phase-matching condition due to SPM or XPM effects [15]. Thus, we have cross-checked the second-harmonic spectral response of the fibre with a CW measurement using the same average power. Since the intensity of the CW light is much lower than the peak intensity of the pulsed light, the SHG in CW mode is much weaker than in the pulsed mode. Therefore we detect the second-harmonic signal with a photomultiplier tube (PMT). To obtain the spectral response, the laser wavelength is tuned in

steps of about 0.4 nm and measured with an optical spectrum analyser (OSA, Ando AQ-6315A). Figure 2.11 shows the results for the CW and the pulsed measurements of sample B. One can see that the shape of both spectra coincide well, which means that for our intensities nonlinear effects like SPM or XPM seem to have no measurable influence on the phase-matching condition. The double peak structure of the spectrum at 485.5 nm ($d = 0.4766$ µm) and 488.0 nm ($d = 0.4792$ µm) can be explained by this particular sample having two dominating waist diameters. The conversion efficiency of SHG with 120 mW of CW light is typically on the order of 10^{-8}.

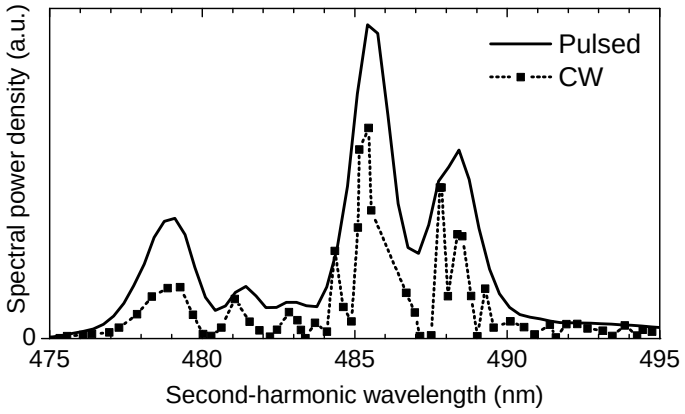

Figure 2.11: Second-harmonic spectral response of sample B measured with CW light (dotted line; the solid squares represent the measured points) in comparison to the measurement with pulsed light (solid line). The heights of the two signals are not up to scale.

2.5.2 Determination of the microfibre waist diameter

Figure 2.12 illustrates how to derive the waist diameter from the peak position of SHG and THG. The full second- and third-harmonic response of sample C is shown in Fig. 2.12a and the phase-matching condition for SHG and THG is shown in Fig. 2.12b. The fibre waist diameter is determined from the wavelengths of the four peaks listed in Tab. 2.2.

The average fibre waist diameter is 0.4257 µm. The diameter errors in Tab. 2.2 are obtained from the spectrometer resolution of ±0.7 nm and the spectrometer calibration error of ±0.3 nm using the phase-matching functions shown in Fig. 2.12b. Since these individual diameter errors are smaller than the variation of the four diameter values determined from the harmonic peak wavelengths, we assume some

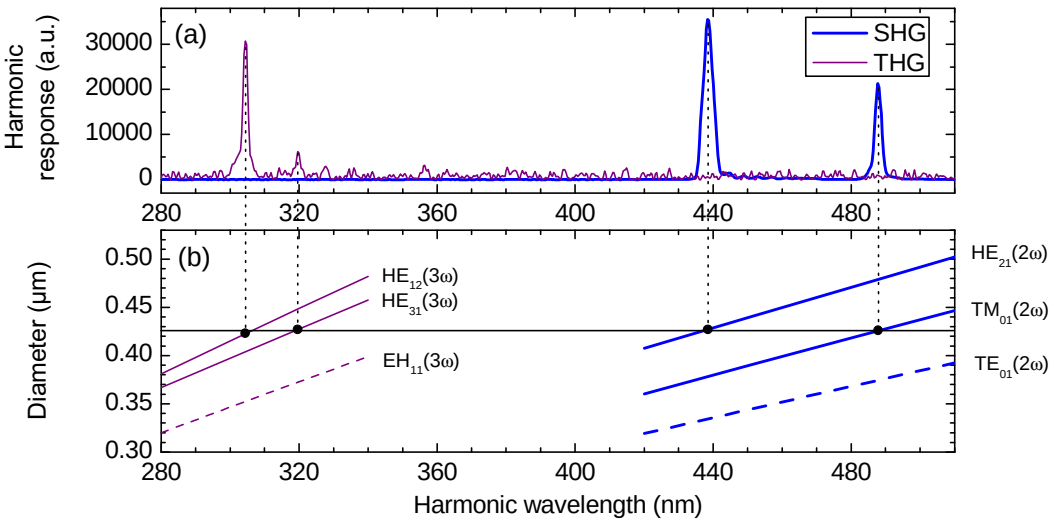

Figure 2.12: (a) The spectral response of sample C for SHG (thick line) and THG (thin line) plotted vs. the harmonic wavelength. The spectrometer response of the THG measurement is scaled up for visibility. The four peaks correspond to phase matching to the following modes (from left to right): $HE_{21}(2\omega)$, $HE_{12}(3\omega)$, $HE_{31}(3\omega)$, $TM_{01}(2\omega)$. (b) Wavelength-dependent phase-matching diameter. Thick lines: SHG, thin lines: THG, dashed lines: modes not observed. The horizontal line indicates the diameter of the investigated sample determined by this method.

unknown underlying systematic error. We therefore estimate the diameter error as half of the maximum difference between the diameter values. From Tab. 2.2 we receive for sample C the error of $\pm 2.0 \times 10^{-3}$ µm. This value is the largest among all samples A–F. We take a conservative approach and use this value for all our samples.

We have not observed the two modes $TE_{01}(2\omega)$ and $EH_{11}(3\omega)$ in any of our samples falling in the range between 0.32 and 0.4 µm. In Sec. 2.2.2 was shown that the nonlinear mode overlap of the fundamental mode $HE_{11}(\omega)$ to these two modes is zero ($TE_{01}(2\omega)$) and very low ($EH_{11}(3\omega)$) making harmonic generation impossible or very inefficient. The nonlinear mode overlap for the two THG modes observed with sample C are $\rho_3(HE_{12}) = 0.88$ and $\rho_3(HE_{31}) = 0.19$. Indeed, in Fig. 2.12 one can see that the left THG peak corresponding to phase-matching to the $HE_{12}(3\omega)$ is approximately a factor 5 higher than the right THG peak corresponding to phase-matching to the $HE_{31}(3\omega)$ mode.

Wavelength (nm)	Phase-matching mode	Diameter (µm)	Diameter error (µm)
304.5	$HE_{12}(3\omega)$	0.423	$\pm 1.3 \times 10^{-3}$
319.5	$HE_{31}(3\omega)$	0.427	$\pm 1.1 \times 10^{-3}$
438.5	$HE_{21}(2\omega)$	0.427	$\pm 0.8 \times 10^{-3}$
488.0	$TM_{01}(2\omega)$	0.426	$\pm 0.7 \times 10^{-3}$

Table 2.2: Phase-matching wavelengths and corresponding waist diameters of sample C.

2.6 Verification using scanning electron microscope imaging

To verify our method, we check the diameter of our samples using a Zeiss SUPRA 55 field emission scanning electron microscope (SEM). The details of this measurement can be found in [54]. Before inserting the samples into the SEM, they are attached to a gold-coated silicon wafer and additionally coated by sputtering a 2 nm thick layer of gold using a Bal-Tec MED 020 machine. The coating minimizes distortion of the electric field in the SEM due to electrostatic charging of the non-conductive silica. We use electron acceleration voltages of 15 and 20 kV and calibrate the obtained SEM images with a calibration target (Plano S1995A). To find the edge of the fibre, we use the highest contrast model [55]. More precise models [56] can be used, but they require the exact knowledge of the electron-sample interaction, which depends on the material, geometry and dimensions of the samples. While the application of SEM is straightforward for relative diameter measurements (imaging the fibre), it is challenging to perform absolute measurements of the submicrometre diameter with an accuracy below 2 %. For a fibre of 0.4 µm in diameter, this corresponds to an error of $< 8 \times 10^{-3}$ µm.

Figure 2.13a shows the diameter profile of sample A measured with the SEM. The fibre waist typically exhibits a short thinner section on one (or both) sides, followed by the taper region with increasing thickness. As seen in Fig. 2.10, the large variation of the diameter in the tapers will therefore produce a weak broadband harmonic generation response, while the relatively uniform and long waist will cause a narrow peak. It is worthwhile to mention that the leftmost minor peak seen on the spectral curve in Fig. 2.10 corresponds to the short segment (cf. position 3.5 to 4 mm in Fig. 2.13) being thinner than the rest of the waist. Moreover, the splitting of the main peak in Fig. 2.10b corresponds to the two larger fibre diameters seen in the SEM data (Fig. 2.13b): slightly thinner waist from 0.5 to 2 mm and a thicker

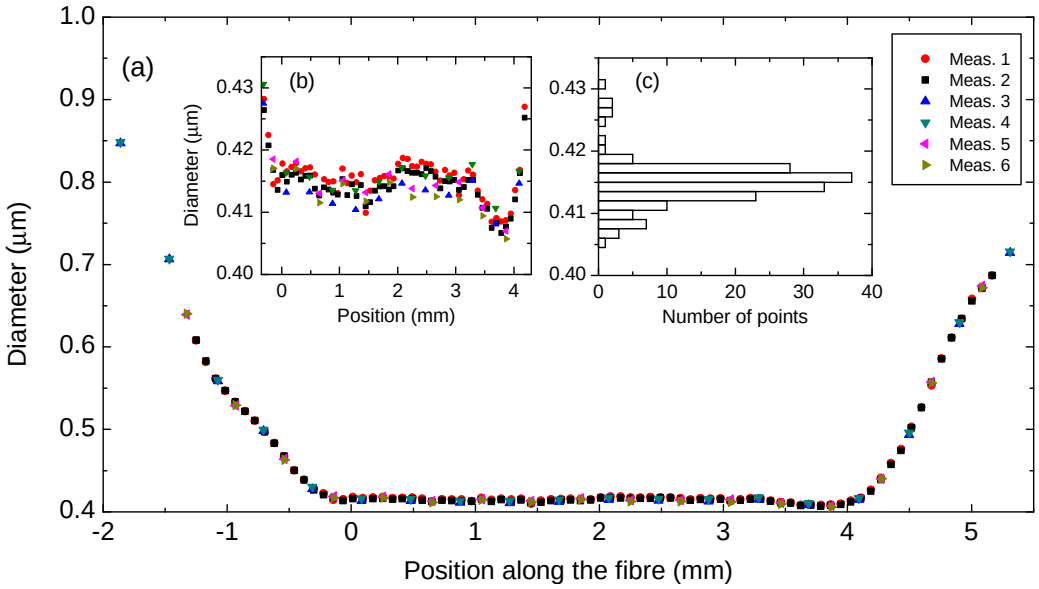

Figure 2.13: (a) Diameter profile of an OMF (sample A) obtained by SEM measurements of different beam energies and scan speeds, designated Meas. 1 to Meas. 6. The position of zero along the fibre is arbitrary. (b) Vertically enlarged picture of the waist. A short thinner region at the right end of the waist can be seen. All the individual points are measured with an accuracy of $< 7 \times 10^{-3}$ µm. (c) Diameter histogram.

Source	Value (µm)	Comment
Finding fibre edge on the image	$\pm 5 \times 10^{-3}$	Systematic uncertainty of our image analysis method
SEM calibration for each beam energy, beam current, scan speed	$\pm 4 \times 10^{-3}$	Error of the calibration target (Plano S1995A), error of processing the target images
Diameter error due to gold coating thickness variation	$\pm 2 \times 10^{-3}$	According to Bal-Tec, manufacturer of our sputtering machine MED 020
Total:	$\pm 7 \times 10^{-3}$	

Table 2.3: SEM error contributions.

part between 2 and 3 mm. The number of SEM images taken is not large enough to allow us to resolve the two peaks in the histogram, Fig. 2.13c.

Further on, the error of the SEM measurement is calculated. Each SEM image shows a section of the fibre 1 µm in length, see Fig. 2.15a. The fibre diameter is

determined by measuring the distance between the fibre edges on the image. Various contributions to the total diameter error are listed in Tab. 2.3. The variation of these various errors along the waist is negligible, therefore we use the same error bar for all measurement positions along the waist.

The comparison of the fibre diameter obtained by harmonic generation and SEM measurements is shown in Fig. 2.14 and Tab. 2.4. The procedure to derive the diameter value and the error for our optical method was described in Sec. 2.5.2. To

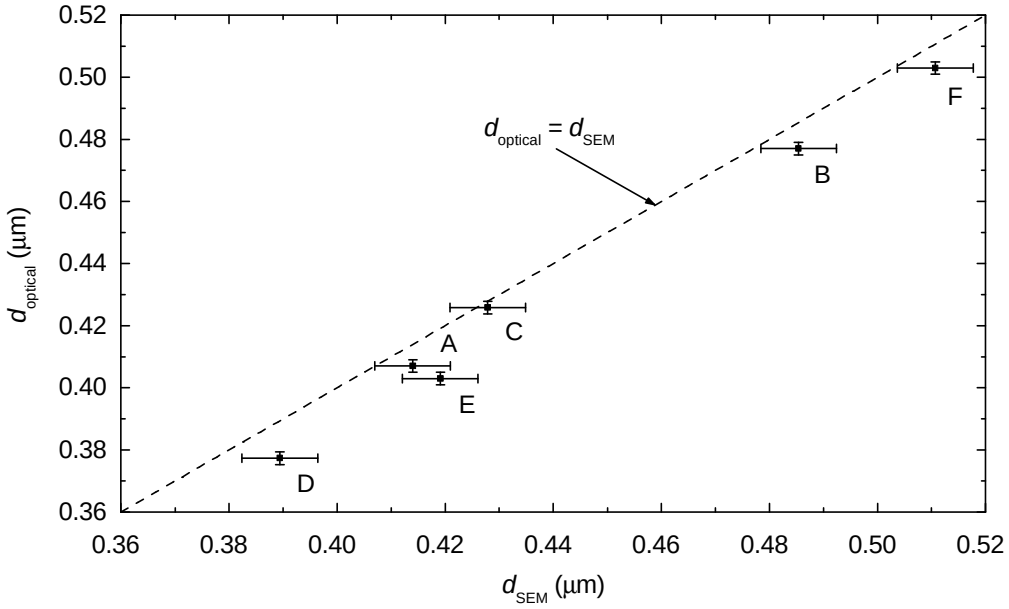

Figure 2.14: The fibre diameter measured by harmonic generation (d_{optical}) vs. the diameter as measured by SEM (d_{SEM}) for samples A–F.

Sample	Fibre diameter (µm)	
	Optical method (±0.002 µm)	SEM (±0.007 µm)
A	0.407	0.414
B	0.477	0.485
C	0.426	0.428
D	0.377	0.389
E	0.403	0.419
F	0.503	0.511

Table 2.4: Fibre waist diameters obtained by optical method and SEM.

get the diameter value of the SEM measurement, the highest peak of the diameter histogram is identified, as shown in Fig. 2.13c for sample A. The overall sample diameter error of $\pm 7 \times 10^{-3}$ µm is denoted by the horizontal error bars in Fig. 2.14.

2.7 Optical damage

During our measurements, we have observed in some samples (not included in Fig. 2.14) a change in the harmonic generation properties over time. After exposing the fibres to pulsed light for several minutes, the strong SHG and THG peaks originating from the waist disappeared. The SEM investigation of these samples showed that some of them suffered physical modification of the surface: a series of "bumps" are clearly visible on the tapered fibre, see Fig. 2.15.

While the origin of these bumps is not clear, the result obtained with one particular sample allows us to suggest a cause. This sample G has a waist ∼0.32 µm in diameter (measured with SEM), which is too thin to produce harmonic generation with the wavelength range of our laser (840–1020 nm). However, this wavelength range provides for phase matching to the second and third harmonic in the diameter range of 0.36–0.5 µm (see Fig. 2.12b). The taper of sample G covers this whole range. In our setup, we have observed a low second- and third-harmonic signal at all wavelengths of our laser. The SEM images reveal the bumps on the taper just in the diameter range where the harmonics could be generated (Fig. 2.15b and c). At the same time, no bumps are seen on the thicker section of the taper (Fig. 2.15a) and on the waist (Fig. 2.15d), for which phase matching is not achievable. We can thus conclude that the appearance of bumps is related to the generation of harmonic light. In our case, the third harmonic falls into the UV range, which can indeed damage optical fibres [57]. The fibre used in this experiment (Fibercore SM800) is not specified for UV operation.

Therefore, strong harmonic generation can induce irreversible changes in the fibre, including a change of the phase-matching wavelength, which could be problematic for an accurate measurement of the fibre diameter. This can be avoided by using CW light to measure the harmonic spectral response. No peak shift has been observed in our samples while using CW for even longer times.

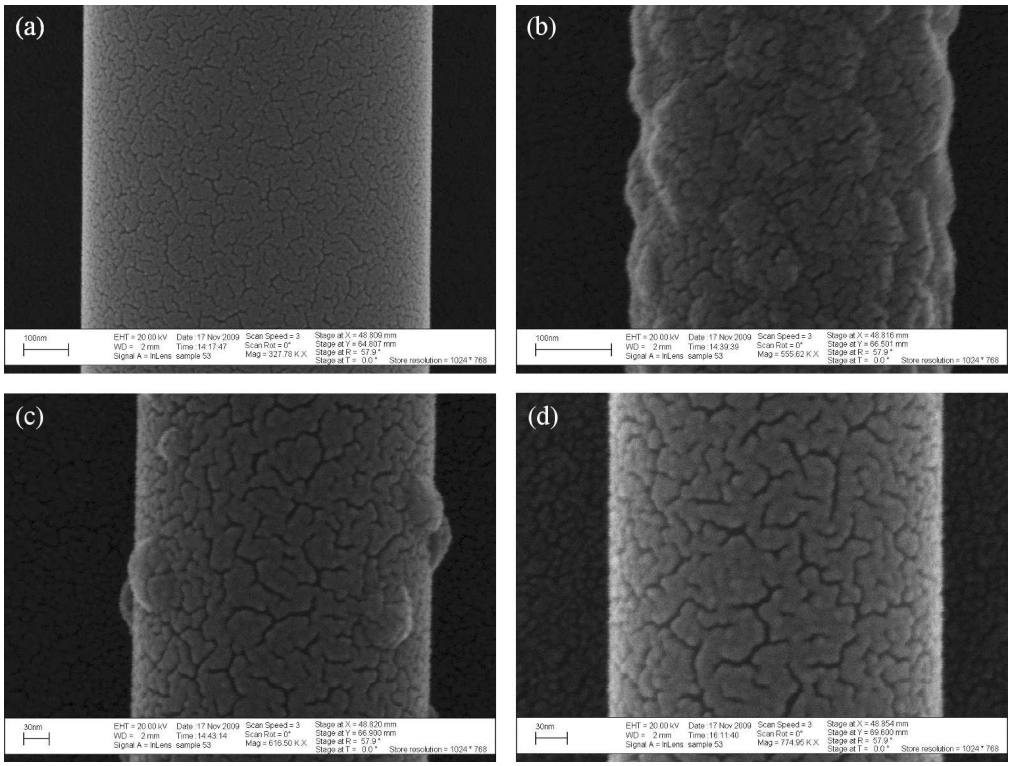

Figure 2.15: SEM images of the damaged sample G. No phase matching and therefore no harmonic light could be achieved within our laser wavelength range for (a) a very thick section of the taper ($d = 0.790$ µm) and (d) for the waist ($d = 0.319$ µm). Images (b) and (c) show the taper sections where harmonic light was generated ($d = 0.430$ µm and $d = 0.355$ µm, respectively). The fissures on all images are due to the gold coating.

2.8 Conclusion

Several other methods to measure the diameter of an OMF were also proposed. One method is based on illuminating the fibre from the side and then analysing the scattered light. An accuracy of 50 nm for a fibre with a diameter of around 1.32 µm was reported [58]. SEM measurements with an accuracy of 3 % were demonstrated [59], but the measurements are time consuming and destructive. A method for measuring the uniformity of OMF with high resolution was also proposed [60, 61]. However, it gives no information about the absolute diameter, so additional measurements are still required.

In this chapter, I presented an optical method to non-destructively measure the

diameter of an OMF with an accuracy of < 2 % (limited by the SEM used for verification). To achieve harmonic generation at the phase-matching wavelength, a tunable laser can be used in both pulsed and CW modes. The accessible fibre diameter range is determined by the laser tuning range. Taking into account the transparency window of silica as the limit for light propagation in fibres, one can theoretically measure fibres with diameters down to 0.19 µm with a fundamental wavelength of 500 nm, and fibres with diameters up to 1 µm using fundamental wavelengths up to 2000 nm. Another option to extend the range of accessible diameters is to achieve harmonic generation to another set of higher modes, for which phase matching occurs at different fibre diameters. The straightforward experimental setup and fast measurement procedure makes this technique easily applicable.

Chapter 3

Switching photochromic molecules adsorbed to optical microfibres

Molecules changing their absorption spectrum under exposure to electromagnetic radiation are called photochromic molecules. This characteristic feature often comes along with a change in the physical and chemical properties and therefore provides many opportunities for research and applications. In this chapter, I give a brief overview about photochromic processes and the experimental basics needed for light-induced switching of photochromic molecules adsorbed to OMF.

3.1 Photochromism

Photochromism is defined as "a reversible change of a single chemical species between two states having distinguishable different absorption spectra, such change being induced in at least one direction by the action of electromagnetic radiation" [62]. This definition is schematically illustrated in Fig. 3.1 with the absorption spectra of the two chemical forms, labelled A and B. In one direction (A to B) there is a light-induced transformation changing the chemical structure and the absorption spectrum of the molecules. According to the definition a photochromic process is reversible and therefore the backtransformation from B to A is possible.

3.1.1 General characteristics of photochromic systems

In typical photochromic systems only one molecule form exhibits a strong absorption band in the visible wavelength range and is therefore called the coloured form, the other form is called transparent, and both forms absorb light in the UV wavelength range. In Fig. 3.1 the coloured molecules would correspond to form B and the transparent molecules to form A. Switching from the transparent to the coloured form (photocolouration) occurs by illumination with UV light, the backswitching

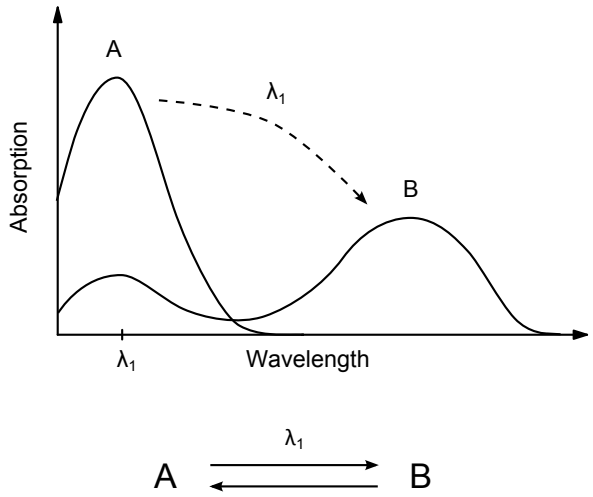

Figure 3.1: Schematic sketch of the definition of photochromism. The absorption spectra of the two molecule forms A and B are illustrated. The bottom graph shows the corresponding reaction diagram.

from coloured to transparent by illumination with visible light (photobleaching) or by thermal relaxation.

The temporal behaviour of an ideal photochromic system under illumination is depicted in Fig. 3.2. At least one of the two molecule forms is thermally stable, usually the transparent form, and without illumination all molecules tend to be in this form. During the exposure to UV light, the fraction of coloured molecules $N_{\mathrm{col}}/N_{\mathrm{tot}} = N_{\mathrm{col}}/(N_{\mathrm{col}} + N_{\mathrm{tr}})$ reaches a limiting maximum value, where N_{col} and N_{tr} are the numbers of coloured and transparent molecules, respectively, and N_{tot} is the total number of molecules. This indicates that the molecules distribution reaches a dynamic equilibrium of UV photocolouration and thermal relaxation, the so-called photostationary state. The fraction of coloured molecules $N_{\mathrm{col}}/N_{\mathrm{tot}}$ in the photostationary state depends on the rates of the two competing switching processes. After the UV exposure has stopped, the molecules return to the transparent form by thermal relaxation or by illumination with visible light. The switching of a photochromic system to a well-defined state with subsequent backswitching to the initial state is called a "cycle".

Meaningful parameters are required to quantify the characteristic properties of a photochromic system. The most important quantities are:

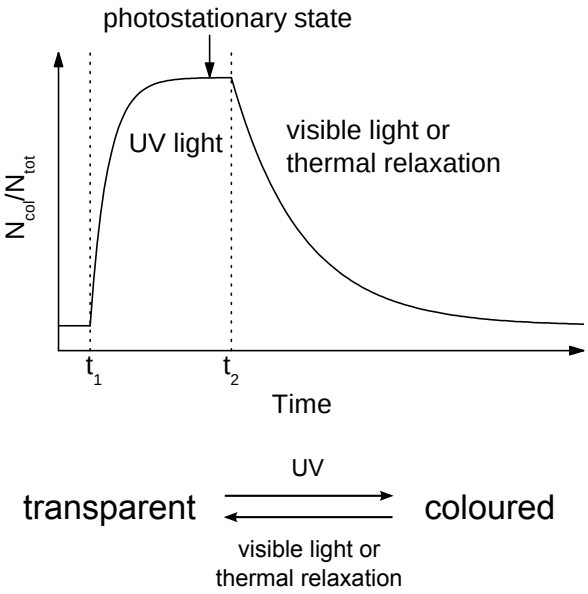

Figure 3.2: The change in the fraction of coloured molecules $N_{\mathrm{col}}/N_{\mathrm{tot}}$. At the time t_1 the illumination with UV light is started and the molecules switch to the coloured form. After the photostationary state is reached, at the time t_2, the illumination is stopped and the molecules return to the transparent form either by thermal relaxation or by illumination with visible light. The bottom graph shows the corresponding reaction diagram.

- **Absorbance spectrum**
  The absorbance A at the wavelength λ is defined as

$$A(\lambda) = -\log_{10} \frac{P_{\mathrm{sig}}(\lambda)}{P_{\mathrm{ref}}(\lambda)} \tag{3.1}$$

  where P_{sig} and P_{ref} are measured signal and reference powers transmitted through a sample in the presence and absence of coloured molecules, respectively. The absorbance is widely used in chemistry because it is proportional to the length of the sample and the molar concentration of the absorbing species (Beer-Lambert's law [63]).

- **Thermal relaxation rate**
  Without illumination photochromic molecules tend to be in a state of balance, the so-called thermodynamic equilibrium. The kinetic process leading to this

equilibrium is thermal relaxation and can be described by the rate equations

$$\frac{\mathrm{d}N_{\mathrm{col}}}{\mathrm{d}t} = -k_{\mathrm{thermal,col}} \cdot N_{\mathrm{col}} + k_{\mathrm{thermal,tr}} \cdot N_{\mathrm{tr}} \tag{3.2}$$

$$\frac{\mathrm{d}N_{\mathrm{tr}}}{\mathrm{d}t} = +k_{\mathrm{thermal,col}} \cdot N_{\mathrm{col}} - k_{\mathrm{thermal,tr}} \cdot N_{\mathrm{tr}} \tag{3.3}$$

where $k_{\mathrm{thermal,col}}$ and $k_{\mathrm{thermal,tr}}$ are the relaxation rates of the molecules in the coloured and transparent form, respectively.

- **Quantum yield**
  For photochemical reactions the probability to induce a process is important, which is characterized by the quantum yield Φ. The quantum yield of a photochromic process is defined in [62] as

$$\Phi_{\mathrm{switch}} = \frac{\Delta N_{\mathrm{switch}}}{J_{\mathrm{abs}}} \tag{3.4}$$

  where $\Delta N_{\mathrm{switch}}$ is the number of switched molecules and J_{abs} is the number of absorbed photons. Besides photoswitching, the absorption of photons can also result in chemical degradation. This means that destructive side reactions can occur leading to non-switchable photoproducts [64]. Analogue to Eq. (3.4), the quantum yield of the destructive reactions is given by

$$\Phi_{\mathrm{destr}} = \frac{\Delta N_{\mathrm{destr}}}{J_{\mathrm{abs}}} \tag{3.5}$$

  where $\Delta N_{\mathrm{destr}}$ is the number of destroyed molecules. Note that I use the term "photobleaching" for the photo-induced switching process from the coloured to the transparent form, and not for the photochemical destruction of molecules.

- **Cyclability**
  The chemical degradation reduces the performance of a photochromic system. A parameter to quantify how often a system with photochromic molecules can be switched is the cyclability Z_{50}. It is defined as the number of cycles to reduce the initial absorbance at a specific wavelength by 50 % [65].

3.1.2 Classes of photochromic reactions

Photochromic reactions are classified with respect to their switching mechanism. Besides dissociative photochromic reactions, occurring for example in triarylmethanes in solution, the switching mechanisms base on intramolecular chemical reactions changing the molecular structure while keeping the atomic composition of the molecule (photoisomerization). The change in the molecular structure occurs either by bond rotation, skeletal rearrangement or atom- or group-transfer [66]. An example for atom-transfer reactions is the relocation of a hydrogen atom or a proton, which is known as tautomerism. In Fig. 3.3 the cis-trans isomerization of azobenzene is shown. The right functional group (benzene ring) is rotated around the reference plane determined by the azo group, that means the two doubly-bound nitrogen atoms in the centre. In this context, "trans" and "cis" means that the functional groups are on the opposite and on the same side of the reference plane, respectively.

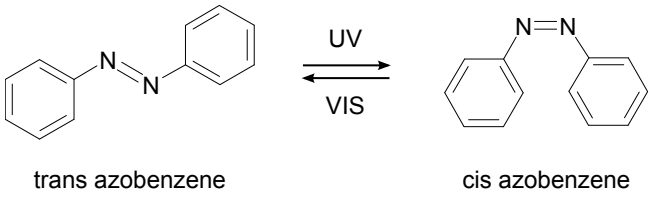

Figure 3.3: The process of cis-trans photoisomerization. The trans and cis azobenzene is switchable with UV and visible light, respectively.

The switching mechanisms of the molecules used in this work are pericyclic* ring-opening and ring-closing reactions, illustrated in Fig. 3.4 by means of the molecule stilbene from the class of the diarylethenes. The molecule structure rearranges in such a way that the bond between the two centre carbon atoms is either open

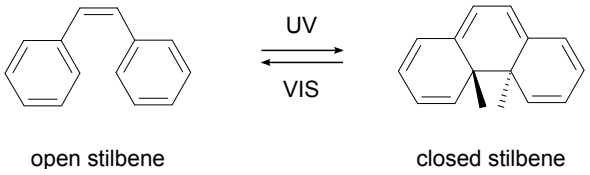

Figure 3.4: Pericyclic ring-opening and ring-closing reaction of stilbene induced by UV and visible light.

*Pericyclic reaction: A chemical reaction in which concerted reorganization of bonding takes place throughout a cyclic array of continuously bonded atoms [66].

(left) or closed (right). Diarylethenes are very compact and the switching reactions induce very little changes in the molecule shape and the polarity.

In pericyclic reactions involving heterolytic bond cleavage – a process occurring in spiropyranes – a covalent bond is broken producing two oppositely charged fragments [66]. In the case of spiropyranes a carbon-oxygen bond is broken, see Fig. 3.5. This reaction is non-dissociative meaning that the two fragments are still connected by other chemical bonds. The open-ring/coloured form of spiropyranes is called merocyanine.

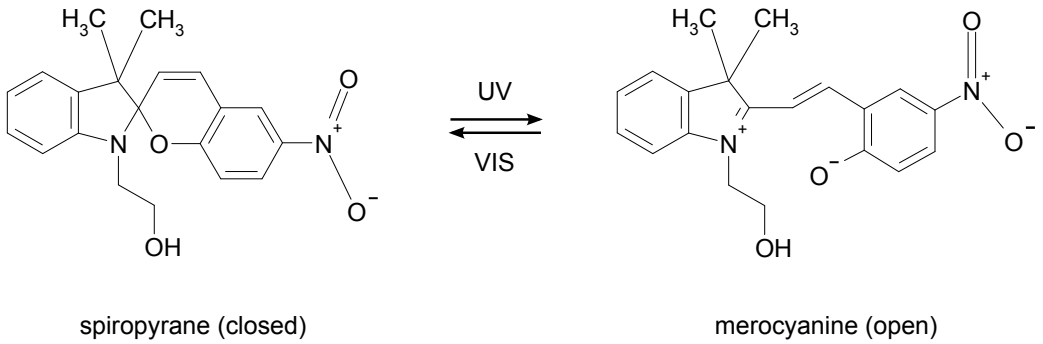

Figure 3.5: The process of heterolytic bond cleavage illustrated with the spiropyrane (spiroOH) used in the measurements. The molecular structure is shown for the closed-ring/transparent form (left) and the open-ring/coloured form (right).

3.1.3 Photochromic molecules used here

The photochromic molecules used in this work were chosen according to the criteria:

- Chemically stable at ambient conditions, especially in oxygen-containing atmosphere.
- Switchable not only in solution but also in the "dry" state on a silica surface.
- Switching by visible and near-UV light which can be guided by the OMF.

SpiroOH

In most experiments we used the commercially available fluorescent spiropyrane *1-(2-Hydroxyethyl)-3,3-dimethylindolino-6'-nitrobenzopyrylospiran* which I will call "spiroOH". Spiropyranes belong to the oldest and most studied photochromic molecule classes. The closed-ring form of a spiropyrane is transparent in the visible

wavelength range and the open-ring form is coloured. The molecular structure of both spiroOH forms is shown in Fig. 3.5 and the absorbance spectra in Fig. 3.6. The polarity of spiroOH is high due to the charged N^+O^--group on the right and the polar OH-group on the bottom. The open form provides additional polarity because of the charged open-ring section. In solution, the coloured form switches thermally back to the transparent form, whereas both forms of spiroOH in a silica matrix are thermally stable at room temperature [20]. To deposit the molecules on the OMF (see Sec. 3.2.1) a solution of 10 mg spiroOH in 50 ml toluene was prepared.

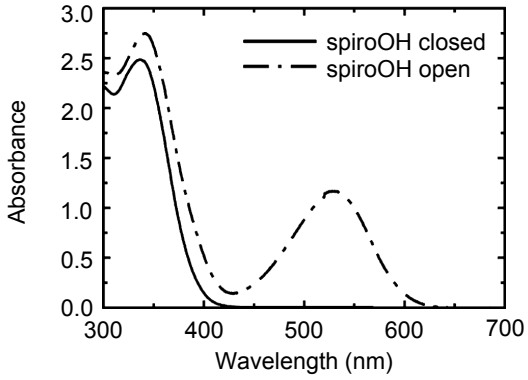

Figure 3.6: Absorbance spectra of spiroOH dissolved in methanol obtained with a UV–Vis spectrometer (no OMF used). The spectra are taken from [67].

XTPA

The second molecule I used is the diarylethene "XTPA", synthesized and provided by the group of Prof. Meerholz from the Institut für Physikalische Chemie, Universität Köln. In contrast to the spiropyranes, the closed-ring form of diarylethenes is coloured whereas the open-ring form is transparent. Figure 3.7 illustrates the molecular structure of XTPA (a) and the absorbance spectrum obtained with an UV-Vis spectrometer (b). XTPA provides small polarity and little shape changes due to switching. It is thermally stable up to 80 °C and the quantum efficiencies of the closing and opening processes are approximately 60 % and 0.1 % [68], respectively. For deposition a solution of 1.5 mg XTPA in 4 ml heptane was diluted by a factor 1000.

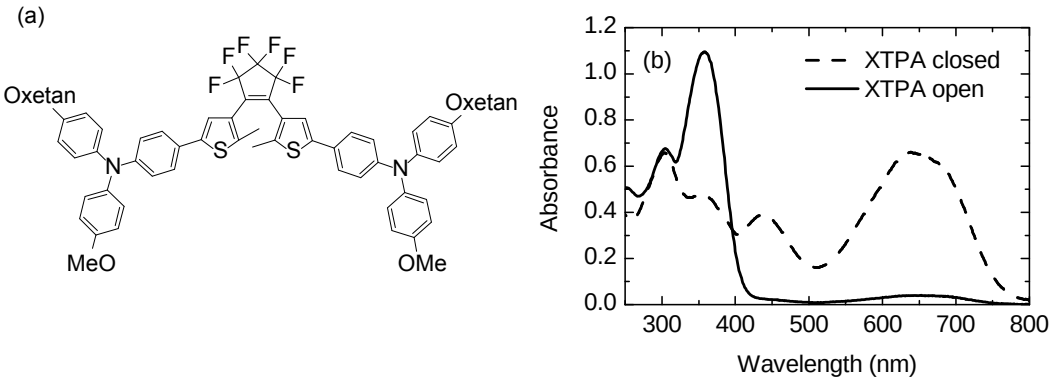

Figure 3.7: (a) Molecular structure of the open/transparent form of XTPA. (b) Absorbance spectra of XTPA dissolved in hexane obtained with a UV–Vis spectrometer (no OMF used). The solid line does not reach zero around 650 nm due to a few molecules remaining in the closed form. The spectra were measured by E. Maibach from Institut für Physikalische Chemie, Universität Köln.

3.2 Experimental prerequisites

To perform experiments with photochromic molecules adsorbed to OMF we need a method to apply the molecules onto the fibre surface. Moreover, for quantitative evaluation a reliable and precise detection method is needed. The methods used in this work are briefly described in the following. They are not limited to photochromic molecules but generally usable for organic dye molecules.

3.2.1 Attaching organic dye molecules to microfibres

A method to deposit thermally stable organic dye molecules on OMF used in our group is reported in [16]. A crucible filled with molecules – in this measurement the organic dye *3,4,9,10-perylene-tetracarboxylic dianhydride* (PTCDA) – was placed below the OMF and heated to 250 °C. Sublimated molecules reaching the OMF were then physically adsorbed to the "cold" fibre surface. This sublimation method provides a very good control of the surface coverage but works only for thermally stable molecules. Unlike PTCDA, most organic dye molecules undergo thermal decomposition before evaporating noticeably at atmospheric pressure. To deposit a larger variety of organic molecules on OMF, we developed a simple approach – the "drip method" [69] – which is illustrated in Fig. 3.8. The molecules are dissolved in a spectroscopic-grade solvent and a drop of this solution is dripped onto the OMF using a pipette. A thin film of the solution covers the fibre surface. Subsequently,

the solvent evaporates and the molecules remain adsorbed to the OMF. We have found that the polarity of the solvent strongly influences the number of molecules deposited on the fibre surface. Less polar solvents (heptane, toluene) leave much more molecules on the fibre compared to polar solvents (acetone, ethanol) for the same initial concentration of molecules. Moreover, by dripping a clean polar solvent onto the OMF we are able to remove the surface-adsorbed molecules.

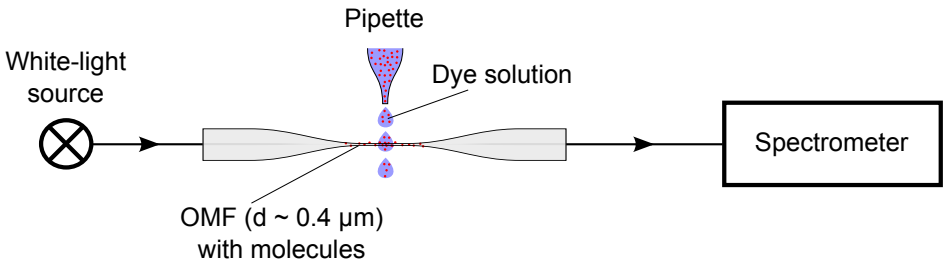

Figure 3.8: Deposition and detection of organic molecules.

3.2.2 Detection of organic dye molecules adsorbed to microfibres

To detect organic molecules adsorbed to an OMF we use ultra-sensitive absorption spectroscopy (Fig. 3.8) [16]. Light propagating through the OMF is strongly confined and provides a high intensity on the microfibre surface. This allows strong interaction of light with surface adsorbates. White light propagating through the OMF is partially absorbed by the surface-adsorbed molecules. The remaining white light is detected with a spectrometer. This makes it possible to measure the absorbance spectra of the molecules already at a very low surface coverage of less than 1 % of a monolayer [16]. This would in principle allow to observe isolated, non-interacting adsorbed molecules. However, we do not know whether the deposition from solution yields isolated molecules, such as the sublimation method, or rather islands, clusters or nanocrystals.

3.3 Basic photoswitching

With the ability to deposit photochromic molecules onto OMF we can study the photochromic behaviour of the molecules. To manipulate the molecular state, independently controlled light of two different wavelengths is needed. For this purpose an optical setup for detection and control of the molecules was installed.

3.3.1 Optical setup

Figure 3.9 shows the experimental setup of the photoswitching experiment. White light from a fibre-coupled halogen lamp (Avantes AvaLight-HAL) is filtered by a 435 nm longpass filter to exclude UV or blue wavelength components and is coupled into the fibre sample. The molecules are exposed to the white light during all measurements continuously, so they tend to be in the transparent form. The outcoupled white light passes a dichroic mirror and is detected either with a spectrometer (Avantes AvaSpec-ULS2048x16) or with a photomultiplier (Hamamatsu H5784).

UV light of 365 nm from an LED (Mightex FCS-0365-000) is coupled into the fibre sample through a beam shutter, a beam sampler and in reflection of the dichroic mirror. The UV light switches molecules to the coloured form and the UV exposure is controlled with the computer-controlled beam shutter (Thorlabs SH05). The UV light reflection of the beam sampler is used to monitor the beam shutter status. To prevent UV reflections from the sample entering the spectrometer or photomultiplier, a 400 nm longpass filter is installed in front of the detection device.

By monitoring the white-light transmission through the fibre the absorbance of the coloured molecule form can be obtained. For monitoring we use either the spectrometer which gives spectral information with slow acquisition time or the photomultiplier providing good time resolution but no spectral information. The fibre sample used in all photoswitching experiments has a waist diameter of 0.42 µm and a waist length of 5 mm. It is fabricated according to Sec. 1.2.3 as a doubly-spliced fibre providing good UV light transmission.

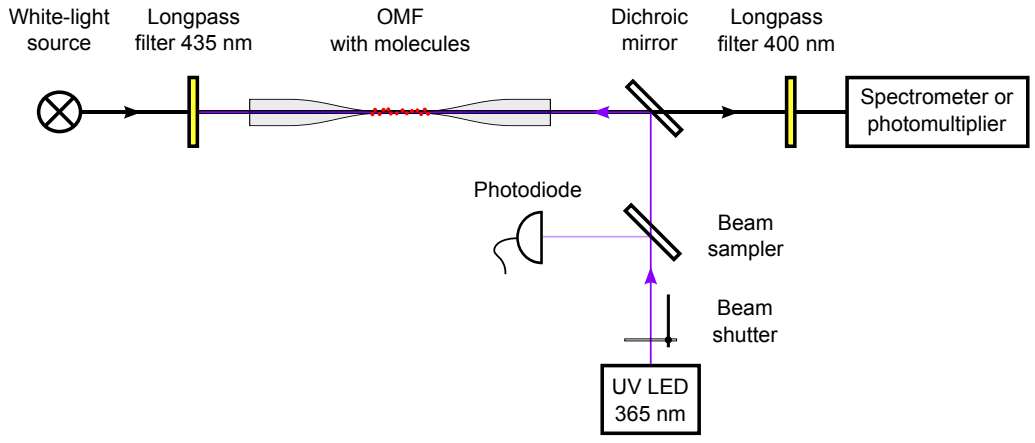

Figure 3.9: Setup of the absorption spectroscopy and photoswitching experiment.

3.3.2 Absorbance spectrum during photoswitching

After deposition of photochromic molecules not all surface-adsorbed molecules are still switchable. They continuously absorb light and can be considered as a background. Therefore, the spectral absorbance (Eq. (3.1)) of the switchable coloured molecules in the visible wavelength range can be determined by measuring the transmitted spectral power with all switchable molecules in the transparent form ($P_{\mathrm{ref}}(\lambda)$) and the actual transmitted spectral power during and after photocolouration ($P_{\mathrm{sig}}(\lambda)$). According to [16], the absorbance for the fibre-based surface absorption spectroscopy can be approximated as

$$A(\lambda) \approx \frac{N_{\mathrm{col}} \cdot \sigma(\lambda)}{\ln(10) A_{\mathrm{eff}}} \tag{3.6}$$

where N_{col} is the number of coloured molecules, $\sigma(\lambda)$ is the absorption cross section of the molecules, and A_{eff} is the effective mode area. This approximation is valid under the assumption that $\sigma(\lambda) \ll A_{\mathrm{eff}}$ which is fulfilled for our typical fibre and mode properties ($A_{\mathrm{eff}} \sim 10^{-9}$ cm^2) and the used molecules ($\sigma_{\mathrm{max}} \sim 10^{-15}$ cm^2). Thus, $A(\lambda)$ is proportional to the number of coloured molecules N_{col} adsorbed to the OMF and is therefore an excellent quantity to monitor photochromic processes.

The absorbance spectrum of spiroOH adsorbed to the OMF during photocolouration and photobleaching is illustrated in Fig. 3.10. After the deposition the molecules are exposed for 5 min to white light ($\lambda > 435$ nm) to switch all molecules to the transparent form. The white-light power in the wavelength range of $\lambda = 435$ nm to 750 nm, i.e. the wavelength range at which the coloured molecules absorb light, was approximately 10 nW*. Subsequently, the molecules are additionally exposed to 1.5 nW of UV light for 1 s. The absorbance increases during photocolouration and approaches the photostationary state, see Fig. 3.10a. This spectrum corresponds to the absorbance of surface-adsorbed coloured spiroOH molecules and is very similar to the absorbance spectrum of coloured spiroOH molecules in methanol, see Fig. 3.6.

After the UV exposure has stopped, the absorbance decreases since the white light switches the molecules back to the transparent form, see Fig. 3.10b. One can see that this photobleaching is slower than the photocolouration with UV. After approximately 1 s the absorbance decreased to 50% of the maximum value in the photostationary state meaning that 50% of the coloured molecules are switched

*The white-light power is very constant ($\Delta P < 1$ %) but the absolute value was not measured precisely. We roughly estimated an error of ±3 nW.

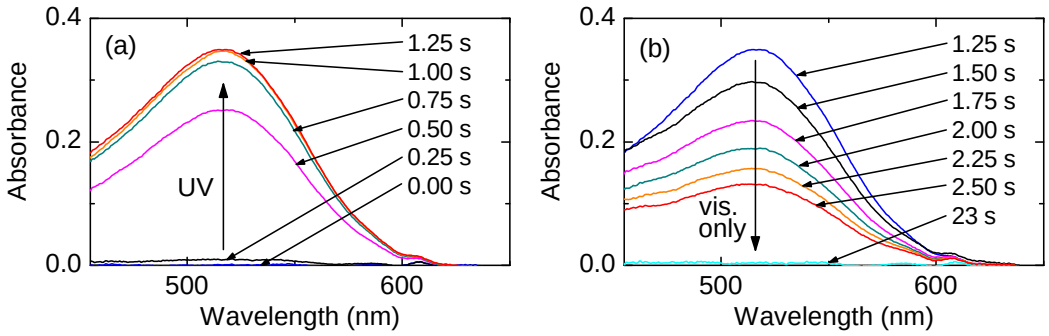

Figure 3.10: (a) Absorbance spectrum of spiroOH during exposure to 10 nW of white light and 1.5 nW of UV light. Starting with all molecules in the transparent form (blue curve), the absorbance increases due to the additional exposure to UV light ending in a stable absorbance in the photostationary state (red curve). The UV light exposure started between 0 s and 0.25 s. (b) Absorbance spectrum of spiroOH during exposure to white light only. Starting with the photostationary state (blue curve), the absorbance decreases after the UV exposure has stopped. The integration time per spectrum is for all figures 250 ms.

back to the transparent form. The absorbance has almost decreased to zero after 23 s indiacting that the switching cycle is nearly reversible.

The absorbance spectrum of coloured XTPA is obtained under exposure to 10 nW of white light and 3 nW of UV light, see Fig. 3.11. Similar to above, the transmitted white-light power with all molecules in the transparent form, i.e. without UV exposure, was used as the reference power. The absorbance spectrum of surface-adsorbed

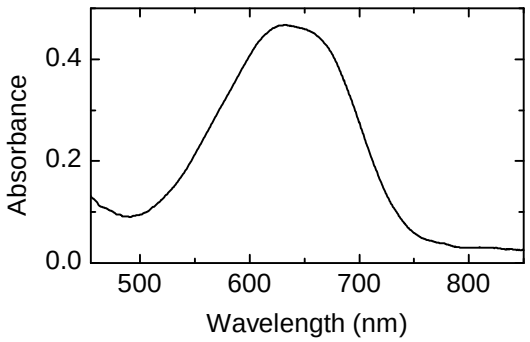

Figure 3.11: Absorbance spectrum of the closed/coloured form of surface-adsorbed XTPA in the photostationary state under illumination with 10 nW of white light and 3 nW of UV light. The integration time per spectrum is 250 ms.

XTPA in the visible wavelength range obtained with the OMF (Fig. 3.11) does not differ noticeably from the absorbance spectrum of XTPA in hexane (Fig. 3.7b).

3.3.3 Photoswitching dynamics

To obtain the temporal behaviour of the photoswitching process with a high time resolution the white-light transmission is monitored with the photomultiplier tube (PMT). The PMT measures the spectrally integrated white-light power with a time resolution of 50 µs. The output signal of the PMT is a voltage. Figure 3.12a illustrates the PMT voltage (dots) during photoswitching of spiroOH with 7 nW of UV light. The solid line displays the status of the UV light exposure which is measured with the photodiode detecting the sampled UV beam.

Before the molecules are exposed to UV light ($t < 0$ ms) all molecules are switched to the transparent form by white light. As soon as all molecules are in the transparent form the PMT voltage remains constant. At $t = 0$ ms the UV light exposure starts and the molecules are gradually switched to the coloured form. Coloured molecules absorb white light and therefore the PMT voltage decreases. After the UV light exposure has stopped ($t > 100$ ms) the white light slowly switches the molecules back to the transparent form and therefore the PMT voltage increases again.

We observed even without molecules that the fibre-coupled UV light causes an additional fluorescence signal on the PMT originating from the fibre. Thus, the PMT voltage is increased by a constant value during the UV exposure. This explains the step to lower voltages at $t = 100$ ms. At $t = 0$ ms a similar step is expected, but it is not visible due to the rapid change of the PMT voltage. This undesired side effect has to be considered for the data processing in the following section.

Data processing: Fully-automated absorbance calculation

From the PMT voltages the spectrally integrated absorbance A_{int} can be calculated by

$$A_{\mathrm{int}}(t) = -\log_{10} \frac{U_{\mathrm{pmt}}(t)}{U_{\mathrm{pmt,ref}}} \tag{3.7}$$

where $U_{\mathrm{pmt}}(t)$ is the PMT voltage at the time t and $U_{\mathrm{pmt,ref}}$ the reference PMT voltage with all molecules in the transparent form. Both voltages are already corrected from the constant PMT dark voltages. To automate the absorbance calculation

of multiple cycles, I have written a MATLAB program with the following requirements:

- Calculation of the maximum absorbance of each cycle.
- Calculation of the time-resolved absorbance during switching.

For the calculation of the maximum absorbance in one cycle the reference PMT voltage $U_{\mathrm{pmt,ref}}$ and the minimum PMT voltage $U_{\mathrm{pmt,min}}$ are needed. Both values are determined by fitting the data in specific time spans. The borders of the time spans are automatically calculated from the shutter photodiode response, shown with the numbers in the circles (1, 2 for $U_{\mathrm{pmt,ref}}$ and 5, 6 for $U_{\mathrm{pmt,min}}$) in Fig. 3.12a.

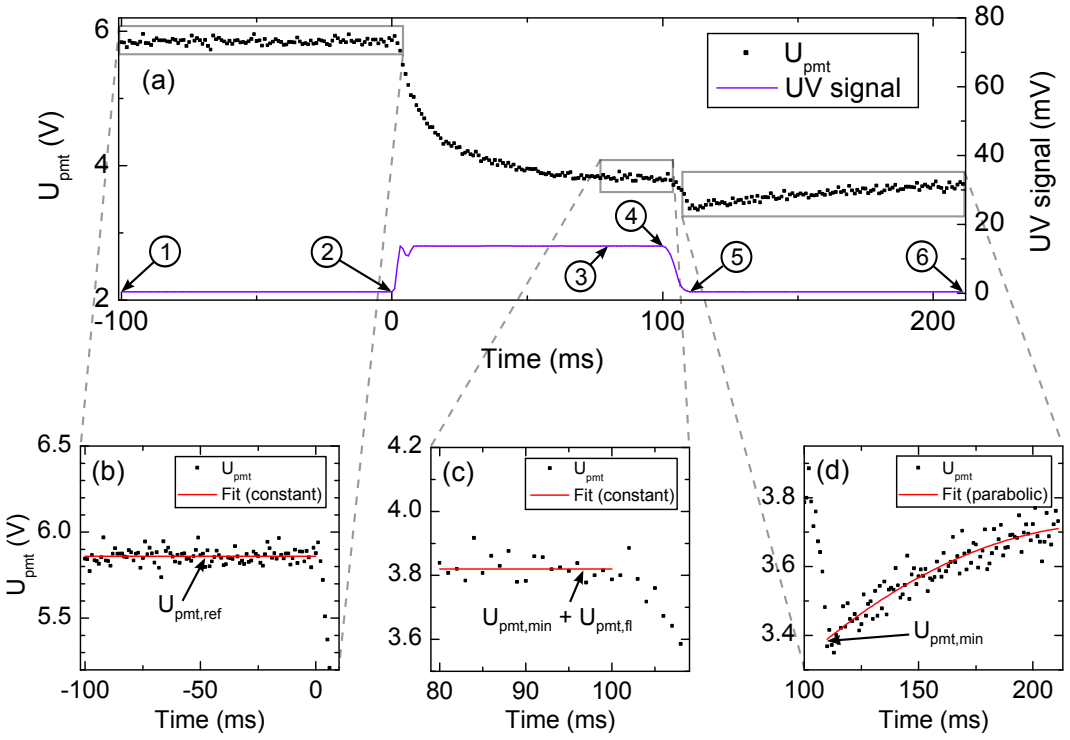

Figure 3.12: (a) The PMT voltage during one switching cycle is shown as dots and the UV light exposure as the solid line. At $t = 0$ ms the UV exposure is started and at $t = 100$ ms it is stopped. The small oscillation at $t = 0$ in the UV signal originates from a mechanical shock due to the shutter opening process. The numbered arrows determine the time ranges used for the fitting procedures and are automatically calculated by the MATLAB program. (b)–(d) Zoomed sections used for determination of the needed parameters.

The PMT voltage for $t < 0$ ms is nearly constant and $U_{\mathrm{pmt,ref}}$ is obtained by fitting a constant value, see Fig. 3.12b. In a similar way $U_{\mathrm{pmt,min}}$ is determined by fitting a parabolic function to the data right after the shutter has closed, see Fig. 3.12d. The maximum spectrally integrated absorbance of a cycle is then calculated by

$$A_{\mathrm{int,max}} = -\log_{10} \frac{U_{\mathrm{pmt,min}}}{U_{\mathrm{pmt,ref}}} \tag{3.8}$$

The time-resolved absorbance $A_{\mathrm{int}}(t)$ is calculated using the reference voltage $U_{\mathrm{pmt,ref}}$ and the actual voltage $U_{\mathrm{pmt}}(t)$. The values for $0 < t < 100$ ms have to be corrected from the UV-induced fibre fluorescence which was already mentioned before. For this purpose the PMT voltages right before (see Fig. 3.12c) and after (see Fig. 3.12d) the shutter is closed are determined. The PMT voltage originating from the fibre fluorescence $U_{\mathrm{pmt,fl}}$ is calculated by subtracting these two values and is then used to correct the PMT voltages during UV exposure

$$U_{\mathrm{pmt,corr}} = U_{\mathrm{pmt}} - U_{\mathrm{pmt,fl}} \qquad \text{for } 0 < t < 100 \text{ ms} \tag{3.9}$$

The fluorescence-corrected PMT voltage $U_{\mathrm{pmt,corr}}$ and the corresponding time-resolved absorbance A_{int} are illustrated in Fig. 3.13a and Fig. 3.13b, respectively. In both figures one can see a spike when the shutter closes ($t \approx 100$ ms). Since the shutter needs approximately 3 ms for closing and the UV beam is filling a large part of the shutter aperture, there is still a part of the UV light coupled into the

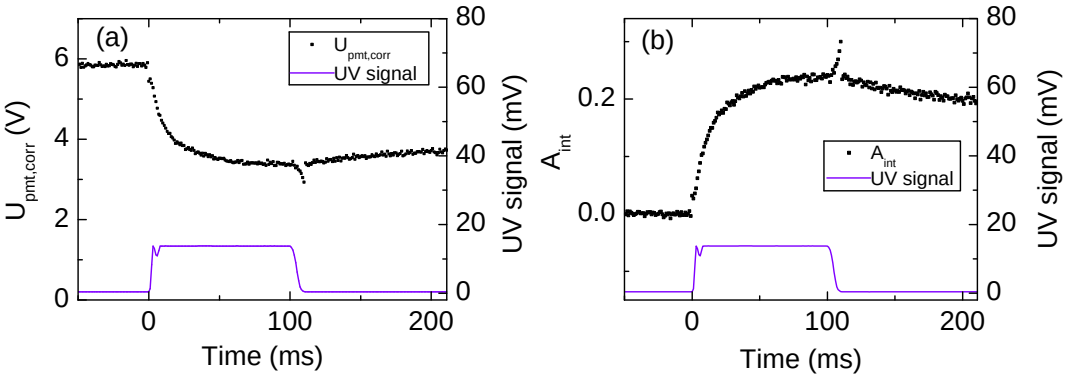

Figure 3.13: (a) The fluorescence-corrected PMT voltage during one photoswitching cycle is shown as dots and the UV light exposure as the solid line. At $t = 0$ ms the UV exposure (7 nW) is started and at $t = 100$ ms it is stopped. (b) The corresponding time-resolved absorbance (dots).

fibre sample during the closing process. This leads to a partial fibre fluorescence signal and is detected by the PMT. However, the MATLAB program still subtracts the full fluorescence value resulting in the spikes. These values are therefore not considered for the further analysis.

Data processing: Absorbance correction

As shown in Eq. (3.6) the absorbance at a fixed wavelength $A(\lambda)$ is proportional to the number of molecules N. This is a useful characteristic because it allows to directly deduce the relative number of coloured molecules from the absorbance. However, this proportionality is not necessarily true for the spectrally integrated absorbance A_{int} because of the wavelength-dependent PMT response and the inhomogeneous white-light spectrum. The consequence of the wavelength dependence is demonstrated in the following.

The reference voltage $U_{\text{pmt,ref}}$ can be described by an integral over the spectral signal strength $U_{\text{ref}}(\lambda)$:

$$U_{\text{pmt,ref}} = \int_{\lambda_1}^{\lambda_2} U_{\text{ref}}(\lambda)\ d\lambda \tag{3.10}$$

$U_{\text{ref}}(\lambda)$ is the measured voltage in a wavelength interval $[\lambda, \lambda + \Delta\lambda]$ when all molecules are in the transparent form. It is given by the product of the white-light spectrum reaching the PMT and the spectral sensitivity of the PMT. After transformations of Eq. (3.1) with $P(\lambda) \propto U(\lambda)$ we obtain

$$U_{\text{sig}}(\lambda) = U_{\text{ref}}(\lambda) \cdot 10^{-A(\lambda)} \tag{3.11}$$

By using Eq. (3.10) and Eq. (3.11) the measured spectrally integrated absorbance from Eq. (3.7) transforms to

$$A_{\text{int}} = -\log_{10} \frac{\int_{\lambda_1}^{\lambda_2} U_{\text{ref}}(\lambda) \cdot 10^{-A(\lambda)}\ d\lambda}{\int_{\lambda_1}^{\lambda_2} U_{\text{ref}}(\lambda)\ d\lambda} \tag{3.12}$$

From Eq. (3.12) one can see that A_{int} is not proportional to $A(\lambda)$ and is therefore not proportional to the number of molecules N. Since we know the spectral signal strength $U_{\text{ref}}(\lambda)$ and the shape of the spectral molecule absorbance $A(\lambda)$ it is possible to connect A_{int} with $A(\lambda)$. The two integrals in Eq. (3.12) are calculated numerically resulting in a dependence of A_{int} on $A(\lambda)$ at a fixed wavelength λ. The wavelength to which the measured absorbance is corrected can be chosen arbitrarily. We use the wavelength λ_{peak} at which the peak absorbance of the molecules

occurs. The correction can be described by a function $f_{\mathrm{corr}}(A_{\mathrm{int}})$ as follows

$$A(\lambda_{\mathrm{peak}}) = A_{\mathrm{int}} \cdot f_{\mathrm{corr}}(A_{\mathrm{int}}) \tag{3.13}$$

The correction functions $f_{\mathrm{corr}}(A_{\mathrm{int}})$ for the two used molecules have been determined numerically and are illustrated in Fig. 3.14a for spiroOH and in Fig. 3.14b for XTPA.

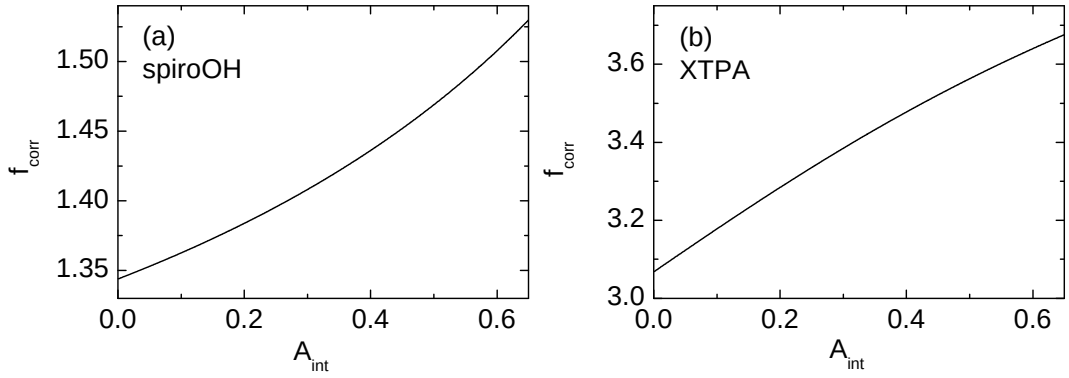

Figure 3.14: The correction function f_{corr} connecting the spectrally integrated absorbance A_{int} measured with the PMT with the peak absorbance of the molecules $A(\lambda_{\mathrm{peak}})$. Graphs (a) and (b) show f_{corr} which is numerically calculated for spiroOH and XTPA, respectively.

Photoswitching measurements

In this subsection the basic measurements to obtain the characteristics of the photoswitching processes are demonstrated, a more detailed analysis follows in the next chapter. The photoswitching dynamics of spiroOH and XTPA during one cycle is illustrated in Fig. 3.15a and 3.15b, respectively. Both measurement were performed with the same light powers (10 nW of white light continuously and 3 nW of UV light temporarily). The photocolouration process was stopped as soon as the system was prepared in the photostationary state.

The photobleaching and photocolouration curves can not be fitted with an exponential function. To get a rough indication about the speed of the photoswitching processes we therefore determine the time τ_{50} until 50 % of the maximum absorbance in the photostationary state is reached, see Tab. 3.1. Although the UV light power is lower than the white-light power, the photocolouration is systematically faster than the photobleaching. For spiroOH we have already seen this

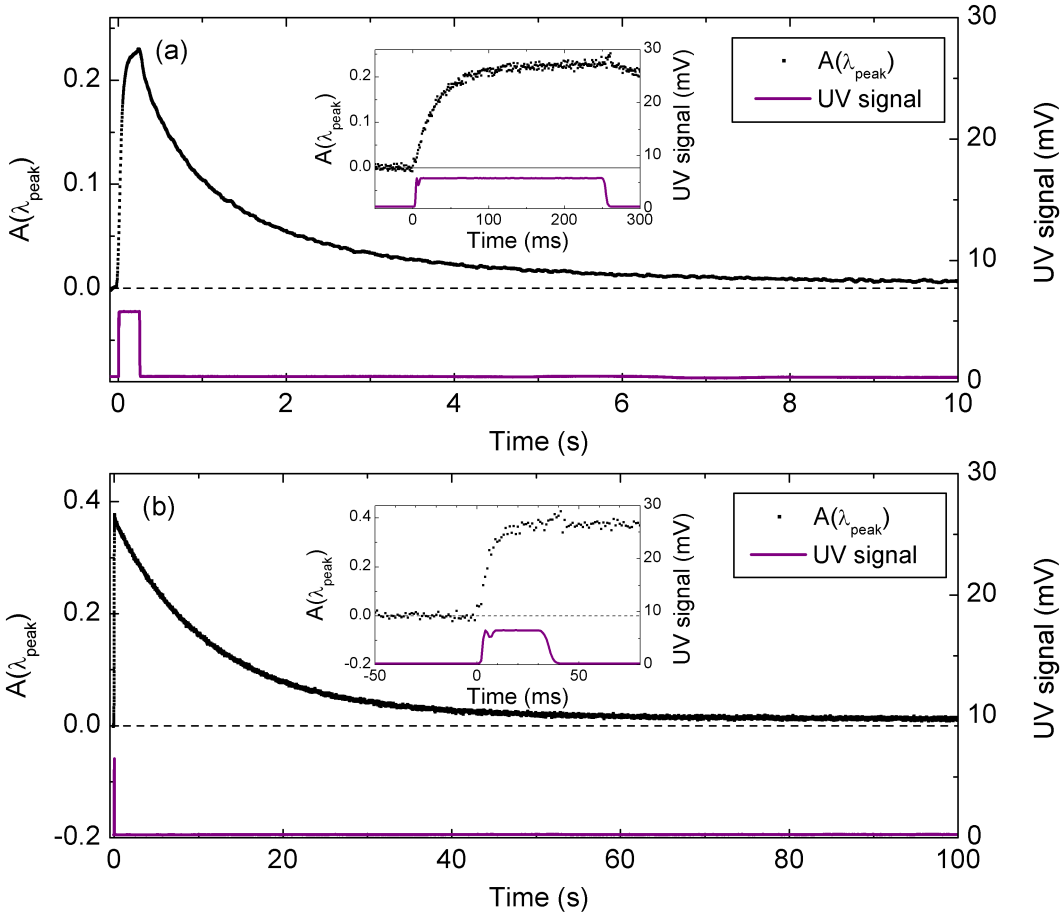

Figure 3.15: Photoswitching dynamics of spiroOH (a) and XTPA (b). The molecules were exposed to white light continuously. The spiroOH and XTPA molecules were additionally exposed to 3 nW of UV light for 250 ms and 30 ms, respectively. The dots denote the molecule absorbance $A(\lambda_{\text{peak}})$, the solid line the UV exposure, and the dashed black line zero absorbance. (a) and (b) were smoothed for visibility. The insets show the horizontally zoomed photocolouration process.

dependence in Sec. 3.3.2 in the measurements with the spectrometer. The switching speed depends on the quantum yield and the number of absorbed photons and is therefore influenced by the specific molecule properties and the light power at the absorbing wavelengths. Since photochromic molecules usually feature a much higher quantum yield for photocolouration than for photobleaching, it is not surprising that $\tau_{50,\text{col}} \ll \tau_{50,\text{bleach}}$.

For the long-term behaviour of photochromic applications the repeatability of

Molecule	$\tau_{50,\mathrm{col}}$ (ms)	$\tau_{50,\mathrm{bleach}}$ (s)
spiroOH	20 ± 2	0.6 ± 0.03
XTPA	5 ± 2	8.2 ± 0.2

Table 3.1: Overview of τ_{50} for the photocolouration and photobleaching processes.

the photoswitching processes is crucial. Therefore I also measured many subsequent photoswitching cycles with spiroOH, see Fig. 3.16. Each cycle consists of 100 ms photocolouration (3 nW of UV) followed by 20 s photobleaching (10 nW of white light). During photocolouration there is a certain probability for UV-induced photodestruction processes. These processes lead to non-switchable photoproducts which may still absorb light. Therefore, the maximum peak absorbance decreases with ascending cycles due to reduced amount of switchable molecules. Moreover, the minimum absorbance reached at the end of each photobleaching process increases, indicating that the molecules are gradually destroyed and continuously absorb white light.

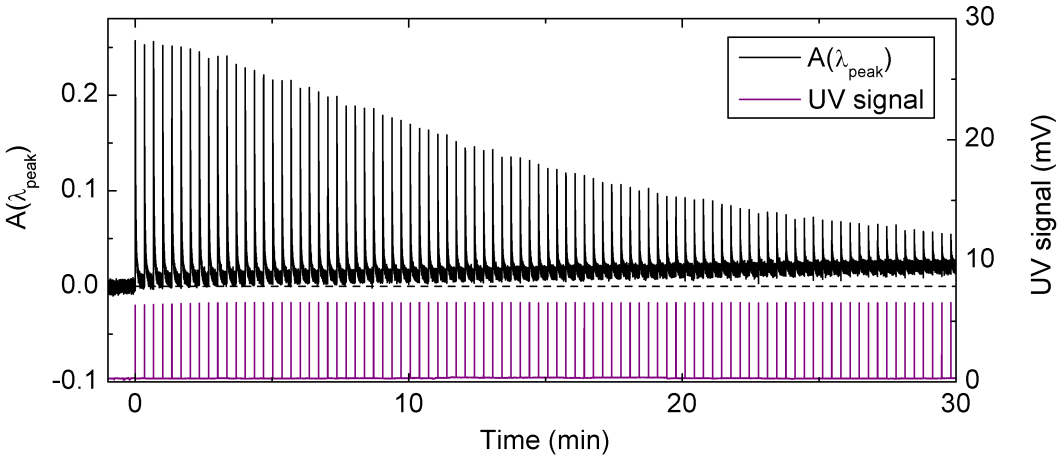

Figure 3.16: Many subsequent switching cycles of spiroOH. The molecules were exposed to white light continuously and for 100 ms additionally to 3 nW of UV light. The UV exposure was repeated each 20 s. The black line denotes the molecule absorbance $A(\lambda_{\mathrm{peak}})$, the violet line the UV exposure, and the dashed black line zero absorbance.

Chapter 4

Quantitative analysis of the photochromic processes

In the previous chapter I have shown the basic switching of photochromic molecules adsorbed to optical microfibres. With this ability it is possible to quantitatively analyse the main characteristics of the photochromic system. For this purpose I present in this chapter the reaction kinetics of the switching processes, the photostationary state under different illumination conditions and the performance loss due to photochemical degradation.

Note that throughout this chapter the measurements of the spectrally integrated absorbance were corrected according to Sec. 3.3.3 to provide the proportionality between absorbance $A(\lambda_{\mathrm{peak}})$ and the number of coloured molecules N_{col}. For readability I omit the notation "λ_{peak}".

4.1 Reaction kinetics of the switching processes

The typical photochromic switching processes can be described by two coupled nonlinear differential rate equations with the reaction rate $r(x,t)$ depending on the time t and the position x along the fibre

$$\begin{aligned} r(x,t) = \frac{\partial n_{\mathrm{col}}(x,t)}{\partial t} = &- k_{\mathrm{thermal,1}} \cdot n_{\mathrm{col}}(x,t) + k_{\mathrm{thermal,2}} \cdot n_{\mathrm{tr}}(x,t) \\ &- \Phi_{\mathrm{photobleach}} \cdot j_{\mathrm{col}}(x,t) + \Phi_{\mathrm{photocol}} \cdot j_{\mathrm{tr}}(x,t) \qquad (4.1) \\ -r(x,t) = \frac{\partial n_{\mathrm{tr}}(x,t)}{\partial t} = &+ k_{\mathrm{thermal,1}} \cdot n_{\mathrm{col}}(x,t) - k_{\mathrm{thermal,2}} \cdot n_{\mathrm{tr}}(x,t) \\ &+ \Phi_{\mathrm{photobleach}} \cdot j_{\mathrm{col}}(x,t) - \Phi_{\mathrm{photocol}} \cdot j_{\mathrm{tr}}(x,t) \qquad (4.2) \end{aligned}$$

where $n_{\mathrm{col}}(x,t)$ and $n_{\mathrm{tr}}(x,t)$ represent the linear density of coloured and transparent molecules, respectively, $k_{\mathrm{thermal,1}}$ and $k_{\mathrm{thermal,2}}$ the rate constants of the thermal

switching processes, $j_{\mathrm{col}}(x,t)$ and $j_{\mathrm{tr}}(x,t)$ the number of photons absorbed per unit length and per second by the coloured and transparent molecules, respectively, and $\Phi_{\mathrm{photobleach}}$ and Φ_{photocol} the quantum yields at the illumination wavelengths for photobleaching and photocolouration, respectively [70]. This rate equation model is valid under the assumption that chemical degradation is negligible and therefore the total molecule number per unit length is constant, $n_{\mathrm{tot}}(x,t) = n_{\mathrm{col}}(x,t) + n_{\mathrm{tr}}(x,t)$. For all measurements in this section the molecule spiroOH was used. Thermal (dark) switching has not been observed in our system at relevant time scales (minutes) and therefore we approximate $k_{\mathrm{thermal},1} = k_{\mathrm{thermal},2} = 0$.

4.1.1 Photobleaching: Exposure to white light

The transparent molecules do not absorb white light. Therefore, for the photo-induced switching with white light applies $j_{\mathrm{tr}} = 0$ and the molecules are switched only from the coloured to the transparent form. The rate equations for photobleaching are given by

$$\frac{\partial n_{\mathrm{col}}(x,t)}{\mathrm{d}t} = -\Phi_{\mathrm{photobleach}} \cdot j_{\mathrm{col}}(x,t) \tag{4.3}$$

$$\frac{\partial n_{\mathrm{tr}}(x,t)}{\mathrm{d}t} = +\Phi_{\mathrm{photobleach}} \cdot j_{\mathrm{col}}(x,t) \tag{4.4}$$

Note that the number of absorbed photons j_{col} depends on the linear molecule density n_{col}. Since we measure only the absorbance of the coloured molecules we can omit Eq. (4.4). Starting with Eq. (4.3) we use different mathematical approaches to model the measured absorbance (see Fig. 4.1). For all models we neglect different couplings of different molecules to the fibre-guided light, such as inhomogeneous local molecule adsorption sites or multi-mode light propagation in the fibre. I first present the considered mathematical models followed by the interpretation of the results.

"Mohn" model

Mohn et al. [70] investigated both theoretically and experimentally the photobleaching and photocolouration of a solid photochromic film under consideration of the dependence on the time t and the longitudinal position x in the film. This is comparable to our microfibre system and the solution for the absorbance after the

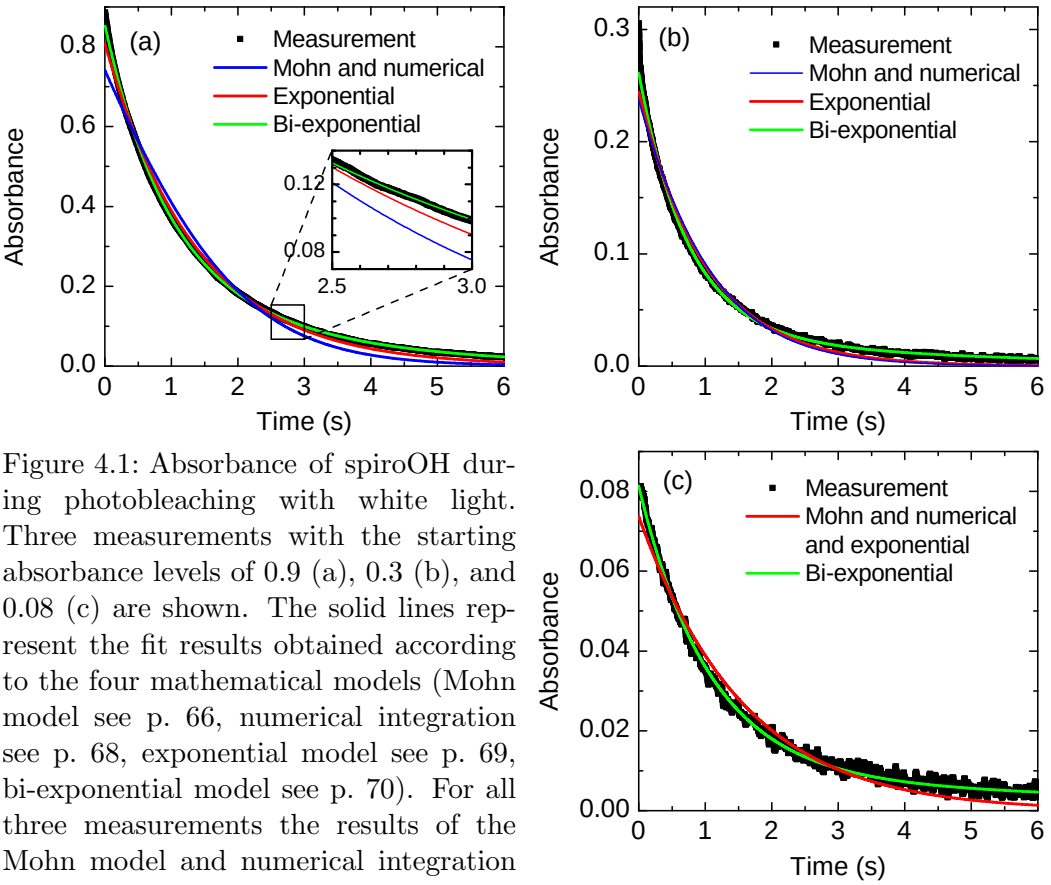

Figure 4.1: Absorbance of spiroOH during photobleaching with white light. Three measurements with the starting absorbance levels of 0.9 (a), 0.3 (b), and 0.08 (c) are shown. The solid lines represent the fit results obtained according to the four mathematical models (Mohn model see p. 66, numerical integration see p. 68, exponential model see p. 69, bi-exponential model see p. 70). For all three measurements the results of the Mohn model and numerical integration coincide. In (c) they additionally coincide with the exponential fit.

photochromic film is

$$A(t) = \log_{10}\left[1 + (10^{A_0} - 1) \cdot \exp\left(-\sigma I_0 \Phi_{\text{photobleach}} \cdot t\right)\right] \tag{4.5}$$

where A_0 is the absorbance after the photochromic film at $t = 0$, σ the absorption cross section of the coloured molecules at the illumination wavelength in cm^2, and I_0 the photon flux density at $x = 0$ in photons/(cm^2·s). To illustrate the absorbance behaviour according to this model the two limits of weak and strong absorption are considered. In the strong absorption limit ($A > 1$) we can approximate

$$A_{\text{strong}}(t) \approx \log_{10}\left[10^{A_0} \cdot \exp\left(-\sigma I_0 \Phi_{\text{photobleach}} \cdot t\right)\right] \tag{4.6}$$

which results in a linear temporal behaviour of the absorbance:

$$A_{\mathrm{strong}}(t) \approx A_0 - \sigma I_0 \Phi_{\mathrm{photobleach}} \cdot t / \ln 10 \tag{4.7}$$

This linear decrease can be explained considering the amount of absorbed light. At high absorbance levels most of the light is absorbed – for example 90 % for $A = 1$ and 99 % for $A = 2$ – and therefore the total rate of absorbed photons is nearly constant. Since every absorbed photon switches a molecule according to the quantum yield with a certain probability, the number of switched molecules per time interval is also nearly constant leading to a linear absorbance decrease.

In the weak absorption limit ($A \ll 1$) we approximate $10^{A_0} \approx 1 + A_0 \cdot \ln 10$ and the absorbance can be expressed as

$$A_{\mathrm{weak}}(t) \approx \log_{10} \left[1 + A_0 \cdot \ln 10 \cdot \exp\left(-\sigma I_0 \Phi_{\mathrm{photobleach}} \cdot t\right)\right] \tag{4.8}$$

With $\log_{10}(1 + x) \approx x / \ln 10$ we obtain an exponential temporal behaviour of the absorbance

$$A_{\mathrm{weak}}(t) \approx A_0 \cdot \exp\left(-\sigma I_0 \Phi_{\mathrm{photobleach}} \cdot t\right) \tag{4.9}$$

These two different dependencies are most clearly demonstrated in Fig. 4.1a. The curve calculated according to the Mohn model first decreases linearly for the high absorbance levels and approaches an exponential decrease for the low absorbance levels.

Numerical integration

Instead of solving the position-dependent rate equation at each position x individually one can consider the ensemble parameters, i.e. the total number of coloured molecules $N_{\mathrm{col}}(t)$ and the total number of absorbed photons per second $J_{\mathrm{col}}(t)$. Under this assumption Eq. (4.3) transforms to

$$\frac{\mathrm{d}N_{\mathrm{col}}(t)}{\mathrm{d}t} = -\Phi_{\mathrm{photobleach}} \cdot J_{\mathrm{col}}(t) \tag{4.10}$$

To use this equation for modelling the measured absorbance we have to replace N_{col} and J_{col} by terms including A. As shown in Eq. (3.6) the number of coloured molecules N_{col} is proportional to the absorbance A

$$N_{\mathrm{col}} \propto A \tag{4.11}$$

The dependence of the number of absorbed photons per second J_{col} on the absorbance A can be derived from the definition of A

$$A = -\log_{10}\frac{P_{\mathrm{sig}}}{P_{\mathrm{ref}}} = -\log_{10}\frac{P_{\mathrm{ref}} - P_{\mathrm{abs}}}{P_{\mathrm{ref}}} \tag{4.12}$$

where P_{abs} is the total absorbed power. P_{abs} can be thus written as

$$P_{\mathrm{abs}} = P_{\mathrm{ref}} \cdot (1 - 10^{-A}) \tag{4.13}$$

and since the total number of absorbed photons is proportional to the total absorbed power follows

$$J_{\mathrm{col}} \propto 1 - 10^{-A} \tag{4.14}$$

Eq. (4.10) can be transformed using Eq. (4.11) and Eq. (4.14) an we obtain

$$\frac{\mathrm{d}A(t)}{\mathrm{d}t} \propto -\Phi_{\mathrm{photobleach}} \cdot (1 - 10^{-A(t)}) \tag{4.15}$$

With this equation the measured absorbance was modelled by numerical integration. Within numerical uncertainties this method gave the same fitting results as the Mohn solution indicating that the x-dependence can be indeed avoided by using the ensemble parameters N_{col} and J_{col}.

Exponential function

In the weak absorption limit ($A \ll 1$) the last term in Eq. (4.15) can be approximated with $1 - 10^{-A} \approx \ln(10) \cdot A$ and thus becomes linear in A. The solution of the resulting rate equation

$$\frac{\mathrm{d}A(t)}{\mathrm{d}t} \propto -\Phi_{\mathrm{photobleach}} \cdot A(t) \tag{4.16}$$

is an exponential function $A_0 \cdot \exp(-kt)$, where k is the rate constant. The corresponding fits are also illustrated in Fig. 4.1.

Interpretation

For the low absorbance levels the light intensity along the microfibre waist is nearly constant. If the light-molecule coupling is constant for all molecules we therefore expect an exponential decay of the absorbance. All three discussed models show this exponential behaviour in the low absorption limit and the fitting results of the

three models coincide, see Fig. 4.1c. However, the models do not fit the measured photobleaching dynamics perfectly. The tendency of the deviation for $A \ll 1$ in Fig. 4.1c shows for $t < 1.5$ s a steeper slope of the measured data than the modelled curves whereas the slope of the measrued data becomes shallower for $t > 1.5$ s. The same behaviour occurs also for the high absorbance measurements (Fig. 4.1a,b) indicating that there is a systematic tendency that the switching process starts with a high switching rate which decreases with time. From this behaviour I conclude that the light-molecule coupling varies for different molecules meaning that the light-molecule coupling distribution is inhomogeneous. This can be explained by the following effects:

- The molecules are not only adsorbed on the microfibre waist, but also on the taper. The light intensity on the surface of the taper is smaller because of the larger fibre diameter. Therefore, the molecules on the taper are switched systematically slower meaning that the rate of this process is smaller than for molecules on the waist.

- The strength of the light-molecule coupling might vary due to inhomogeneous local molecule adsorption sites. The resulting different switching probabilities correspond to a distribution of rates.

- Possible multi-mode light propagation in the OMF results in a strong and fast absorption of modes with high surface intensity (high rate) and weak and slow absorption of modes with low surface intensity (low rate).

The inhomogeneous distribution of rate constants can be considered by assuming a multi-exponential decay. Already a **bi-exponential decay** describes the measured data better than the other curves, see Fig. 4.1 (green line). The use of two rate constants results in a stronger curvature of the absorbance decay. To allow a further quantitative analysis of the photoswitching processes we have to neglect the inhomogeneous light-molecule coupling distribution. This is done by applying the exponential model with a single switching rate constant. The single switching rate constant can be interpreted as the empirical mean value of the inhomogeneous rate constant distribution.

4.1.2 Photocolouration: Exposure to UV and white light

The system becomes much more complicated if the molecules are additionally exposed to UV light. The UV light is absorbed by both the transparent and coloured

molecules. The resulting system of two nonlinear coupled differential equations cannot be solved analytically. We could try to fit the measurement data by numerical integration of the rate equation, as shown in the section before. However, since the theory for the photobleaching dynamics did not give a good agreement to the measurement, we first would have to improve the model in Sec. 4.1.1.

4.1.3 Molecules ratio in the photostationary state

Exposing the molecules continuously to both UV and white light leads to a dynamic equilibrium state (photostationary state). In the photostationary state the ratio of coloured to transparent molecules does not change. The molecules ratio depends on the absorption cross section and quantum yield of the molecules in both forms, as well as on the irradiating light intensity. Therefore we can use the UV and white-light power to control the molecules ratio in the photostationary state.

In the following I describe and apply a method to determine the ratio of the photobleaching rate to the photocolouration rate. For this purpose we control the photocolouration rate by varying the UV power. This allows us to determine the fraction of coloured molecules in the resulting photostationary state.

Rate equation model for the photostationary state

Using the exponential model the photochromic system can be described by the rate equation

$$\frac{\mathrm{d}N_{\mathrm{col}}}{\mathrm{d}t} = -k_{\mathrm{vis}} \cdot N_{\mathrm{col}} + k_{\mathrm{uv}} \cdot N_{\mathrm{tr}} \tag{4.17}$$

where k_{vis} is the photobleaching rate depending on the white-light power and k_{uv} is the photocolouration rate depending on the UV power. To approach the photostationary state the light powers are kept constant. In the photostationary state the molecules distribution does not change and therefore

$$\frac{\mathrm{d}N_{\mathrm{col,stat}}}{\mathrm{d}t} = -k_{\mathrm{vis}} \cdot N_{\mathrm{col,stat}} + k_{\mathrm{uv}} \cdot N_{\mathrm{tr,stat}} = 0 \tag{4.18}$$

where the label “stat” means that the system is in the photostationary state. For the molecules ratio follows

$$\frac{N_{\mathrm{col,stat}}}{N_{\mathrm{tr,stat}}} = \frac{k_{\mathrm{uv}}}{k_{\mathrm{vis}}} \tag{4.19}$$

By assuming a constant number of switchable molecules ($N_{\mathrm{tot}} = N_{\mathrm{col,stat}} + N_{\mathrm{tr,stat}}$) we obtain

$$N_{\mathrm{col,stat}} = N_{\mathrm{tot}} \cdot \frac{k_{\mathrm{uv}}/k_{\mathrm{vis}}}{1 + k_{\mathrm{uv}}/k_{\mathrm{vis}}} \tag{4.20}$$

This equation directly connects the switching rates ratio $k_{\mathrm{uv}}/k_{\mathrm{vis}}$ with the fraction of coloured molecules in the photostationary state $N_{\mathrm{col,stat}}/N_{\mathrm{tot}}$.

UV power dependence

The white light power, which is used for monitoring the absorbance as well as for switching, is kept constant at 10 nW during all measurements. Therefore, the photobleaching rate k_{vis} can be assumed to be constant. The molecules distribution in the photostationary state is controlled by modulating the photocolouration rate k_{uv}. The photocolouration rate k_{uv} depends linearly on the UV power

$$k_{\mathrm{uv}} \propto P_{\mathrm{uv}} \tag{4.21}$$

The initial UV power is 1.5 nW and the corresponding photocolouration rate is labelled $k_{\mathrm{uv,0}}$, the photobleaching rate with constant white-light power of 10 nW is labelled $k_{\mathrm{vis,0}}$. Enhancing the UV power by f_{enh} (UV power enhancement factor) leads to a modified switching rate

$$k_{\mathrm{uv}}(f_{\mathrm{enh}}) = f_{\mathrm{enh}} \cdot k_{\mathrm{uv,0}} \tag{4.22}$$

The number of coloured molecules depending on f_{enh} can be then written as

$$N_{\mathrm{col,stat}}(f_{\mathrm{enh}}) = N_{\mathrm{tot}} \cdot \frac{f_{\mathrm{enh}} \cdot k_{\mathrm{uv,0}}/k_{\mathrm{vis,0}}}{1 + f_{\mathrm{enh}} \cdot k_{\mathrm{uv,0}}/k_{\mathrm{vis,0}}} \tag{4.23}$$

In Fig. 4.2 the fraction of coloured molecules in the photostationary state depending on f_{enh} is illustrated for three different $k_{\mathrm{uv,0}}/k_{\mathrm{vis,0}}$. By measuring $N_{\mathrm{col,stat}}(f_{\mathrm{enh}})$ and analysing the shape of the curve we can thus determine the initial switching rates ratio $k_{\mathrm{uv,0}}/k_{\mathrm{vis,0}}$. $N_{\mathrm{col,stat}}(f_{\mathrm{enh}})$ can be obtained by measuring multiple subsequent cycles with varying UV power.

Photodestruction

We have to take into account that the UV light not only switches photochromic molecules, but also initiates side reactions leading to non-switchable photoproducts. This means that the total number of switchable molecules N_{tot} decreases after each

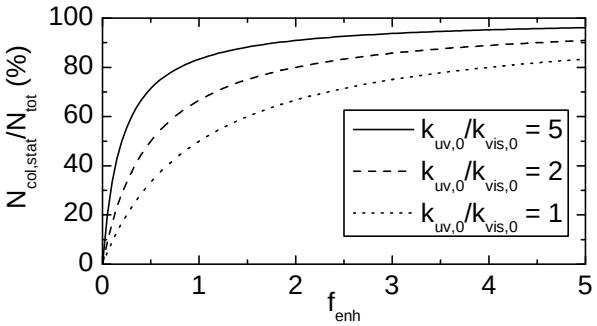

Figure 4.2: Simulated curves for the normalized number of coloured molecules depending on the UV power enhancement factor f_{enh}. The curves are calculated for three different initial switching rate ratios $k_{\mathrm{uv},0}/k_{\mathrm{vis},0}$.

cycle. Therefore we choose to deposit the same UV dose in each cycle. This allows us to assume an exponential decrease of $N_{\mathrm{tot}}(n)$. For only a few cycles a linear decrease is a valid approximation. We verified this by measuring the absorbance in the photostationary state for 10 cycles with the same UV power and exposure time, see Fig. 4.3. The total number of switchable molecules available in the n-th cycle is

$$N_{\mathrm{tot}} = N_{\mathrm{tot},0} - \Delta N \cdot n \tag{4.24}$$

where $N_{\mathrm{tot},0}$ is the number of switchable molecules at the beginning of the experiment and ΔN the number of destroyed molecules per cycle.

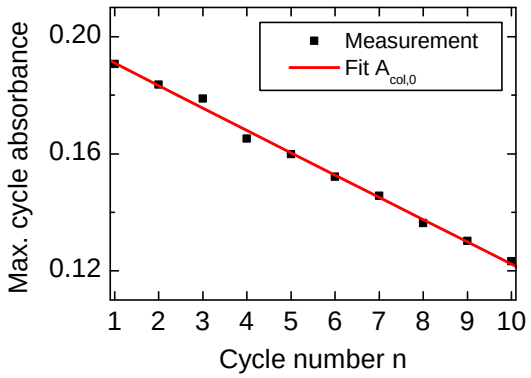

Figure 4.3: Absorbance in the photostationary state for several cycles. In each cycle the molecules were exposed to 7.5 nW of UV light for 100 ms. The absorbance decreases due to the photodestruction of switchable molecules. The red line shows the corresponding linear fit.

Measurement

Including the linear decrease due to photodestruction in Eq. (4.23) we obtain

$$N_{\mathrm{col,stat}}(f_{\mathrm{enh}}, n) = (N_{\mathrm{tot},0} - \Delta N \cdot n) \cdot \frac{f_{\mathrm{enh}} \cdot k_{\mathrm{uv},0}/k_{\mathrm{vis},0}}{1 + f_{\mathrm{enh}} \cdot k_{\mathrm{uv},0}/k_{\mathrm{vis},0}} \tag{4.25}$$

Since the white-light absorbance A is proportional to N_{col} we can rewrite this equation to

$$A_{\mathrm{stat}}(f_{\mathrm{enh}}, n) = (A_{\mathrm{col},0} - \Delta A \cdot n) \cdot \frac{f_{\mathrm{enh}} \cdot k_{\mathrm{uv},0}/k_{\mathrm{vis},0}}{1 + f_{\mathrm{enh}} \cdot k_{\mathrm{uv},0}/k_{\mathrm{vis},0}} \tag{4.26}$$

where $A_{\mathrm{col},0}$ is the maximum absorbance if all initially switchable molecules are in the coloured form and ΔA is the absorbance decrease in each cycle due to destructed molecules. The absorbance $A_{\mathrm{col}}(f_{\mathrm{enh}}, n)$ depending on the UV enhancement factor f_{enh} and the cycle number n is measured according to the following procedure:

The molecules are continuously exposed to white light with a constant power of 10 nW and are therefore completely switched to the transparent form. In the first cycle, they are additionally illuminated with 1.5 nW of UV light until the photostationary state is reached (500 ms). Once the UV exposure has stopped, the molecules are switched back to the transparent form by the white light. In four subsequent cycles the UV power is increased (3 nW, 4.5 nW, 6 nW, 7.5 nW) and in five more cycles reversely decreased, see Fig. 4.4. The exposure time of each cycle is varied inversely to keep the UV dose, and thus the photodestruction per cycle, constant. The reverse sequence is used to obtain a symmetric sequence to optimally separate the asymmetric reduction of molecules with the fit.

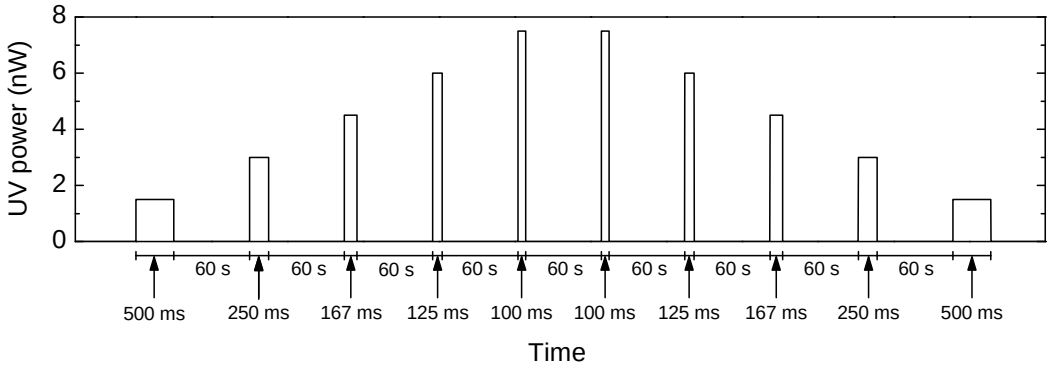

Figure 4.4: The UV exposure sequence used in the measurement shown in Fig. 4.5a.

The result of this measurement including the fit according to Eq. (4.26) is shown in Fig. 4.5a. For the first five cycles the shape expected from the example in Fig. 4.2 is reproduced. In the first cycle, with the lowest UV power of 1.5 nW, less molecules are switched to the coloured form, whereas in the fifth cycle, with the highest UV power of 7.5 nW, more molecules are switched. The cycles 6–10 with reverse UV power trend show the mirrored behaviour.

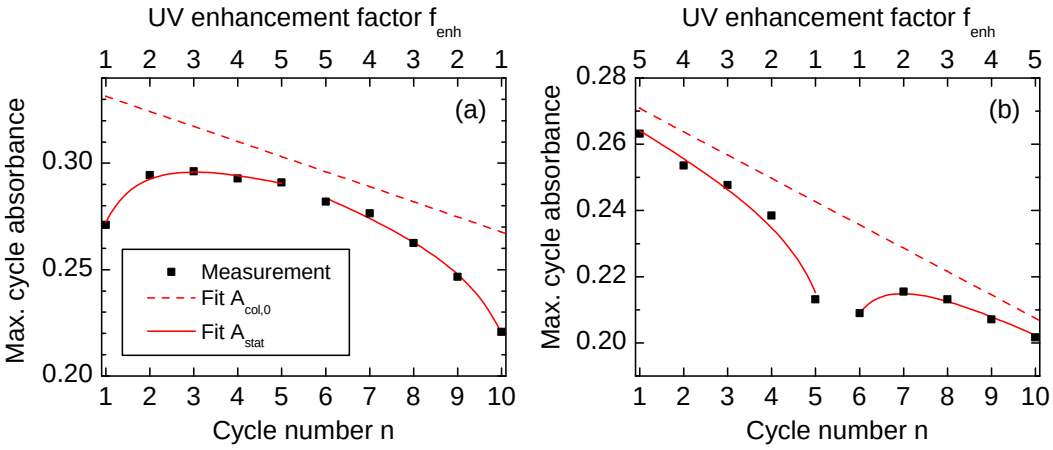

Figure 4.5: Absorbance in the photostationary state for 10 cycles with varying UV power, [1.5, 3, 4.5, 6, 7.5] nW and backwards in (a) and [7.5, 6, 4.5, 3, 1.5] nW and backwards in (b). The exposure time of each cycle was varied inversely to the power to keep the UV dose constant. The solid lines are the fit curves according to Eq. (4.26) taking photodestruction (dashed line) into account.

In. Fig. 4.5b a similar measurement is illustrated where we start with the highest UV power which is decreased is the four subsequent cycles and then increases in the cycles 6–10. Both measurements have been performed twice. Before starting each of the four measurements new molecules were deposited. The resulting fit parameters are listed in Tab. 4.1.

There is a systematic deviation of the switching rates ratio $k_{\mathrm{uv},0}/k_{\mathrm{vis},0}$ depending on the UV power trend. I do not suggest that the kinetics are responsible for this effect, since every systematic deviation, for example if low UV powers switch less molecules than expected, would lead in both measurements to the same systematic error. An exponential decrease (instead of the linear approximation) of $A_{\mathrm{col,n}}$ due to photodestruction would decrease the systematic deviation. However, the measurement in Fig. 4.3, which has been reproduced, does not support this suggestion. The systematic deviation indicates that there is a non-understood hysteresis effect.

Measurement number	UV power trend	$A_{\mathrm{col},0}$	ΔA	$k_{\mathrm{uv},0}/k_{\mathrm{vis},0}$ ($P_{\mathrm{uv}} = 1.5$ nW)
1 (Fig.4.5a)	increasing, decreasing	0.34	0.0071	4.6
2	increasing, decreasing	0.24	0.0066	5.1
3 (Fig.4.5b)	decreasing, increasing	0.28	0.0070	7.8
4	decreasing, increasing	0.29	0.0068	7.8

Table 4.1: The resulting fit parameters of the four measurements. The UV power trend designates if the UV power was first increased in the cycles 1–5 and then decreased in the cycles 6–10, or vice versa. $A_{\mathrm{col},0}$ is the maximum absorbance if all initially switchable molecules are in the coloured form and ΔA the absorbance decrease in each cycle due to destructed molecules.

The average switching rates ratio is $k_{\mathrm{uv},0}/k_{\mathrm{vis},0} = 6.3$ meaning that 1.5 nW of UV switches the molecules 6.3 times faster than 10 nW of white light. Since the origin of the systematic deviation is not understood, the error is estimated by the largest deviation of the measured switching ratio from the average value, i.e. $\Delta(k_{\mathrm{uv},0}/k_{\mathrm{vis},0}) = 1.7$ for the UV power of 1.5 nW. The errors for other UV powers are calculated according to the propagation of uncertainty. For 1.5 nW of UV power we obtain

$$\frac{N_{\mathrm{col,stat}}}{N_{\mathrm{tot}}} = \frac{1 \cdot k_{\mathrm{uv}}}{k_{\mathrm{vis}} + 1 \cdot k_{\mathrm{uv}}} = (86 \pm 3)\ \% \tag{4.27}$$

meaning that in the photostationary state about 86 % of the molecules that are still switchable are in the coloured form. With the highest available UV power of 7.5 nW we obtain $k_{\mathrm{uv},0}/k_{\mathrm{vis},0} = 31.5 \pm 8.5$ and even (97 ± 1) % of the molecules are switched to the coloured form. The UV-power dependent molecule fraction in the photostationary state is illustrated in Fig. 4.6.

4.2 Cyclability

Photochromic molecules lose their ability to switch upon illumination, which is called fatigue. The switching process itself is non-destructive, but side reactions lead to non-switchable photoproducts (by-products) [65]. The parameter to quantify how often a system with photochromic molecules can be switched is the cyclability Z_{50} [65]. The cyclability of a photochromic system is an important parameter to characterize the practicability of photochromic applications. The cyclability depends not only on the molecule but also on the measurement conditions: Do

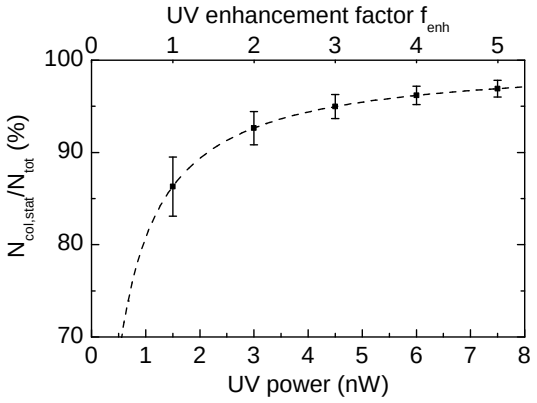

Figure 4.6: Fraction of coloured molecules in the photostationary state depending on the UV light power. The points illustrate the specific UV powers used in the experiment.

we try to switch 80 % or 99 % of the molecules in each cycle? Are all molecules exposed to the same UV power, or does the UV intensity decrease along the OMF? Therefore, the experimentally observed cyclability is a system-specific parameter.

In the following I characterize the cyclability of spiroOH adsorbed to the OMF under different measurement conditions. The molecules are switched back and forth in many subsequent cycles and the maximum white-light absorbance in each cycle is measured. The absorbance is measured for each cycle independently meaning that for each individual cycle the reference power is determined right before the photocolouration starts. In this way deviations due to white-light absorbing by-products are avoided. Therefore, the measured maximum cycle absorbance is proportional to the number of molecules switched to the coloured form in the respective cycle. From this measurement the cyclability of our photochromic system is then determined.

4.2.1 Dependence on UV power

To study the interplay of system parameters, in two similar experiments the switching UV light power was set to 3.2 nW and 7 nW, respectively. The UV pulse time was 100 ms and the molecules were photobleached in each cycle with white light for 20 s. With the higher UV power of 7 nW the photostationary state was reached during each switching cycle (Fig. 4.7a), and the absorbance decreased to 50 % after 20 cycles (Fig. 4.7b), i.e. $Z_{50}(7\ \text{nW}) = 20$. With 3.2 nW the photostationary state was not fully reached in each cycle (Fig. 4.7c) and we obtain $Z_{50}(3.2\ \text{nW}) = 41$ (Fig. 4.7d). From Fig. 4.7a and 4.7c I conclude that in both measurements we

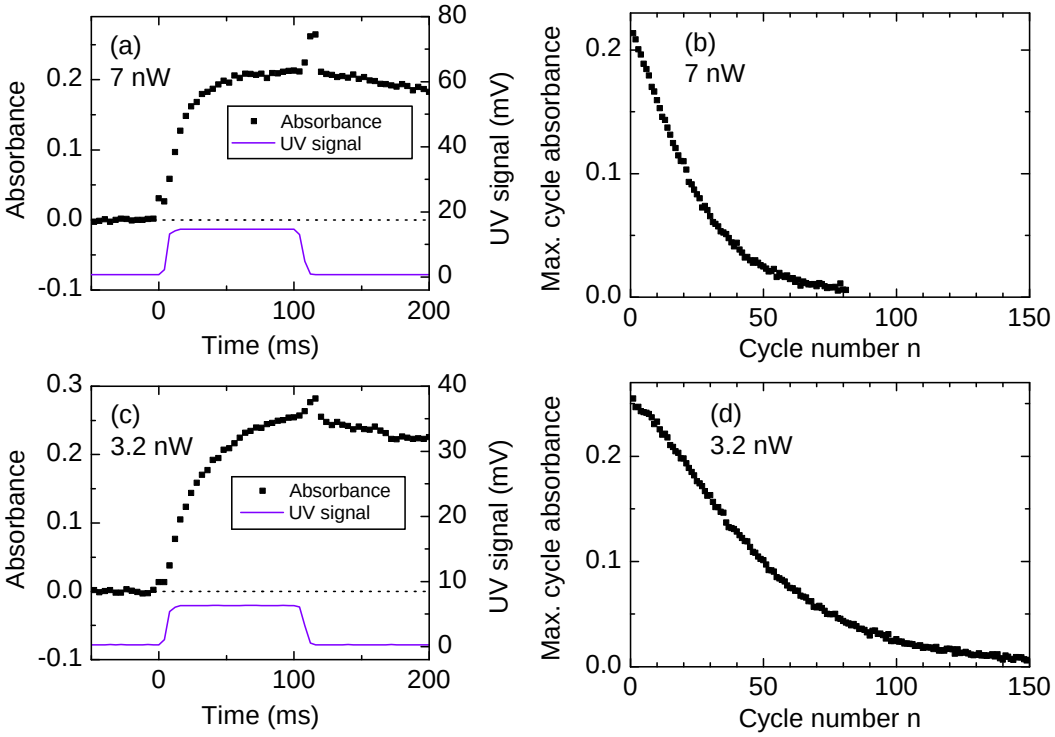

Figure 4.7: The two left plots show the absorbance of spiroOH during photocolouration due to exposure to 7 nW (a) and 3.2 nW (c) of UV light for 100 ms. The two right plots show the corresponding maximum cycle absorbance for many subsequent cycles. For deposition spiroOH dissolved in toluene was used.

have switched the vast majority of molecules to the coloured form and back in each cycle. The total UV dose accumulated until reaching Z_{50} was very similar in both experiments, 14 nJ and 13.1 nJ for the 7 nW and 3.2 nW experiment, respectively. This confirms that the molecules are destroyed due to the UV light and not due to the switching process itself.

As a comparison to spiroOH, I also measured the cyclability of XTPA adsorbed to the OMF. The molecules were switched for 30 ms with 3.2 nW of UV light, see Fig. 4.8a. The photobleaching of XTPA with white light is much slower than for spiroOH such that the molecules had to be exposed in each cycle to white light for 15 min. The absorbance was reduced to 50 % after $Z_{50} = 14$ cycles (Fig. 4.8b), corresponding to a deposited UV energy of 1.4 nJ. The deposited UV energy to reach 50 % absorbance is for XTPA a factor 10 less than for spiroOH.

A possible explanation might be the state-dependent photodestruction. For di-

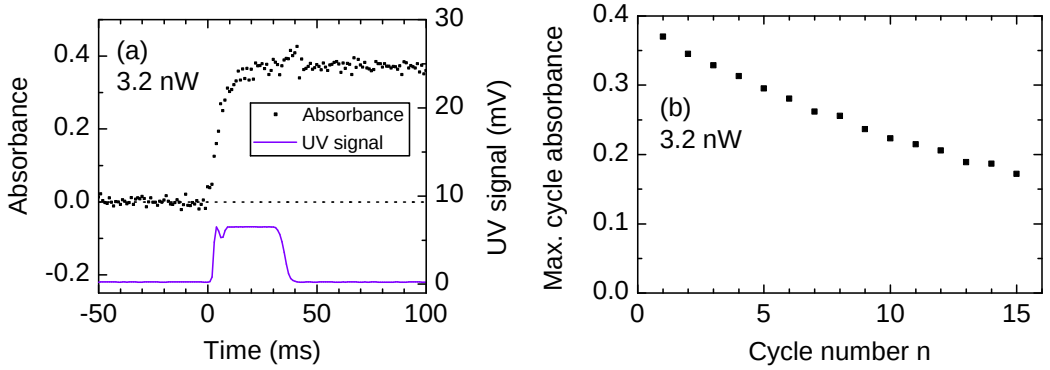

Figure 4.8: (a) The absorbance of XTPA during photocolouration due to exposure to 3.2 nW of UV light for 30 ms. (b) The corresponding maximum cycle absorbance for many subsequent cycles. For deposition XTPA dissolved in heptane was used.

arylethenes it is generally assumed that side-reactions are predominantly induced to the coloured form, whereas the transparent form is more stable under UV illumination [24, 71, 72]. This assumption has been verified for at least one diarylethene compound [73]. Since the "front" molecules on the OMF see more UV light than the "back" molecules, and moreover the quantum yield for the photocolouration process is very high, the position-dependent distribution of the molecules states is very inhomogeneous. The coloured molecules at the front are exposed to the highest power of UV light and therefore the photodestructive reaction should be very efficient.

4.2.2 Dependence on number of adsorbed molecules

By choosing the solvent of our photochromic solution we can roughly control the number of molecules deposited on the OMF. The less polar the solvent, the more molecules stick to the polar silica surface. After deposition of few drops of spiroOH in toluene, which we have used in the previous experiments, the white-light absorbance in the photostationary state under illumination with UV was ∼0.25. The UV transmission is typically on the order of tens of percent, meaning that the UV light reaches all molecules.

We performed an experiment with spiroOH dissolved in the non-polar solvent heptane. Using this solution, much more molecules remain on the OMF and the white-light absorbance reaches ∼0.75 under illumination with UV for 100 ms. Here, the photostationary state is not fully reached. We observed that no UV light can

be detected after the OMF. All UV light is absorbed by the molecules meaning that the molecules adsorbed at the front end of the OMF are switched and the molecules at the back end are not exposed to UV. Therefore, only a fraction of the molecules is switched. In Fig. 4.9 the absorbance during one cycle (a) and maximum cycle absorbance (b) is illustrated. After 150 cycles more than 70% of the initial absorbance can be still reached, corresponding to a cyclability of $Z_{50} \approx 300$. Compared to the experiment with less surface adsorbed molecules but similar exposure parameters (Fig. 4.7c,d, $Z_{50} \approx 41$), the cyclability is enhanced by a factor 7. A suggestion for an explanation of this cyclability enhancement is the large "reservoir" of switchable molecules on the OMF. If a molecule is destroyed due to the UV light, and assuming that this by-product absorbs less UV light than the initially switchable molecule, the UV light can switch other molecules at a further position along the OMF which have not been switched before.

The cyclability obtained so far remains behind the values obtained for macroscopic samples of molecules in solution, which can be up to $Z_{50} \sim 10^4$ for spiropyranes [62,74] and $Z_{50} \sim 10^5$ for diarylethenes [24]. A reason for the lower cyclability using OMF might be for example the oxygen-containing atmosphere causing light-induced oxidation [64, 75].

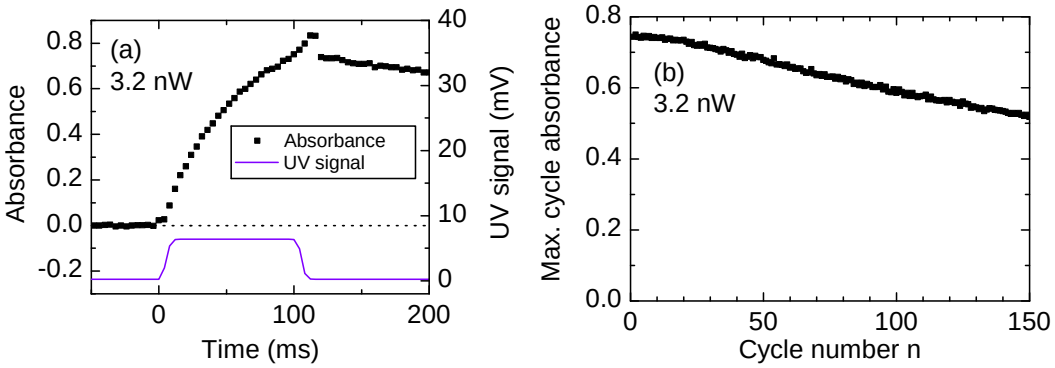

Figure 4.9: (a) The absorbance of spiroOH during photocolouration due to exposure to 3.2 nW of UV light for 100 ms. (b) The corresponding maximum cycle absorbance for many subsequent cycles. For deposition spiroOH dissolved in heptane was used.

4.2.3 Photodestruction quantum yield

The fatigue characteristics of photochromic molecules can be quantified by the photodestruction quantum yields of the two molecule forms ($\Phi_{\mathrm{destr,col}}$, $\Phi_{\mathrm{destr,tr}}$). For this purpose the molecules are prepared in the transparent form and are then continuously exposed to UV light, see Fig. 4.10. For the analysis the following assumptions are taken into account:

- Before starting the photocolouration all molecules are prepared in the transparent form.
- The UV power is high enough to switch most of the molecules into the coloured form ($N_{\mathrm{col,stat}}/N_{\mathrm{tot}} > 90$ %).
- For the analysed data at the beginning of the experiment ($t < 2$ s) the number of destroyed molecules is small and therefore the UV absorption due to these by-products is neglected.

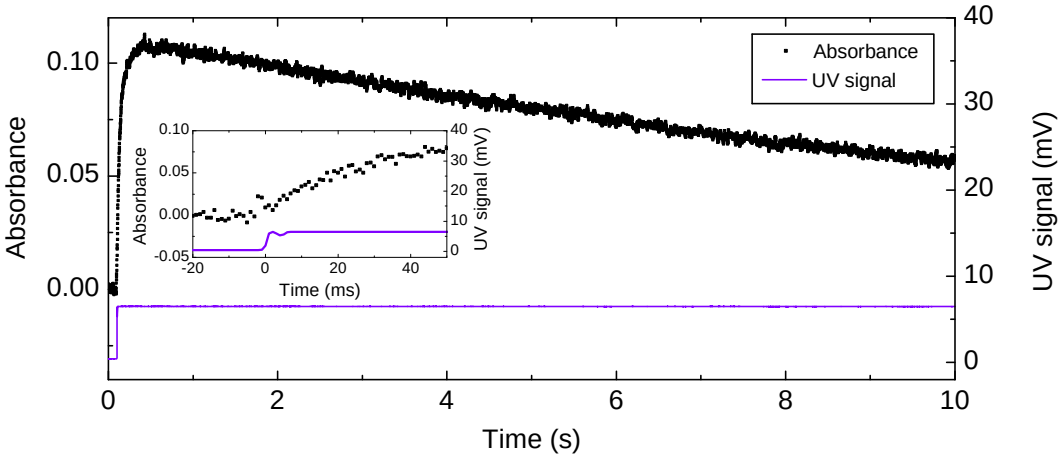

Figure 4.10: Fast photocolouration and slow photodestruction of spiroOH under UV exposure (3 nW) used for the determination of the respective quantum yields. The inset shows the horizontally zoomed photocolouration process.

When starting the photocolouration all molecules are in the transparent form. The initial rise of the number of coloured molecules N_{col} can be described by the rate equation

$$\begin{aligned}\left(\frac{\mathrm{d}N_{\mathrm{col}}}{\mathrm{d}t}\right)_{\mathrm{photocol}} &= \Phi_{\mathrm{photocol}} \cdot J_{\mathrm{abs,tr}}(\mathrm{UV}) \\ &= \Phi_{\mathrm{photocol}} \cdot \sigma_{\mathrm{tr}}(\mathrm{UV}) \cdot N_{\mathrm{tr}} \cdot I(\mathrm{UV}) \\ &\approx \Phi_{\mathrm{photocol}} \cdot \sigma_{\mathrm{tr}}(\mathrm{UV}) \cdot N_{\mathrm{tot}} \cdot I(\mathrm{UV}) \end{aligned} \tag{4.28}$$

where $J_{\mathrm{abs,tr}}(\mathrm{UV})$ is the number of UV photons absorbed per second by the transparent molecules, $\sigma_{\mathrm{tr}}(\mathrm{UV})$ is the absorption cross section of the transparent molecules at the UV wavelength and $I(\mathrm{UV})$ is the UV photon flux density in photons/ $(\mathrm{cm}^2 \cdot \mathrm{s})$. When the photostationary state is reached the absorbance should be stable. However, Fig. 4.10 shows that the absorbance decreases after the maximum absorbance level is reached. This can be attributed to the fatigue of molecules meaning that switchable molecules are destroyed. From the absorbance decrease I conclude that the molecules emerging from the UV-initiated side reactions absorb less white light than the coloured spiroOH molecules. The rate equation for the photodestruction process can be expressed as

$$\left(\frac{\mathrm{d}N_{\mathrm{col}}}{\mathrm{d}t}\right)_{\mathrm{destr}} \approx -\Phi_{\mathrm{destr,col}} \cdot J_{\mathrm{abs,col}}(\mathrm{UV}) - \Phi_{\mathrm{destr,tr}} \cdot J_{\mathrm{abs,tr}}(\mathrm{UV}) \tag{4.29}$$

where $J_{\mathrm{abs,col}}(\mathrm{UV})$ is the number of UV photons absorbed per second by the coloured molecules. Assuming that the vast majority of molecules is switched to the coloured form, and therefore neglecting the light absorption due to transparent molecules, Eq. (4.29) transforms to

$$\begin{aligned}\left(\frac{\mathrm{d}N_{\mathrm{col}}}{\mathrm{d}t}\right)_{\mathrm{destr}} &\approx -\Phi_{\mathrm{destr,col}} \cdot \sigma_{\mathrm{col}}(\mathrm{UV}) \cdot N_{\mathrm{col}} \cdot I(\mathrm{UV}) \\ &\approx -\Phi_{\mathrm{destr,col}} \cdot \sigma_{\mathrm{col}}(\mathrm{UV}) \cdot N_{\mathrm{tot}} \cdot I(\mathrm{UV}) \end{aligned} \tag{4.30}$$

Since the absorbance is proportional to the number of coloured molecules $(\mathrm{d}N_{\mathrm{col}}/\mathrm{d}t) = (\mathrm{d}A/\mathrm{d}t)$ and using Eq. (4.28) and Eq. (4.30), we get for the quantum yield ratio

$$\frac{\Phi_{\mathrm{photocol}} \cdot \sigma_{\mathrm{tr}}(\mathrm{UV})}{\Phi_{\mathrm{destr,col}} \cdot \sigma_{\mathrm{col}}(\mathrm{UV})} \approx -\frac{\left(\frac{\mathrm{d}A}{\mathrm{d}t}\right)_{\mathrm{photocol}}}{\left(\frac{\mathrm{d}A}{\mathrm{d}t}\right)_{\mathrm{destr}}} \tag{4.31}$$

The absorption cross section at $\lambda = 365$ nm is very similar for the two molecules forms of spiroOH, see Fig. 3.6, and therefore Eq. (4.31) can be approximated to

$$\frac{\Phi_{\text{photocol}}}{\Phi_{\text{destr,col}}} \approx -\frac{\left(\frac{\mathrm{d}A}{\mathrm{d}t}\right)_{\text{photocol}}}{\left(\frac{\mathrm{d}A}{\mathrm{d}t}\right)_{\text{destr}}} \tag{4.32}$$

Thus, the quantum yield ratio can be determined from the slope of the photocolouration process right after starting the UV exposure and the slope of the absorbance decrease in the photostationary state. By fitting the rates from Fig. 4.10 we obtain for spiroOH

$$\frac{\Phi_{\text{photocol}}}{\Phi_{\text{destr,col}}} \approx 500 \tag{4.33}$$

In contrast to the photodestruction, the photocolouration quantum yield is known for many molecules. Therefore, this method can be used to determine the quantum yield of the destructive side reactions of the coloured molecules.

For an improved quantitative analysis two aspects should be considered. First, the assumption that in the photostationary state all molecules are in the coloured form is not perfectly true. With 3 nW of UV light we switch approximately 93 % of the molecules into the coloured form. This can be improved by using a higher UV power. Second, the created by-products might absorb white light. Therefore, the measured white-light absorbance originates not only from the coloured molecules but also from the by-products. This background can be included into the calculations if the absorbance of the by-products in known. For this purpose the molecules can be exposed to UV until the absorbance is constant. This constant absorbance should originate from all by-products.

4.3 Summary and conclusion

Photochromic molecules adsorbed to optical microfibres could be repeatedly switched between the two forms by UV light and white light in a controlled manner. The experimental setup with a fibre-coupled white-light source and an UV LED is very stable and provides the opportunity for monitoring the photoswitching dynamics with sub-millisecond time resolution as well as for automated and precise long-term measurements.

I have presented time-resolved measurements of the switching processes. The light-induced switching dynamics of the molecules was modelled in a rough approximation as a rate equation system. This simple model neglects different (in-

homogeneous) couplings of different molecules to the fibre-guided light. In this way the dependence on various unknown parameters and lengthy numerical calculations were avoided, while being able to approximately extract the important main properties of the systems.

With the analysis of the photostationary state under different illumination conditions it was possible to extract the fraction of coloured molecules in the photostationary state for specific UV and white-light powers. By choosing the proper UV light power we can therefore prepare the photochromic system with a desired fraction of coloured molecules. Moreover, with the analysis of the photostationary state we can determine the ratio of the photocolouration and photobleaching rate providing information about the reaction kinetics.

The performance loss due to chemical degradation was characterized in two different ways, by repeatedly switching the molecules and identifying the system cyclability as well as by determining the ratio between the photoswitching and photodestruction quantum yields. The cyclability as a system parameter showed a strong dependence on the measurement conditions. For spiroOH the cyclability could be enhanced by a factor 7 by increasing the surface coverage. The large number of molecules can be considered as a reservoir of molecules where the destroyed molecules are replaced by still switchable molecules. A limiting factor for the system cyclability is the absorption of UV light by the destroyed molecules. Therefore, the fraction of UV light accessible for photocolouration is reduced.

In conclusion, I have demonstrated a new system of photochromic molecules adsorbed to OMF which can be used to study photochromic processes. The functionality which is typically known from macroscopic diluted samples can successfully be transferred to the microfibre environment. This fibre-based method is an alternative approach to comparable experiments using photochromic molecules in solution (e.g. [18]) or spin-coated samples with selectable substrate (e.g. [19]). The system has indeed nanoscale properties: minute light powers at the nanowatt level are sufficient to switch molecules between conformal states, but at the same time cause photodestruction already.

Chapter 5

Outlook

In the first part of this thesis I have presented a non-destructive method to optically measure the diameter of an OMF with an accuracy of better than 2 %. In the second part I have reported on the characterization of a photochromic microfibre system using surface-adsorbed organic photochromic molecules. In this chapter I finally suggest some improvements and prospects of both experiments.

5.1 Diameter measurement and harmonic generation

Origin of the systematic deviation

The fibre diameters determined by the SEM measurement were systematically larger than the results of the optical measurement. It would be worthwhile to check if this deviation is due to the SEM measurement or if it is a limitation of our optical method. For this purpose the fibre diameter should be verified using a more accurate measurement, such as for example transmission electron microscopy, which provides sub-nanometre resolution.

Harmonic generation aided fabrication process

The fibre samples used in my experiments were fabricated in collaboration with A. Rauschenbeutel at the University of Mainz (now TU Vienna). The precision of the fabricated fibre diameter is experimentally limited to ± 5 % [35]. Moreover, due to inaccurate fibre preparation in the pulling machine unnoticed deviations can occur resulting in fibre diameters several hundreds of nanometres off the target fibre diameter. Currently, we design and develop a new fibre pulling machine in our group. The pulling process could be improved with respect to the target fibre diameter by combining the final pulling sequence with real-time harmonic generation measurements. Aiming for a specific fibre diameter, the laser has to be tuned to the

wavelength at which harmonic generation is expected due to the phase-matching condition. By real-time monitoring of the harmonic response we can thus stop the pulling process controllably right when the harmonic signal appears, similar to [15]. Moreover, the fibre diameter measurement is an excellent auxilliary tool for the construction of the new fibre pulling machine since it allows in-situ analysis of the fibre diameter.

5.2 Photochromic molecules

Ideal cyclability

For characterization and comparison of switchable molecules it would be very useful to define an intrinsic cyclability of the molecules, independent of the optical system. This "ideal cyclability" would specify how often on average a single molecule could be switched before it undergoes a destructive side reaction. As the photodestruction is only caused by the UV light (see Sec. 4.2.1), the critical switching step is the photocolouration. An upper limit to the ideal cyclability can thus be obtained by measuring the ratio of the UV-induced photocolouration and photodestruction quantum yields of the transparent molecules.

$$Z_{50,\mathrm{ideal}} = \frac{\Phi_{\mathrm{photocol}}}{\Phi_{\mathrm{destr,tr}}} \tag{5.1}$$

The measurement in Sec. 4.2.3 (Fig. 4.10) has to be modified such that in the photostationary state the majority of molecules is in the transparent form. Basically, it would be preferable to use only transparent molecules to avoid distortions of the measured photodestruction quantum yield (of the transparent molecules) due to the different photodestruction quantum yield of the coloured molecules. However, a few coloured molecules are needed for monitoring. The number of molecules adsorbed to the OMF should not be too large to provide that all molecules are exposed to the UV. This can be achieved by using diluted molecules solutions, e.g. diluted spiroOH in toluene. The UV power should be reduced such that only a small fraction ($N_{\mathrm{col,stat}}/N_{\mathrm{tot}} < 10$ %) of molecules is switched to the coloured form. This can be done according to the photostationary state analysis in Sec. 4.1.3. The quantum yields Φ_{photocol} and $\Phi_{\mathrm{destr,tr}}$ can be then obtained from the resulting measured absorbance similar to Sec. 4.2.3.

Reduction of light-molecules coupling inhomogeneities

An improvement of the experimental results could be achieved by reducing light-molecule coupling inhomogeneities. For this purpose the origin of the inhomogeneities has to be identified. Molecules on the fibre taper could be avoided by systematic and careful measurements on position-dependent effects or by increasing the length of the microfibre waist and therefore simplified molecules deposition. Multi-mode light propagation can be basically avoided by decreasing the microfibre waist diameter, but the fabrication of thinner OMF with high (UV) light transmission is challenging. If the inhomogeneities originate from the interaction of molecules with the fibre surface, the basic experiment has to be modified. For example, the OMF could be immersed in a polar solution with photochromic molecules. The photoswitching and monitoring would be provided by interaction of the evanescent field with floating molecules.

Improving the system performance

The performance of the photochromic microfibre system is limited by the cyclability and the switching speed. Experiments with photochromic molecules in solution show a superior cyclability to our system. The fatigue resistance in our experiments might be improved by changing the environment such as excluding oxygen by placing the OMF in a noble gas atmosphere or embedding the molecules in a polymer matrix. In the latter case a low refractive index polymer would be required to maintain light guidance in the OMF. State controlled deposition could increase the number of molecules participating in the switching process.

The switching speed could be increased by orders of magnitude by applying tailored laser pulses. The switching process of diarylethene molecules themselves happens on a picosecond timescale (in solution) [24]. We expect the dynamics of adsorbed molecules to be governed by a similar time scale.

Photo-optical switch

Our experiments with surface-adsorbed photochromic molecules showed that the light transmission through OMF can be controlled by the molecules absorption. However, the absorbed light also switches molecules and therefore significantly influences the molecules state. In a parallel project in our group a single optical microfibre interferometer is developed [76]. Since the switching of photochromic molecules comes along with a change in the refractive index [24, 77, 78], we could

apply photochromic molecules to the interferometer to dispersively control the fibre transmission at non-absorbing wavelengths of the molecules. For this purpose the OMF has to be coated with a thick photochromic film or immersed in a photochromic solution.

Bibliography

[1] J. Hecht, "Illuminating the origin of light guiding," *Opt. Photon. News*, vol. 10, no. 10, pp. 26–30, 1999.

[2] G. J. Tearney, M. E. Brezinski, B. E. Bouma, S. A. Boppart, C. Pitris, J. F. Southern, and J. G. Fujimoto, "In vivo endoscopic optical biopsy with optical coherence tomography," *Science*, vol. 276, no. 5321, pp. 2037–2039, 1997.

[3] T. G. Giallorenzi, J. A. Bucaro, A. Dandridge, G. H. Sigel, and J. H. Cole, "Optical fiber sensor technology," *IEEE J. Quantum Elect.*, vol. 18, no. 4, 1982.

[4] Y. Jeong, J. Sahu, D. Payne, and J. Nilsson, "Ytterbium-doped large-core fiber laser with 1.36 kw continuous-wave output power," *Opt. Express*, vol. 12, no. 25, pp. 6088–6092, 2004.

[5] G. Brambilla, V. Finazzi, and D. J. Richardson, "Ultra-low-loss optical fiber nanotapers," *Opt. Express*, vol. 12, no. 10, pp. 2258–2263, 2004.

[6] S. Leon-Saval, T. Birks, W. Wadsworth, P. S. J. Russell, and M. Mason, "Supercontinuum generation in submicron fibre waveguides," *Opt. Express*, vol. 12, no. 13, pp. 2864–2869, 2004.

[7] J. Ward, D. O'Shea, B. J. Shortt, M. J. Morrissey, K. Deasy, and S. N. Chormaic, "Heat-and-pull rig for fiber taper fabrication," *Rev. Sci. Instrum.*, vol. 77, no. 8, p. 083105, 2006.

[8] F. Warken, A. Rauschenbeutel, and T. Bartholomaeus, "Fiber pulling profits from precise positioning," *Photon. Spectra*, vol. 42, no. 3, p. 73, 2008.

[9] L. Tong, J. Lou, and E. Mazur, "Single-mode guiding properties of subwavelength-diameter silica and silicon wire waveguides," *Opt. Express*, vol. 12, no. 6, pp. 1025–1035, 2004.

[10] P. Dumais, F. Gonthier, S. Lacroix, J. Bures, A. Villeneuve, P. G. J. Wigley, and G. I. Stegeman, "Enhanced self-phase modulation in tapered fibers," *Opt. Lett.*, vol. 18, no. 23, pp. 1996–1998, 1993.

[11] T. A. Birks, W. J. Wadsworth, and P. S. J. Russell, "Supercontinuum generation in tapered fibers," *Opt. Lett.*, vol. 25, no. 19, pp. 1415–1417, 2000.

[12] R. R. Gattass, G. T. Svacha, L. Tong, and E. Mazur, "Supercontinuum generation in submicrometer diameter silica fibers," *Opt. Express*, vol. 14, no. 20, pp. 9408–9414, 2006.

[13] D. A. Akimov, A. A. Ivanov, A. N. Naumov, O. A. Kolevatov, M. V. Alfimov, T. A. Birks, W. J. Wadsworth, P. S. J. Russell, A. A. Podshivalov, and A. M. Zheltikov, "Generation of a spectrally asymmetric third harmonic with unamplified 30-fs cr:forsterite laser pulses in a tapered fiber," *Appl. Phys. B*, vol. 76, pp. 515–519, 2003.

[14] V. Grubsky and A. Savchenko, "Glass micro-fibers for efficient third harmonic generation," *Opt. Express*, vol. 13, no. 18, pp. 6798–6806, 2005.

[15] V. Grubsky and J. Feinberg, "Phase-matched third-harmonic UV generation using low-order modes in a glass micro-fiber," *Opt. Commun.*, vol. 274, no. 2, pp. 447–450, 2007.

[16] F. Warken, E. Vetsch, D. Meschede, M. Sokolowski, and A. Rauschenbeutel, "Ultra-sensitive surface absorption spectroscopy using sub-wavelength diameter optical fibers," *Opt. Express*, vol. 15, no. 19, pp. 11952–11958, 2007.

[17] M. Irie and K. Sayo, "Solvent effects on the photochromic reactions of diarylethene derivatives," *J. Phys. Chem.*, vol. 96, no. 19, pp. 7671–7674, 1992.

[18] K. Uchida, Y. Kido, T. Yamaguchi, and M. Irie, "Thermally irreversible photochromic systems. reversible photocyclization of *2-(1-Benzothiophen-3-yl)-3-(2 or 3-thienyl)maleimide* derivatives," *Bull. Chem. Soc. Jpn.*, vol. 71, no. 5, pp. 1101–1108, 1998.

[19] L. Raboin, M. Matheron, J. Biteau, T. Gacoin, and J. Boilot, "Photochromism of spirooxazines in mesoporous organosilica films," *J. Mater. Chem.*, vol. 18, no. 27, pp. 3242–3248, 2008.

[20] K. Kinashi, Y. Harada, and Y. Ueda, "Thermal stability of merocyanine form in spiropyran/silica composite film," *Thin Solid Films*, vol. 516, no. 9, pp. 2532–2536, 2008.

[21] T. Yoshida, A. Morinaka, and N. Funakoshi, "Photochromism of a vacuum-deposited *1',3',3'-trimethyl-6-hydroxyspiro[2H-1-benzopyran-2,2'-indoline]* film," *J. Chem. Soc., Chem. Commun.*, pp. 437–438, 1986.

[22] R. A. Evans, T. L. Hanley, M. A. Skidmore, T. P. Davis, G. K. Such, L. H. Yee, G. E. Ball, and D. A. Lewis, "The generic enhancement of photochromic dye switching speeds in a rigid polymer matrix," *Nat. Mater.*, vol. 4, no. 3, pp. 249–253, 2005.

[23] M. Q. Zhu, L. Zhu, J. J. Han, W. Wu, J. K. Hurst, and A. D. Q. Li, "Spiropyran-based photochromic polymer nanoparticles with optically switchable luminescence," *J. Am Chem Soc*, vol. 128, no. 13, pp. 4303–4309, 2006.

[24] M. Irie, "Diarylethenes for memories and switches," *Chem. Rev.*, vol. 100, no. 5, pp. 1685–1716, 2000.

[25] A. W. Snyder and J. D. Love, *Optical Waveguide Theory*. London: Kluwer Academic Publishers, 2000.

[26] A. Yariv, *Optical Electronics in Modern Communications*. New York: Oxford University Press, 5th ed., 1997.

[27] K. Karapetyan, U. Wiedemann, C. Dan, D. Pritzkau, F. Bruse, W. Alt, and D. Meschede, "Optical fibre toolbox for MATLAB," 2010. `http://www.mathworks.com/matlabcentral/fileexchange/27819`.

[28] A. W. Snyder and W. R. Young, "Modes of optical waveguides," *J. Opt. Soc. Am.*, vol. 68, no. 3, pp. 297–309, 1978.

[29] J. D. Love and W. M. Henry, "Quantifying loss minimisation in single-mode fibre tapers," *Electron. Lett.*, vol. 22, no. 7, pp. 912–914, 1986.

[30] M. Sumetsky, "Optics of tunelling from adiabatic nanotapers," *Opt. Lett.*, vol. 31, no. 23, pp. 3420–3422, 2006.

[31] T. A. Birks and Y. W. Li, "The shape of fiber tapers," *J. Lightwave Technol.*, vol. 10, no. 4, pp. 432–438, 1992.

[32] J. S. Harper, C. P. Botham, and S. Hornung, "Tapers in single-mode optical fibre by controlled core diffusion," *Electron. Lett.*, vol. 24, no. 4, pp. 245–246, 1988.

[33] A. D. Yablon, *Optical fiber fusion splicing*. Berlin: Springer, 2005.

[34] Nufern, "Specifications of S630-HP, 630 nm pure silica core fiber." `http://www.nufern.com/fiber_detail.php/91`. Accessed on 2011-07-31.

[35] A. Stiebeiner, O. Rehband, R. Garcia-Fernandez, and A. Rauschenbeutel, "Ultra-sensitive fluorescence spectroscopy of isolated surface-adsorbed molecules using an optical nanofiber," *Opt. Express*, vol. 17, no. 24, pp. 21704–21711, 2009.

[36] N. Bloembergen, *Nonlinear Optics*, ch. 1. New York: Benjamin, 1st ed., 1965.

[37] R. W. Boyd, *Nonlinear Optics*. San Diego: Academic Press, 2nd ed., 2003.

[38] G. P. Agrawal, *Nonlinear Fiber Optics*. London: Academic Press, 1989.

[39] Y. Fujii, B. Kawasaki, K. Hill, and D. Johnson, "Sum-frequency light generation in optical fibers," *Opt. Lett.*, vol. 5, no. 2, pp. 48–50, 1980.

[40] Y. Sasaki and Y. Ohmori, "Phase-matched sum-frequency light generation in optical fibers," *Appl. Phys. Lett.*, vol. 39, pp. 466–468, 1981.

[41] R. Terhune and D. Weinberger, "Second-harmonic generation in fibers," *J. Opt. Soc. Am. B*, vol. 4, no. 5, pp. 661–674, 1987.

[42] U. Österberg and W. Margulis, "Dye laser pumped by nd:yag laser pulses frequency doubled in a glass optical fiber," *Opt. Lett.*, vol. 11, no. 8, pp. 516–518, 1986.

[43] R. H. Stolen and H. W. K. Tom, "Self-organized phase-matched harmonic generation in optical fibers," *Opt. Lett.*, vol. 12, no. 8, pp. 585–587, 1987.

[44] D. Z. Anderson, V. Mizrahi, and J. E. Sipe, "Model for second-harmonic generation in glass optical fibers based on asymmetric photoelectron emission from defect sites," *Opt. Lett.*, vol. 16, no. 11, pp. 796–798, 1991.

[45] J. Lægsgaard, "Theory of surface second-harmonic generation in silica nanowires," *J. Opt. Soc. Am. B*, vol. 27, no. 7, pp. 1317–1324, 2010.

[46] P. Weidner and A. Penzkofer, "Spectral broadening of picosecond laser pulses in optical fibres," *Opt. Quantum Electron.*, vol. 25, no. 1, pp. 1–25, 1993.

[47] T. Okuno, M. Onishi, and M. Nishimura, "Dispersion-flattened and decreasing fiber for ultra-broadband supercontinuum generation," in *Integrated Optics and Optical Fibre Communications, 11th International Conference on, and 23rd European Conference on Optical Communications (Conf. Publ. No.: 448)*, vol. 5, pp. 77–80, 1997.

[48] R. H. Stolen and C. Lin, "Self-phase-modulation in silica optical fibers," *Phys. Rev. A*, vol. 17, no. 4, pp. 1448–1454, 1978.

[49] N. Tzoar and M. Jain, "Self-phase modulation in long-geometry optical waveguides," *Phys. Rev. A*, vol. 23, no. 3, pp. 1266–1270, 1981.

[50] D. Anderson and M. Lisak, "Nonlinear asymmetric self-phase modulation and self-steepening of pulses in long optical waveguides," *Phys. Rev. A*, vol. 27, no. 3, pp. 1393–1398, 1983.

[51] P. Kean, K. Smith, and W. Sibbett, "Spectral and temporal investigation of self-phase modulation and stimulated raman scattering in a single-mode optical fibre," in *Optoelectronics, IEE Proceedings J*, vol. 134, pp. 163–170, 1987.

[52] M. Sumetsky, "How thin can a microfiber be and still guide light?," *Opt. Lett.*, vol. 31, no. 7, pp. 870–872, 2006.

[53] M. Baudrier-Raybaut, R. Haïdar, P. Kupecek, P. Lemasson, and E. Rosencher, "Random quasi-phase-matching in bulk polycrystalline isotropic nonlinear materials," *Nature*, vol. 432, no. 7015, pp. 374–376, 2004.

[54] D. Pritzkau, "Measurement of submicrometer diameters of tapered optical fibres using scanning electron microscopy," Master's thesis, Institut für Angewandte Physik, Universität Bonn, 2010. `http://quantum-technologies.iap.uni-bonn.de/de/diplom-und-masterarbeiten.html`.

[55] B. Rieger and G. N. A. Veen, "Method to determine image sharpness and resolution in scanning electron microscopy images," in *EMC 2008 14th European Microscopy Congress 1–5 September 2008, Aachen, Germany*, pp. 613–614, Springer, Heidelberg, 2008.

[56] J. S. Villarrubia, A. E. Vladar, J. R. Lowney, and M. T. Postek, "Scanning electron microscope analog of scatterometry," in *Proc. SPIE*, vol. 4689, pp. 304–312, 2002.

[57] E. V. Anoikin, A. N. Guryanov, D. Gusovsky, E. M. Dianov, V. M. Mashinsky, S. I. Miroshnichenko, V. B. Neustruev, V. A. Tikhomirov, and Y. B. Zverev, "UV and gamma radiation damage in silica glass and fibres doped with germanium and cerium," *Nucl. Instr. Meth. B*, vol. 65, no. 1–4, pp. 392–396, 1992.

[58] F. Warken and H. Giessen, "Fast profile measurement of micrometer-sized tapered fibers with better than 50-nm accuracy," *Opt. Lett.*, vol. 29, no. 15, pp. 1727–1729, 2004.

[59] G. Brambilla and D. N. Payne, "The ultimate strength of glass silica nanowires," *Nano Lett.*, vol. 9, no. 2, pp. 831–835, 2009.

[60] T. A. Birks, J. C. Knight, and T. E. Dimmick, "High-resolution measurement of the fiber diameter variations using whispering gallery modes and no optical alignment," *IEEE Photonic. Tech. L.*, vol. 12, no. 2, pp. 182–183, 2000.

[61] M. Sumetsky, Y. Dulashko, J. M. Fini, A. Hale, and J. W. Nicholson, "Probing optical microfiber nonuniformities at nanoscale," *Opt. Lett.*, vol. 31, no. 16, pp. 2393–2395, 2006.

[62] G. H. Brown, *Photochromism*. New York: John Wiley & Sons, 1971.

[63] P. W. Atkins, *Physical chemistry*, ch. 16.2. Oxford Academic Press, 5th ed., 1997.

[64] V. Malatesta, *Organic Photochromic and Thermochromic Compounds: Physicochemical studies, biological applications, and thermochromism*, vol. 2, ch. 2: Photodegradation of organic photochromes. Kluwer Academic Press, 1999.

[65] H. Bouas-Laurent and H. Duerr, "Organic photochromism (IUPAC technical report)," *Pure Appl. Chem.*, vol. 73, no. 4, pp. 639–665, 2001.

[66] P. Müller, "Glossary of terms used in physical organic chemistry," *Pure Appl. Chem.*, vol. 66, no. 5, pp. 1077–1184, 1994.

[67] K. Kinashi, S. Nakamura, Y. Ono, K. Ishida, and Y. Ueda, "Reverse photochromism of spiropyran in silica," *J. Photoch. Photobio. A*, vol. 213, no. 2–3, pp. 136–140, 2010.

[68] E. Maibach, "Properties of XTPA." (private communication), March 2011.

[69] R. Garcia-Fernandez, W. Alt, F. Bruse, C. Dan, K. Karapetyan, O. Rehband, A. Stiebeiner, U. Wiedemann, D. Meschede, and A. Rauschenbeutel, "Optical nanofibers and spectroscopy," *Appl. Phys. B*, vol. 105, pp. 3–15, 2011.

[70] E. Mohn, "Kinetic characteristics of a solid photochromic film," *Appl. Opt.*, vol. 2, no. 7, pp. 1570–1576, 1973.

[71] K. Higashiguchi, K. Matsuda, S. Kobatake, T. Yamada, T. Kawai, and M. Irie, "Fatigue mechanism of photochromic *1,2-bis(2,5-dimethyl-3-thienyl)perfluorocyclopentene*," *Bull. Chem. Soc. Jpn.*, vol. 73, no. 10, pp. 2389–2394, 2000.

[72] Y. C. Jeong, D. G. Park, E. Kim, K. H. Ahn, and S. I. Yang, "Fatigue-resistant photochromic dithienylethenes by controlling the oxidation state," *Chem. Commun.*, pp. 1881–1883, 2006.

[73] M. Irie, T. Lifka, K. Uchida, S. Kobatake, and Y. Shindo, "Fatigue resistant properties of photochromic dithienylethenes: by-product formation," *Chem. Commun.*, pp. 747–750, 1999.

[74] H. Durr and H. Bouas-Laurent, *Photochromism: molecules and systems*. Elsevier Amsterdam, 2003.

[75] V. Malatesta, M. Milosa, R. Millini, L. Lanzini, P. Bortolus, and S. Monti, "Oxidative-degradation of organic photochromes," *Molecular Crystals and Liquid Crystals*, vol. 246, pp. 303–310, 1994.

[76] K. Karapetyan, *Single optical microfibre interferometer*. PhD thesis, University of Bonn, 2012. To be published.

[77] G. Berkovic, V. Krongauz, and V. Weiss, "Spiropyrans and spirooxazines for memories and switches," *Chem. Rev.*, vol. 100, no. 5, pp. 1741–1754, 2000.

[78] K. Sasaki and T. Nagamura, "Ultrafast wide range all-optical switch using complex refractive-index changes in a composite film of silver and polymer containing photochromic dye," *J. Appl. Phys.*, vol. 83, no. 6, pp. 2894–2900, 1998.

Acknowledgements / Danksagung

Diese Seite möchte ich dazu nutzen, um all denjenigen zu danken, die durch ihre Unterstützung zum Gelingen dieser Arbeit beigetragen haben.

Mein besonderer Dank gilt Prof. Meschede für die Betreuung meiner Promotion. Ich konnte stets auf seine Unterstützung zählen und er ließ mir die Freiheit, meine eigenen Arbeitsschwerpunkte entsprechend meiner Interessen zu wählen. Die enge Zusammenarbeit mit Kotya hat sehr zum Gelingen meiner Doktorarbeit beigetragen. Ich habe viel von seinem technischen und theoretischen Wissen gelernt und danke ihm für die vielen fruchtbaren Diskussionen. Nicht unerwähnt lassen möchte ich die anderen Mitglieder des Faserteams der letzten Jahre: Cristian, Dimitri und Fabian. Die Arbeit im Labor hat mir sehr viel Freude bereitet. Mittlerweile arbeiten Marcel, Christian und Jan mit den Fasern, bei denen die Experimente in guten Händen sind.

Wolfgang danke ich für seine großartige Hilfe bei allen Fragen. Von seinem enzyklopädischen physikalischen Wissen und seiner Erfahrung habe ich enorm profitiert. Ohne ihn hätten wohl viele Probleme ungelöst bleiben müssen. Dem ganzen Team der Gruppe Meschede danke ich für die gute Atmosphäre am Institut.

Nicht zuletzt danke ich der Mitgliedern aus der Verwaltung – Annelise, Dietmar, Fien, und Ilona – für ihre Hilfsbereitschaft bei allen organisatorischen Angelegenheiten. Vielen Dank auch an die technischen Werkstätten, auf die wir uns auch bei dringenden Aufträgen immer velassen konnte.

Allen Mitgliedern der Arbeitsgruppe Rauschenbeutel danke ich für die tolle Unterstützung bei unseren Besuchen in Mainz. Der Gedankenaustausch über andere Faserexperimente war immer sehr aufschlussreich. Des Weiteren möchte ich den Kollegen aus der physikalischen und organischen Chemie, Prof. Meerholz und Eduard Maibach sowie Prof. Herges, für die informativen Diskussionen danken.

Danke auch an meine Familie, die es mir immer wieder ermöglichte, auf andere Gedanken zu kommen und stets ein offenes Ohr für mich hatte. Ich bedanke mich bei Britta, für den Rückhalt und die Unterstützung die sie mir über die ganze Zeit gegeben hat.